Design study of large-scale linear generators for wave energy conversion

Doctoral Dissertation

DESIGN STUDY OF LARGE-SCALE LINEAR GENERATORS FOR WAVE ENERGY CONVERSION

September 2017

Graduate School of Marine Science and Technology
Tokyo University of Marine Science and Technology
Doctoral Course of Applied Marine Environmental Studies

Jing Hailian

Contents

List of abbreviation

WEC: wave energy converter
PM: permanent magnet
LG: linear generator
HTS: high-temperature superconductor
TLG: tubular linear generator
MMF: magnetomotive force
IEA: International Energy Agency
PTO: power take-off
OWC: oscillating water column
AWS: Archimides Wave Swing
SSG: Sea-wave Slot-cone Generator
EMEC: Europe Marine Energy Centre
VRPM: variable reluctance permanent magnet
TFM: transverse flux machine
VHM: vernier hybrid machine
TLM: tubular linear machine
LTS: low-temperature superconductor
2G: second generation
FESS: flywheel energy storage system
SCLG: superconducting linear generator
TSFSLG: tubular superconducting flux-switching linear generator
PMFSLG: permanent magnet flux-switching linear generator

Abstract

Ocean wave energy is an attractive renewable energy source, which exists a great worldwide resource and offers the highest energy density among the renewable energy. Wave energy converters (WECs) have been developed to convert wave energy into electric power. Among them, direct-drive devices are considered more reliable and robust than gearbox or hydraulic systems due to the absence of intermediate mechanical conversion parts.

Permanent magnet linear generators (PM-LGs) are generally adopted to direct-drive wave energy converters (WECs). Nevertheless, these machines are physically large and heavy due to the low moving speed of waves, and they also suffer from the drawbacks of PM demagnetization, uncontrollable airgap flux, and high PM cost. On contrary, high-temperature superconductors (HTSs) exhibits high current-carrying capability, which can generate a higher magnetic field than that achieved by using copper wires or PMs, thus compensating for the low speed of the translator. Therefore, the HTSs have the potential of achieving compact and light machine, which causes little mechanical tension on the heaving buoy if used in WECs. The research in this thesis aims to breakthrough some key design technologies of HTS linear generators used for direct-drive WECs, and explore their advantages in WEC application.

This thesis consists of six chapters, and the contents are organized as follows:

In Chapter I, state of the art of WEC systems and the linear generators (mainly the different types of PM-LGs) used in direct-drive WECs are firstly introduced. Then, the fundamental properties, development and applications of HTSs are described. And two concepts of HTS linear generators proposed for WECs are presented, with the advantages and disadvantages discussed.

In Chapter II, characteristics of ocean waves are firstly investigated to make sure that the studies in this thesis are based on realistic wave data. Then, electrical system of a direct-drive WEC is presented, and the structural merits of the WEC device are highlighted. Next, the buoy movement during one-cycle operation is analyzed, and the relation of maximum output power and buoy size is clarified.

In Chapter III, PM tubular linear generators (PM-TLGs) are designed for the WEC. This chapter focuses on the electrical design method of PM-TLGs and the design results of different PM-TLGs (with PM thickness of 50 mm, 60 mm, and 70 mm, respectively). The electrical design method is described in detail, especially the methods of determining main machine parameters, calculating leakage coefficients with three-dimensional (3-D) simulation, and evaluating PM operating point. Optimum design results of the PM-TLGs are presented and discussed to select a most desirable one. And the magnetic flux density

distribution of the PM-TLG with 60 mm PMs is analyzed to verify the correctness of the design method.

Chapter IV aims to present the key design technologies of HTS-TLGs, clarify the induced voltage characteristics of the HTS-TLGs, introduce the cooling system and describe the evaluation of input power of cryocooler. The contents are organized as follows. Firstly, conceptual structure of the HTS-TLG is described in detail. Then, the key electrical design technologies of HTS-TLGs are presented, including the electrical design process, the determination of main machine parameters, the calculation of magnetomotive force (MMF), and the approaches of obtaining leakage coefficients and HTS heat loss with 3-D simulation. By using this electrical design method, a 1 MW HTS-TLG is designed for the WEC, and the design results are shown. Then, waveforms of electrical frequency, induced phase voltage, and rectified 3-phase voltage of the HTS-TLG are plotted to show its induced voltage characteristics. Besides, an economic way of connecting output power to grid is proposed, which benefits for reducing expensive filters. Moreover, cooling system of the WEC device is introduced, with the cryogenic vessels presented, various heat loss calculated, and input power of cryocooler evaluated.

In Chapter V, different TLGs designed for the WEC are compared and discussed. Firstly, three types of TLGs are described, which are HTS-TLG, PM-TLG, and Cu-TLG (with field exciting component made of copper wires). These TLGs are compared from the aspects of machine performance including the physical and electromechanical characteristics, and the costs. Furthermore, a 2 MW HTS-TLG is designed based on a different set of wave data，which is compared to another HTS-LG designed with approximate wave data to show the advantages of the proposed structure, and is further compared to the 1 MW HTS-TLG to show the influence of wave data on the generator design.

Chapter VI summarizes the research conducted and results presented in this study. The contributions in this thesis are highlighted. Moreover, the possible improvements are proposed for the future research.

Chapter I Introduction

1.1 State of the art of wave energy conversion systems

In the light of increased environmental concerns, renewable energy conversion technologies have attracted attention from governments, academy and utilities. As reported by IEA, the gross electricity production from non-combustible renewables (including wind, solar, geothermal, and others) in OECD countries accounted for 21.5% of all generation in 2015 [1]. However, there is still an unexploited renewable energy resource that waits to be harnessed, which is ocean wave energy. Ocean waves offer higher energy density (2-3 kW/m^2) than other renewable resources (wind 0.4-0.6 kW/m^2, solar 0.1-0.2 kW/m^2) [2][3]. Other benefits include: 1) little energy loss under large travel distance [4]; 2) larger predictable capability than both wind and solar energy [2]; 3) good correlation between source and demand (Natural seasonal variability of wave energy follows the electricity demand in temperature climate.) [4]; limited negative environmental impact in use [5].

Wave energy conversion technology attracted attentions because of not only above merits of ocean waves, but also a great worldwide resource of wave energy, which has been estimated to be greater than 2 TW [6]. Interests in wave energy conversion technology was firstly spurred by the emerging oil crisis of the 1970s [7], but did not last long as the oil price went down. Recently, following the issues of climate change and the rising level of CO_2, the focus on generating electricity from ocean waves is once again an important area of research, and a wide variety of wave energy converter (WEC) prototypes have been developed [8][9]. In the following, the predominant types of WECs and the main power take-off devices are presented.

1.1.1 Predominant types of wave energy converters (WECs)

During the last years, a large number of WECs have been presented in publications, developed, constructed and tested, which could be classified into: 1) onshore, nearshore and offshore devices depending on the distance from the coast; 2) attenuator, point absorber, and terminator according to the size and direction of the device regarding the incoming wave; 3) pressure differential, overtopping device, floating structure, and oscillating wave surge based on their working principle [2][10]. Fig. 1-1 shows the WEC prototypes and their developers based on above classifications, with schematic diagrams shown on top to depict their working principles. The typical WECs and the main types of power take-off (PTO) devices are described in detail as follows.

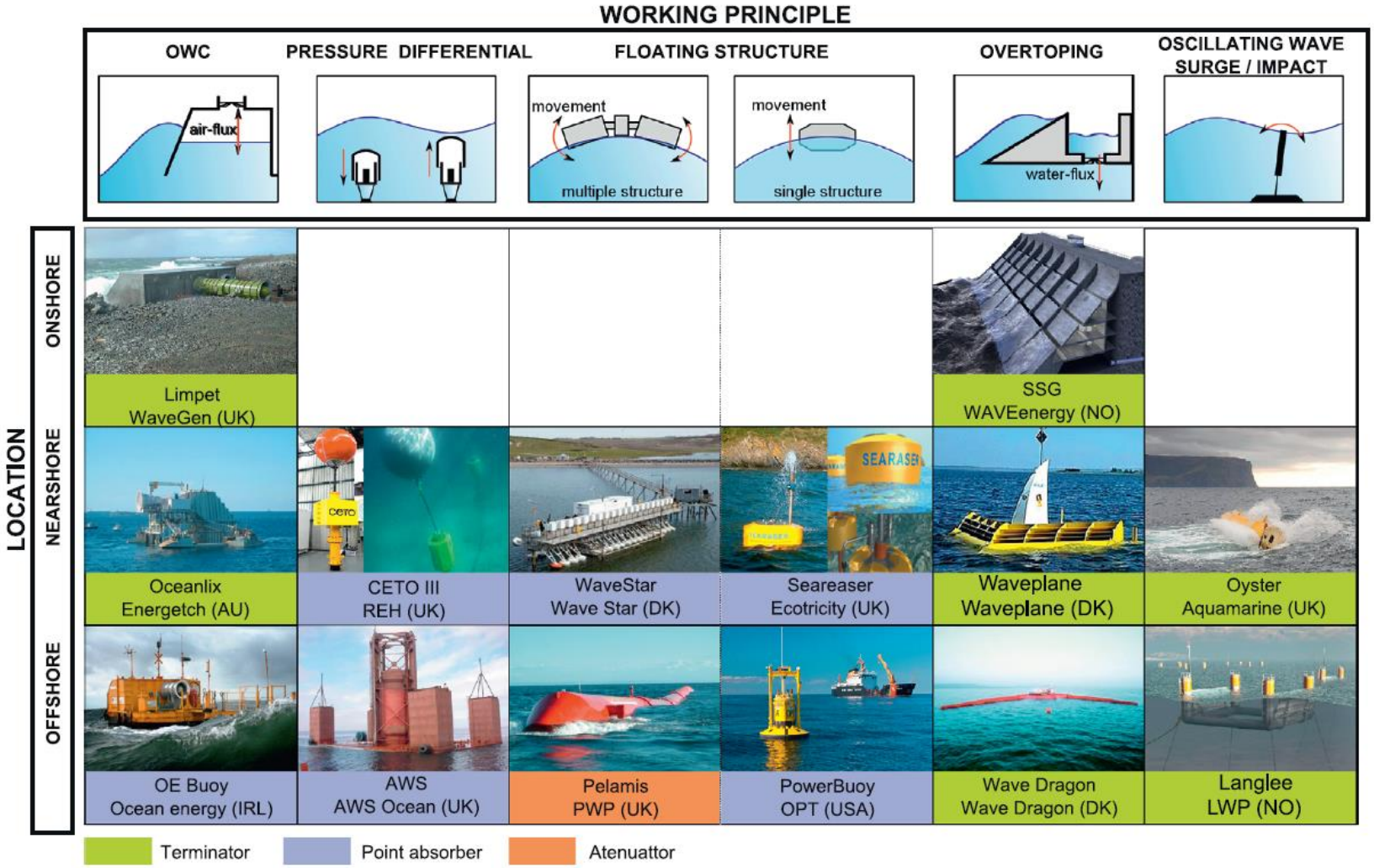

Fig. 1-1 Classifications of WECs [2].

A. Pressure differential

WECs belonging to this category can be subdivided into Archimedes effect converters and shoreline oscillating water columns (OWCs). The former is a submerged point absorber that uses the pressure difference generated between the wave crests and troughs over the device. As a wave crest is over the device, the water pressure compresses the air inside of it and moves the device down. As a through passes over, the water pressure will be reduced and the device rises. A classic example of this type of WEC is the 250 kW Archimides Wave Swing (AWS) [11]. The latter consists of a semi-submerged chamber with an opening at the bottom. The reciprocating movement of the waves raises and lowers the level of water therein, moving the internal air volume. This air flow drives a low-pressure Wells turbine which rotates in the same direction even though the air flow is bidirectional. The shoreline LIMPET 500 kW power plant represents one OWC system that is currently producing power for the National Grid, installed at Islay, Scotland, in 2000 [12]. The OWC concept could also be found in Oceanlix 3 MW products (BlueWAVE) [13]. Advantages of the OWC wave power device are simplicity, robustness, and high reliability.

B. Floating structure

This type of devices is based on a floating body, which is slack-moored to the sea bed, and moved by the waves. The usable oscillatory movement may be vertical, horizontal, pitch or a combination of them, such as the OPT (Ocean Power Technologies) PowerBuoy (vertical oscillation) [14] and the Pelamis Wave Power (pitching device) [15]. The Pelamis became the world's first offshore wave machine when it was first connected to the UK grid in 2004 [16], followed the world's first commercial Pelamis Wave Power's Agucadoura Wave Farm, which started operating and delivering 2.25 MW in Northern Portugal in 2008 [17].

C. Overtopping wave power device

Overtopping systems force water to a reservoir above the sea level, and then releases the water back to sea through head turbines. A typical such converter is the 4-10 MW Wave Dragon depending on the wave climate at deployment sites [18][19]. Another example is the Sea-wave Slot-cone Generator (SSG), a 150 kW WEC pilot project in the island of Kvitsoy, Norway [20].

D. Oscillating wave surge device

An oscillating wave surge converter is generally comprised of a hinged deflector, positioned perpendicular to the wave direction (a terminator). The deflector moves back and forth, exploiting the horizontal particle velocity of the wave. An example is the 800 kW Aquamarine Power Oyster [21], a nearshore device, which had been grid-connected at EMEC's Billia Croo test site from June 2012 until 2015.

1.1.2 Power take-off devices

As WEC devices are generally heaving or nodding, electrical power must be generated by either a direct-drive linear generator or a conventional rotary generator with a mechanical interface that converts the alternative motion into a continuous one-directional motion. In the latter case, the mechanical interface is generally a pneumatic or hydraulic turbine. Some of these PTO elements are described as follows.

A. Air turbines

Using air turbines in WECs has the advantage of increasing the slow velocities of waves to high air flow rates. Nevertheless, as the flow through the turbine is reciprocating, random, and highly variable over time, conventional turbines are not appropriate for WECs. Thus, several types of air turbines like the Wells air-turbine, the Dennis-Auld turbine, and the impulse air-turbine have been proposed for WECs. Fig. 1-2 shows the schematic diagrams of these three types of air turbines, which are all self-rectifying turbines.

The Wells air-turbine is the most popular air turbine in OWCs [22] because of its ability to rotate in the same direction despite of airflow direction, and the features of relatively high velocity ratio of rotational blade to air-flow and low cost to construct. Nevertheless, it has disadvantages like: low or even negative torque at small flow rates; low efficiency (around 60%-65%) [23][24]; high noise; poor starting; and relatively large diameter for its power (2.6 m for the counter-rotating 500 kW turbine of the LIMPET Islay II plant) [22].

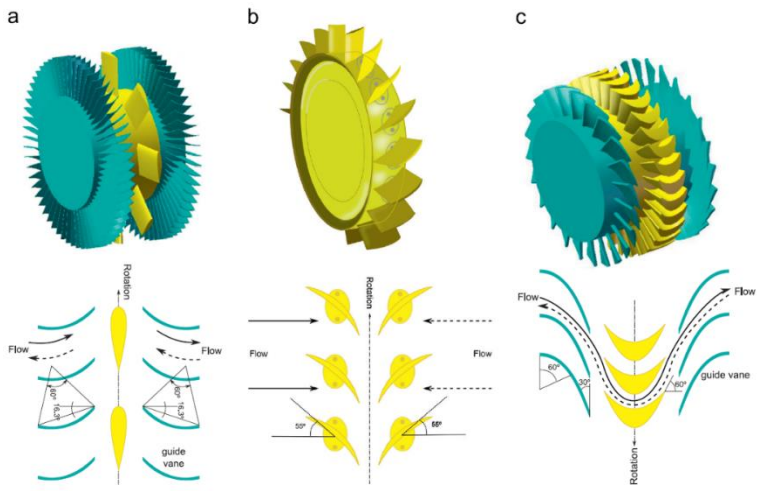

Fig. 1-2 Schematic diagrams of air turbines for WECs. (a) Wells turbine with guide vanes (b) Denniss-Auld turbine and (c) impulse turbine.

The Dennis-Auld air-turbine was developed in Australia and installed in the Oceanlinx OWC [25], as shown in Fig. 1-3. The blades are located on the periphery of the rotor hub in a neutral position, parallel to the axial direction of the flow. The Dennis-Auld turbine has a much larger pitching range than the variable pitch Wells turbine, so it has a much greater

solidity (total blade area divided by turbine sweep area) which increases the efficiency of the device [26].

The impulse air-turbine is a self-rectifying turbine with an axis of rotation aligned to the direction of an air flow. An example of its utilization is the wave energy plant of Niigata-Nishi port [27][28], as shown in Fig. 1-4. The air turbine has guide vanes both upstream and downstream. These guide vanes are symmetrical with respect to the rotation axis to achieve rotation in a single direction from bi-directional airflow generated by OWC. The advantages and disadvantages of impulse turbines compared to Wells turbines are not clear, depending on which versions of each are being compared [10].

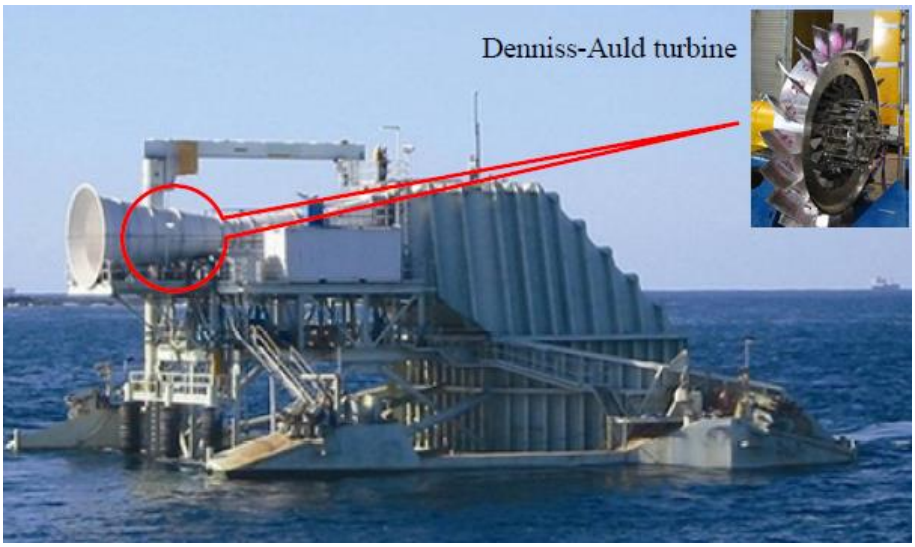

Fig. 1-3 Full-scale module of Oceanlinx [29].

Fig. 1-4 OWC device and impulse air turbine at Niigata-Nishi Port, Japan [30].

B. Hydraulic turbines

The significant advantage of using sea water turbines is that leakage of fluid causes no environmental problems. Hydraulic turbines are mainly impulse hydro-turbines and reaction hydro-turbines. The most common type of impulse turbine is Pelton turbine, which is used in the Oyster WEC. As shown in Fig. 1-5 (a), this turbine is composed of a wheel with several split buckets mounted around its rim. High velocity water jets are directed onto the split buckets, and the momentum of the water jets is transferred to the turbine, so that the turbine rotates. Pelton turbines are very efficient in high-head and low-flow applications. Therefore, they are not suitable for overtopping devices, but suitable for oscillating wave surge devices [31]. For the reaction hydro-turbine, the two most common types are the Kaplan and Francis turbine, as displayed in Fig. 1-5 (b) and (c). The Kaplan turbines are suited best to ocean energy devices as they can produce a highly efficient output power in low head applications, as in Wave Dragon [29] and SSG [20]. On the contrary, Francis turbines are suitable for high-head applications, therefore, they are not usually employed for WEC applications.

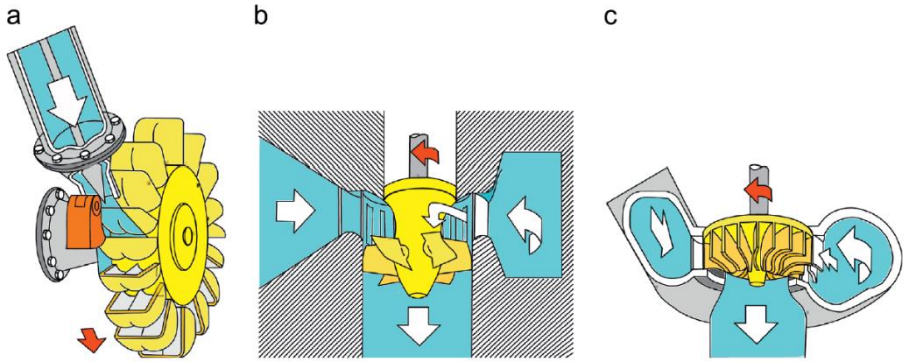

Fig. 1-5 Hydro turbines for WECs: (a) Pelton turbine, (b) Kaplan turbine and (c) Francis turbine [2].

C. High-pressure or oil-hydraulics cylinders

Another method of converting the low-speed oscillating motion is to employ high-pressure or oil-hydraulics cylinders, like the PowerBuoy [14]. Fig. 1-6 shows a schematic representation of the hydraulic PTO. The motion of a heaving buoy is firstly converted into hydraulic energy via a hydraulic cylinder, moving a fast-hydraulic motor, which drives an ordinary electrical generator. In this way, the oscillating motion of the buoy is converted into electric energy. In order to generate a regular output power, the hydraulic motor has variable capacity to drive the generator at a constant speed despite a variable flowrate. Usually, between the cylinder and motor, there are accumulators to provide energy storage and to maintain constant flow to the hydraulic motor.

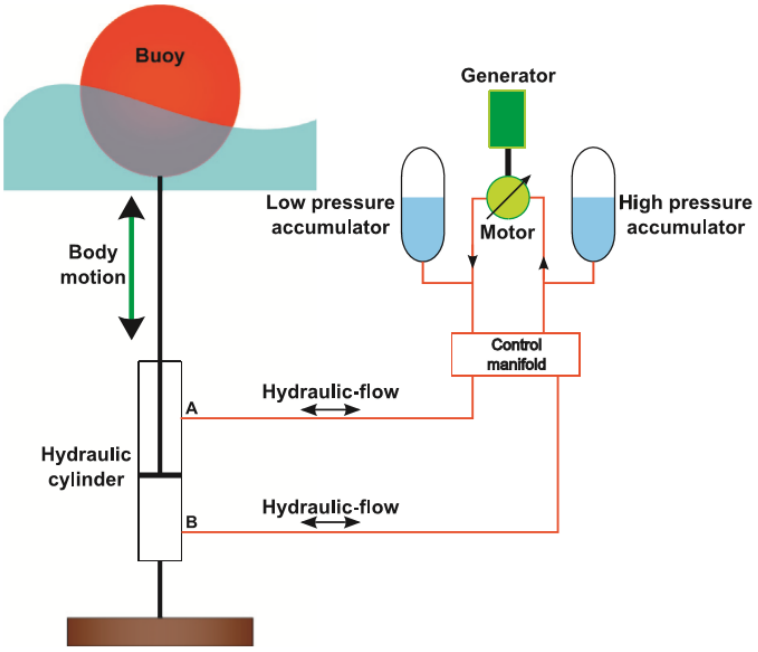

Fig.1-6 Schematic representation of the hydraulic PTO [2].

Despite the advantages of the different types of PTO devices, some severe drawbacks of the pneumatic and hydraulic systems in WECs have been obstacles to the development and application of WEC systems, which are summarized as:

- Both the pneumatic and hydraulic system involve many stages to interface the low-speed reciprocating motion of waves to the high-speed rotary motion of an electrical generator. All these stages have moving parts requiring maintenance, and the off-shore maintenance is more difficult and restricted by weather conditions.
- Turbines are expensive and do not exhibit high efficiencies over a wide speed range.
- For the hydraulic turbine systems, sea water is a complex fluid with various unpredictable constituents. The abrasive particles in sea water could damage seals and valves of devices.
- There are conflicts with fisheries interests on low-head schemes, and with irrigation needs on high head schemes.

D. Direct Drive

As mentioned above, the reliance on conventional high-speed rotary electrical generators inevitably involves complex and inefficient pneumatic or hydraulic PTO systems. If the electrical generator could be directly coupled to the wave energy device there would be fewer intermediate conversion stages, thus simpler structure and lower maintenance requirements.

AWS, developed in the Netherlands and first tested in the sea off the coast of Portugal in 2004, is the first direct-drive WEC device which adopts a double-sided permanent magnet linear generator (PM-LG) [32][33]. The AWS is basically a cylindrical air-filled chamber,

the lid of which, can move in vertical direction. As a wave crest passes over the device, pressure inside of the chamber is increased, reducing the volume of the air chamber, hence the device will fall. The device will rise again when a trough passes over the device. The AWS device is survivable and reliable whilst providing best-in-class efficiency and cost and a minimal environmental foot-print due to the use of direct-drive technology and the sub-sea location. The inventors intend to offer their 25 kW Waveswing on a pre-commercial basis from mid-2017.

Another attractive direct-drive WEC device is the Edinburgh Duck [34], which consists of a rocking cam shaped device reacting a force against a stationary spine, as depicted in Fig. 1-7. A custom-made rotary machine could be used as the PTO, in which the generator stator is integrated into the spine and the rotor in the nodding cam. It is worth noting that it is one of the few devices that is suitable for direct drive but produces rotary motion. An important feature of this device is its capability of converting both the kinetic and potential energies of the wave to mechanical energy, thus achieving very high absorption efficiencies (theoretically over 90%) [35].

Other direct-drive WEC systems employing PM-LGs have been developed at the kW level, such as the Trident Energy TE 5 in UK, which adopts a single-sided linear tubular air-cored generator [36], the linear converter in Uppsala University, which employs a multisided linear generator [37], the WEC system developed by Oregon State University, which uses a tubular PM-LG [38], and so on.

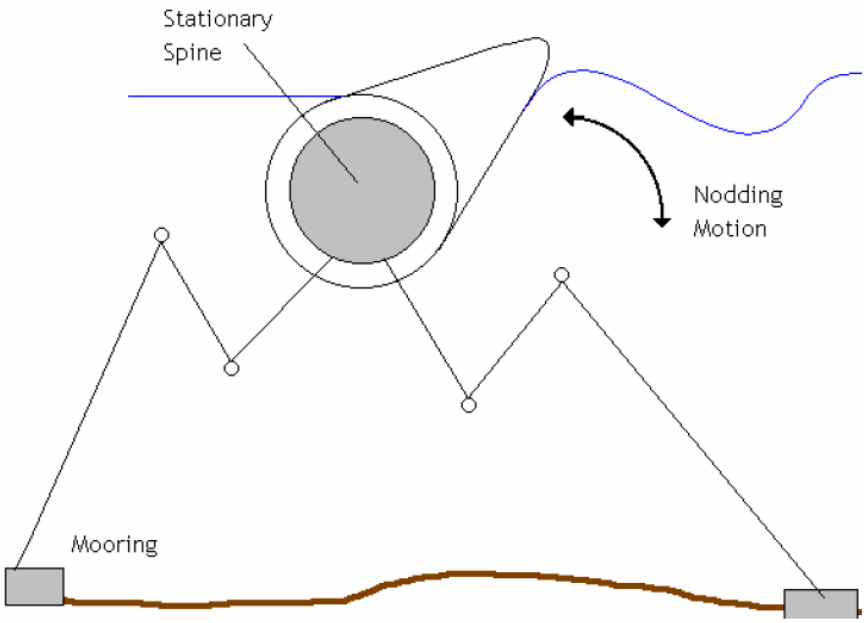

Fig. 1-7 Sketch of the Edinburgh Duck [39].

1.2 Linear generators used in direct-drive WECs

As mentioned above, the direct-drive concept is more promising in WEC application due to the absence of linear-to-rotary conversion mechanisms. At present, PM-LGs are generally used in direct-drive WECs, which produce higher power density than copper machines. In the following, different types of PM-LGs for direct-drive WECs are presented, with their advantages and disadvantages discussed.

A. Double-sided / Multi-sided PM-LG

The AWS employs a double-sided PM-LG, with magnets on the translator [32][33], as displayed in Fig. 1-8. It is reported that major merits of the PM-LG include a rather high force density and the elimination of electrical contact to the translator. However, the double-sided PM-LG used in the AWS has several disadvantages, like the severe bearing loads caused by the attractive force between stator and translator, the large size and high cost, and the high losses [40]. In addition, the PM-LGs suffer from demagnetization of PMs and uncontrollable airgap flux.

To eliminate load on the structure of generators, N. Hodgins *et al*. proposed a C-GEN machine for the AWS, which is basically a double-sided air-cored PM-LG [41]. Fig. 1-9 shows the 50-kW prototype of the C-GEN generator with the C-Core modules [42]. The C-GEN machine features no attractive forces between the stator and the PM translator as a C-shape translator is adopted, which eliminates the bearing load. However, there are still large attraction forces between facing magnets, which increase the mechanical challenges. A 50-kW prototype has been manufactured and tested at both no-load and half-loaded conditions with velocities controlled by a hydraulic system, which proves the concept to AWS applications.

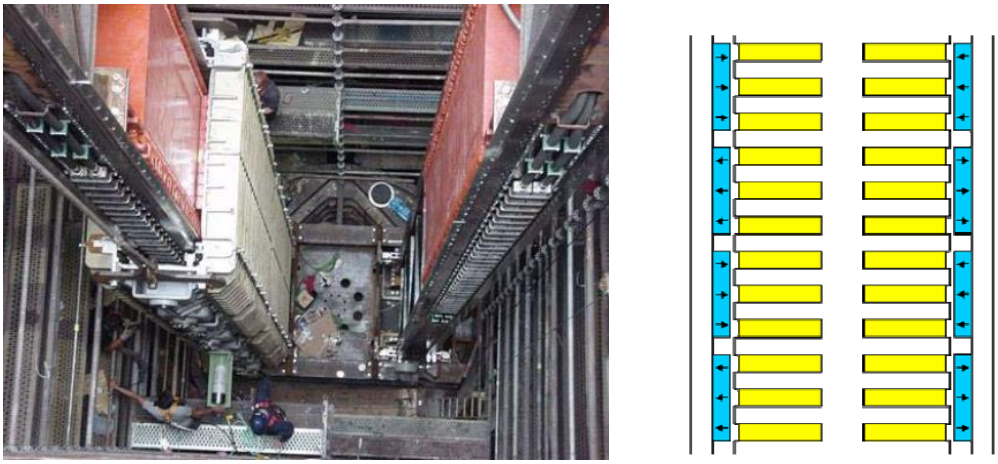

(a) (b)

Fig. 1-8 (a) The PM-LG in the AWS; (b) a sketch of the cross section [43].

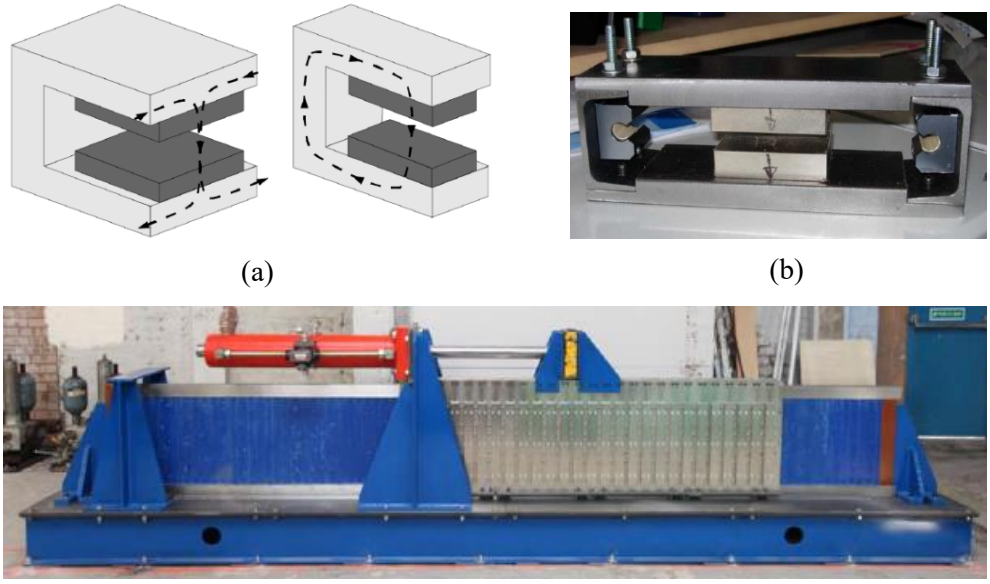

(a) (b)

(c)

Fig. 1-9 The 50-kW C-GEN generator: (a) flux paths within the C-Core module and between modules; (b) Completed linear module; (c) prototype of the generator [42].

M. Leijon et al. in Uppsala University proposed a 100 kW PM-LG with an octagonal stator for a direct-drive WEC [44], aiming to find a robust construction that optimizes price, maintenance cost and environmental impact. Then, they constructed a 10-kW laboratory four-sided linear test generator, as shown in Fig. 1-10, to verify computer simulations and investigate the mechanical and electromagnetic properties of the prototype [45]. And the experimental result shows excellent agreement between measured data and simulations. Nevertheless, compared to a double-sided LG or a tubular LG, this structure is more complicated, and there would be more leakage fluxes due to the coil ends.

Fig. 1-10 A 10 kW laboratory four-sided, three-phase synchronous linear generator [45].

B. Variable reluctance PM machines

Variable Reluctance Permanent Magnet (VRPM) machines such as transverse flux machine (TFM) and vernier hybrid machine (VHM) exhibit much higher airgap shear stress (a shear stress of 100 kN/m^2 reported for the TFM [46]) than conventional PM synchronous machines (with shear stress in the region of 20-30 kN/m^2). Such a VRPM machine could reduce the airgap surface area by a factor of 5, which lead to small machines for marine applications. Mueller & Baker have built a linear vernier hybrid PM machine to investigate its suitability for direct-drive WECs [39][47]. As shown in Fig. 1-11, stator of this machine consists of iron C-cores placed in pairs facing each other, with armature windings wound around the limbs of the C-cores. As shown in the schematic sketch of the single phase, PM magnets are mounted on the limbs of the stator with alternating polarities, and the magnets on the facing limbs have opposite polarities. Translator is sandwiched between the stationary C-core stator. When the translator moves one tooth pole pitch the polarity of flux changes, producing a rapid flux reversal, in which way, the low velocity of the translator is geared up to a high electrical frequency. During the flux reversal, an energy change takes place over a small distance, resulting in high thrust forces at the airgap. A shear stress of 106 kN/m^2 has been measured [48]. Another example of VRPM machine is proposed by Y. Du et al. in [49].

Despite the remarkable advantage in airgap shear stress, VRPM machines have the following characteristics, which limit their application to large-scale WECs:

- very high inductance due to the dominant leakage fluxes, thus a low power factor;
- large attractive forces, which should be overcome by using a support structure, thus leading to very complex machines;
- very small airgaps ($<$ 1 mm) with small magnet pitch.

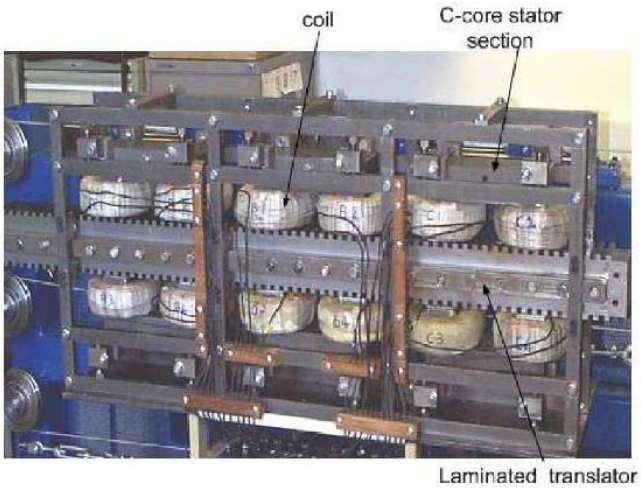

(b)

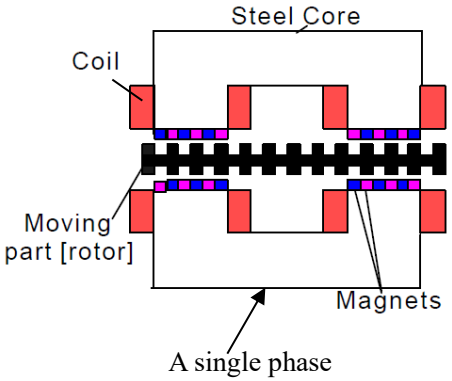

(b)

Fig. 1-11 A linear vernier hybrid PM machine: (a) the prototype; (b) the structural diagram of a single phase [39][46].

C. Tubular PM-LG

Tubular PM-LGs were payed attention as they have little attractive forces between stator and translator, low per unit self-inductance, and simple structure. A PM tubular linear generator (PM-TLG) is designed and manufactured for ocean wave energy conversion by Oregon University, with novelties of a seawater air gap between the magnets and armature, cogging force reduction techniques in the lamination design, and radially oriented laminations for reduction of eddy current loss. As shown in Fig. 1-12, the PM-TLG buoy system has three main components, which are the spar (3.3 m in height), the float (2.3 m in height), and the PM-TLG. The PM-TLG consists of a 1196 mm long magnet section located on the inside diameter of the float and a 286-mm long armature located on the outside diameter of the spar. The linear generator was tested on the pier in Yaquina Bay off the coast of Newport Oregon in the fall of 2007, with controlled actuation of the spar using the dock-side crane. The testing results indicated that the system can generator over 1 kW at 0.3 m/s. Ocean testing of a 10-kW direct-drive wave energy conversion system SeaBeav I was conducted but not succeeded due to the swelling of the bearing strips. Besides, the PM-TLG used in the SeaBeavI has the disadvantage of relatively large effective air gap, which requires a more magnetic material and more armature turns.

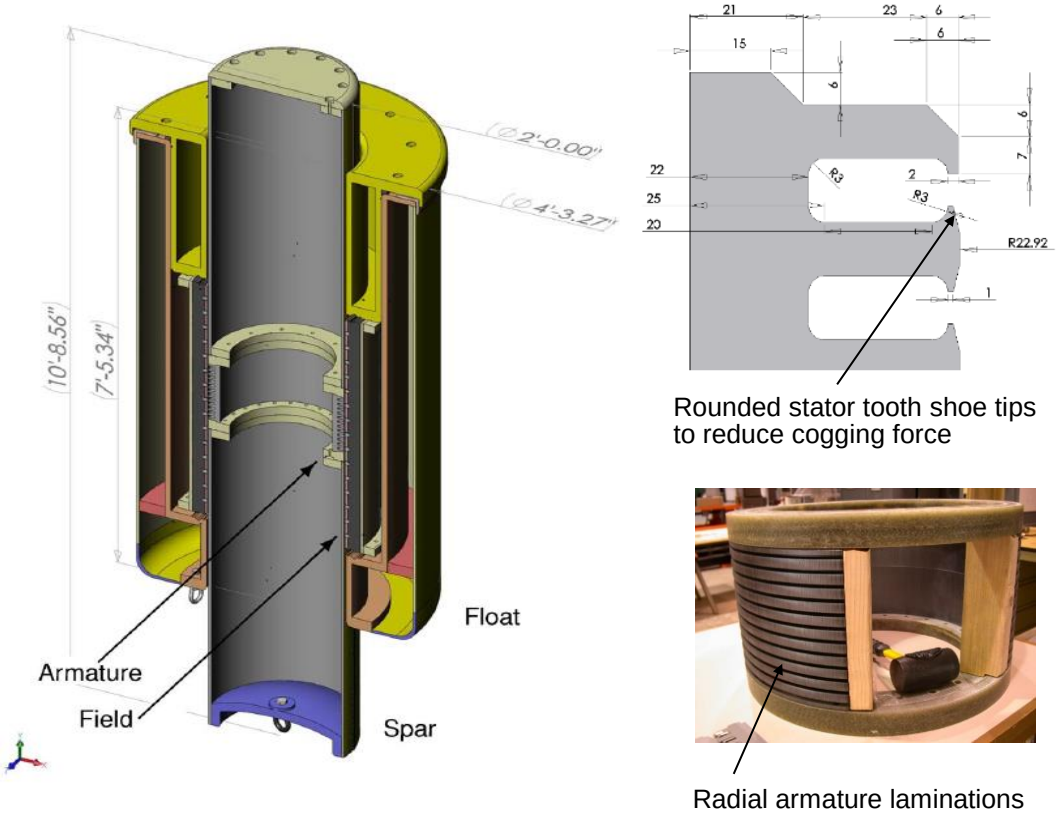

Fig.1-12 Cross-sectional view of buoy and PM-TLG proposed by Oregon University [50].

Trident Energy and Cambridge University designed a single-sided linear tubular air-cored generator for the Trident Energy TE 5, with the schematic diagram presented in Fig. 1-13. The Trident Energy TE 5 operates on the principle of having direct-drive linear generators mounted above the water surface, coupled to floats moving under the rig deck. The Trident Energy TE 5 comprises four floats, with each float coupled by a rigid thrust pole to two linear generators in tandem. Fig. 1-13 shows the schematic diagram of the tubular linear machines (TLMs) used in the Trident Energy TE 5, which have fixed permanent magnet stacks with alternating polarities. The generator coils are air-cored and in the form of a two-phase system, with a ferromagnetic screen located around the coils to gain more output power. Total length of the magnet stacks is 4.75 m, and stroke of the TLM is 3.3 m.

The TLMs used in the Trident Energy TE 5 features a ferromagnetic screen located around the coils, which improves the output of the air-cored TLMs, however, the air gap flux density dramatically decreases away from the PM translator due to the lack of iron in the stator.

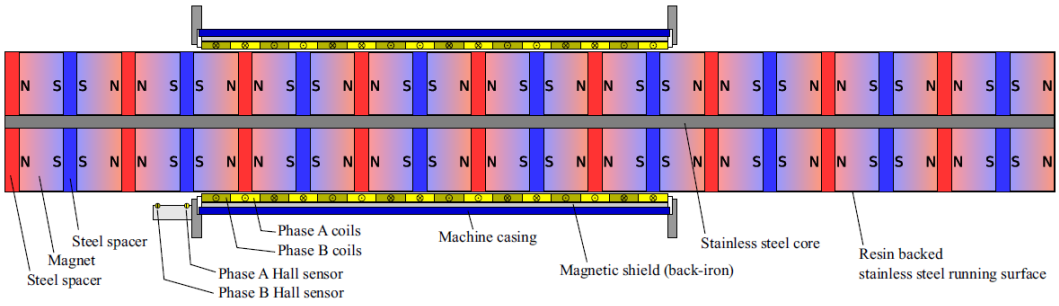

Fig. 1-13 Schematic diagram of the TLMs used in Trident Energy TE 5 [36].

D. Other types of PM-LG

As PM machines suffer from the drawbacks of uncontrollable airgap flux due to the PM excitation [51], very recently, some novel PM-LGs have been proposed to improve voltage waveform of the WEC device, such as those proposed in [52]-[54].

As presented above, different types of PM-LGs have been designed and developed for direct-drive WECs. In spite of the advantages of each machine mentioned before, some significant drawbacks existing in these machines are summarized as follows:

- The PM-LGs have the problem of PM demagnetization.
- Due to the slow speed of waves, these machines are physically large, and hence in high mass and high cost.
- As the magnetic field of PM-LGs cannot be adjusted, it results in high output voltage regulation and low power density.

These drawbacks brought the requirement for high current-density materials to make compact and light machines, and enhance the power density of direct-drive LGs.

1.3 Development and application of high-temperature superconductors (HTSs)

1.3.1 Fundamental properties of superconductors

(a) Electromagnetic properties of superconductors

Superconductivity has come a long way since first being discovered in 1911 by H. Kamerlingh Onnes. He found that at 4.2 K the resistance in a solid mercury wire immersed in liquid helium suddenly vanished. In the following observation, other metals such as lead and tin also exhibit zero resistance below a certain temperature, known as the critical temperature (T_c). Perfect conductivity (zero resistance) is one aspect of the properties of superconductors, and the other aspect is the perfect diamagnetism, which means that a superconductor completely expels an applied magnetic field except for a distance of λ, the penetration depth [55]. The perfect diamagnetism was discovered by Meissner and Ochsenfeld in 1933, and was known as the Meissner effect [56].

The disappearance of resistance and the complete expulsion of an applied magnetic field are the two principal properties to prove the existence of superconducting material. All superconductors must operate within a region determined by three inter-related parameters: critical current density J_c, critical temperature T_c, and critical magnetic field H_c. These parameters define the upper limits for the superconductivity in a material, exceed which a superconductor will revert to its normal state [57]. As shown in Fig. 1-14, the shaded volume shows the superconducting region of superconductors.

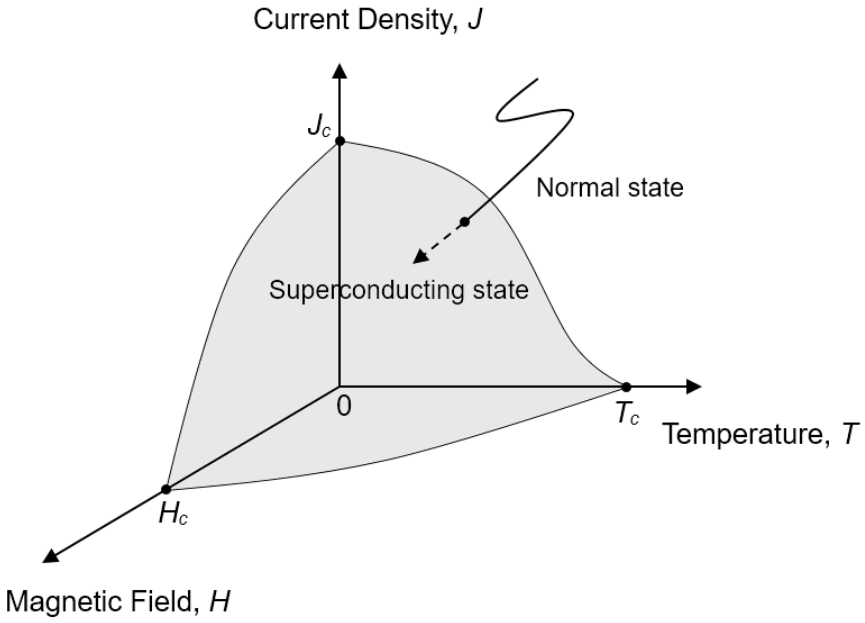

Fig. 1-14 Critical surface of a superconductor, defined by current density, temperature, and magnetic field.

(b) Type I & type II superconductors

Superconductors are classified into type-I and type-II superconductors according to the different normal to superconducting transition processes. The type-I superconductors are mainly comprised of metals and metalloids that show some conductivity at room temperature. They exhibit a very sharp transition from a normal state to a superconducting state, namely the Meissner effect (perfect diamagnetism below H_c). Type-I superconductors have a relatively low H_c, which limits their applications. Type-II superconductors are comprised of metallic compounds and alloys. Different with type-I superconductors, the transition from a normal to a superconducting state of type-II superconductors is gradually across a region of "mixed state". Type-II superconductors have two critical magnetic field, the lower critical field H_{c1} and the upper critical field H_{c2}. Type-II superconductors expel magnetic fields up to a lower limit H_{c1}. As the field increases beyond the H_{c1}, the type-II superconductors enter a mixed state, during which the magnetic field gradually penetrate the material until the H_{c2} is reached. At H_{c2}, the material is already fully penetrated and returns to the normal conducting state. The H_{c2} is much higher than the H_c of type-I superconductors, therefore, type-II superconductors can work in high magnetic fields and have wide practical applications.

Superconductors are distinguished as low temperature superconductors (LTSs) and high temperature superconductors (HTSs) depending on their critical transition temperature. HTSs generally have a T_c higher than around 23 - 30 K, and all other superconductors which have a T_c lower than this value are LTSs. Both LTSs and HTSs belong to type-II superconductors.

(c) Flux flow and flux pining of superconductors

As mentioned above, superconductors allow magnetic flux to penetrate the material above their critical field (H_c for type-I superconductors and H_{c1} for type-II superconductors). The magnetic flux penetrates the material in such a way that individual magnetic flux quanta enter the material and form cylindrically symmetric domains called vortices. Each vortex is composed of a circular shielding current flowing around a single flux quantum, as shown in Fig. 1-15. The superconducting shielding current is composed of a pair of superconducting electrons known as a Cooper pair. These vortices interact with each other in such a way that they repel each other by means of a Lorentz force F_L, given as:

$$F_L = J \times B \tag{1-1}$$

This Lorentz force comes from the interaction between one vortex's magnetic field and the circulating shielding current of its neighbor's vortex. The vortices move under the influence of the Lorentz force, but are trapped at defects in the lattice called pinning centers. This phenomenon is known as flux pinning. The pinning centers exert a force on the vortices known as the pinning force F_P. The pinning force acts on the core of a vortex and is equal to

the Lorentz force required to depin the vortex. When there is a transport current *J*, the Lorentz force becomes great enough to depin the vortices and causes a collective flux motion. If the pinning forces dominate, the flux motion is slow and is called flux creep. If the Lorentz forces dominate, the flux motion is fast and is known as flux flow.

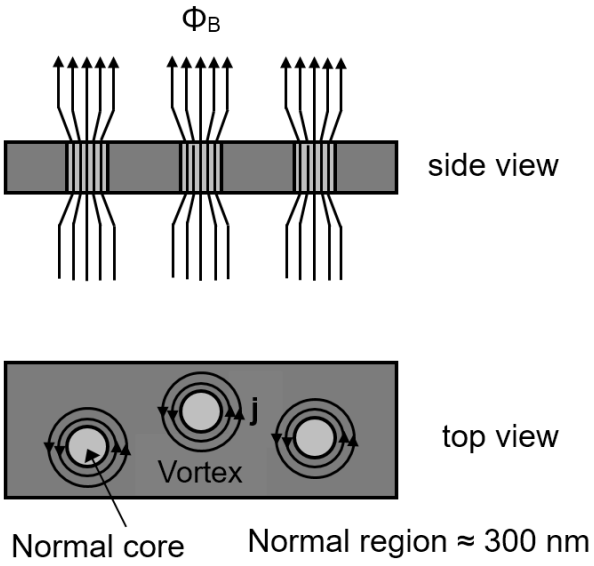

Fig. 1-15 Flux pinning for type-II superconductors.

(d) Loss in a superconductor

Due to the flux pinning in critical state, the magnetic flux in a superconductor will not change in a reversible way as the external applied field changes, and the work needed to overcome the pinning force relates to some losses in the superconductor. In applications, losses of type-II superconductors are distinguished as the transverse alternating applied field loss, the alternating current loss (AC loss), and the direct current loss (DC loss) depending on the power supply. The transverse alternating applied field loss results from applying a transverse alternating magnetic field to superconductors. The AC loss comes from the connection of a superconducting wire to an AC power supply with normal leads (with peak current of the superconducting wire below its critical value). Once the peak current of the superconducting wire is above its critical current, a large loss would be generated in the superconducting wire, in addition to the loss caused by the changing self-field. The DC loss occurs in a superconducting wire in the case that it is connected to a DC power supply with normal leads. The DC loss is small if the current is less than a critical value, but can become quite large if the DC current considerably exceeds the critical value.

The losses which occur in a superconductor must usually be kept to a very low level to maintain the superconductivity, which are much lower than the resistive loss in a normal conductor under the same circumstances. However, the losses are dissipated as heat in a low

temperature environment, leading to evaporation of the coolant or an increased thermal load on the cooling system. The use of HTS over LTS greatly reduces the problem of heat removal due to the higher operating temperature, but does not eliminate it. Therefore, calculating the losses of a superconductor allows for more detailed design of applications that make use of superconductors to justify the extra investment in the superconductor and the cooling equipment. In addition, superconductors must meet several other requirements to compete with the presently used normal conductors, including a high critical current and a low $/kAm price. The decision to utilize superconductors in electrical power devices is usually based on financial considerations: energy costs, superconducting material costs, cooling system costs, and maintenance and reliability [58].

1.3.2 Development of HTSs

(a) Discovery and main properties

HTSs were discovered by Georg Bednorz and Alex Muller in 1986 [2] when they studied the conductivity of a Lanthanum-Barium-Copper-Oxide (LaBaCuO) ceramic, which has a critical temperature of 30 K. This discovery started a surge of activity which discovered superconducting behavior as high as 125 K. HTSs are all ceramic-based copper oxide compounds and are coated superconductor tapes, known as the second generation (2G) superconductors.

YBCO (Yttrium-Barium-Copper-Oxide, $YBa_2Cu_3O_7$) is the most famous HTS material. It has a critical temperature of 95 K, which can be cooled to below by using the liquid nitrogen (LN_2, boiling point of 77 K). By contrast, LTSs become superconducting at temperatures near the boiling points of liquid helium or hydrogen (4.2 K and 20 K, respectively), which are both more expensive and difficult to obtain than LN_2.

YBCO also appeals to researchers because it is the cleanest and most ordered crystal. Fig. 1-16 shows the crystalline structure of YBCO. The crystal structure of YBCO is highly anisotropic, with much higher conductivity within the CuO_2 than perpendicular to the planes. Thus, supercurrents flow mainly within the CuO_2 (a-b) planes, and the trapped field generated by these supercurrents is directed along the c-axis.

Table 1-1 lists the main properties of four widely used HTS materials, which are YBCO-123, BSCCO-2212, BSCCO-2223, and Magnesium-diboride (MgB_2). Here, BSCCO is short for Bismuth-Strontium-Calcium-Copper-Oxide. These superconductors offer the promise of higher efficiency and lower operating cost than LTSs for the electrical industry. YBCO-123 and BSCCO-2223 are capable of operation in the temperature range of 20 K to 77 K, which have achieved widespread application. Despite the high-field properties at 4.2 K, BSCCO-2212 exhibits a very low current-carrying capability at 77 K. MgB_2 has lower critical temperature and current-carrying capability than the other HTS materials.

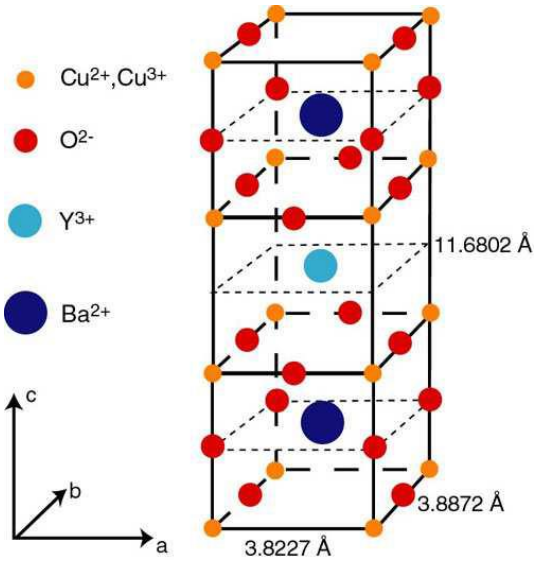

Fig. 1-16 Crystalline structure of YBCO [59].

Table 1-1 Main properties of four widely used HTS materials. (The electrical current and the magnetic field are oriented parallel to the CuO-layers.) [60][61][62]

Conditions	Materials		Y-123	Bi-2212	Bi-2223	MgB_2
	Critical temperature [K]		93	85	110	39
Thin films at 4.2 K (boiling He)	Upper critical field $\mu_0 H_{c2}$ [T]		≈ 300	≈ 400	> 100	35-60
	Irreversibility field $\mu_0 H_{irrev}$ [T]		> 30	> 30	> 30	8
	Critical current density in self-field J_{c0} [A/mm^2]		5×10^5	2×10^4	1×10^5	~10^4
	Critical current density at 0.1 T J_c [A/mm^2]		5×10^5	2×10^4	2×10^4	-
Thin films at 77 K (boiling N_2)	Upper critical field $\mu_0 H_{c2}$ [T]		≈ 56	≈ 35	> 20	-
	Irreversibility field $\mu_0 H_{irrev}$ [T]		> 10	≈ 0.005	≈ 0.2	-
	Critical current density in self-field J_{c0} [A/mm^2]		4×10^4	1×10^3	1×10^4	-
	Critical current density at 0.1 T J_c [A/mm^2]		2×10^4	0	1×10^3	-
Long-length flexible tapes at 77 K	Engineering critical current density in self-field J_e [A/mm^2]	Laboratory scale 0.01-1 m	200	80	200	-
		Industry scale 1-100 m	-	-	100	-

(b) Commercial HTS wires

As mentioned above, the four main HTS materials are YBCO-123, BSCCO-2212, BSCCO-2223, and MgB_2. Among them, BSCCO-2223, YBCO-123, and MgB_2 wires are currently commercially available. Particularly, the commercially availability of long-length HTS wires has made it possible to wind coils and cables for large scale applications. BSCCO-2223 is the most developed, but it is limited to long lengths due to the

manufacturing process. This material is mechanically weak, which must be laminated to stronger material for application. Sumitomo Electric Industries is one of the main companies which supply BSCCO-2223 wires [63]. MgB_2 could be independent of the magnetic field orientation because it can be made in a round shape. However, the low critical temperature and low critical temperature limit their applications. And their availability in long lengths is also limited. YBCO-123 coated conductors are available in manufacturing long-length wires as they contain some strong materials (e.g., stainless steel, brass or copper). American Superconductor (AMSC) [64] and SuperPower [65] are the two main companies that supply long-length YBCO-based HTS tapes/wires. The manufacturing techniques differ between the two, which results in a different configuration for the final product, as shown in Fig. 1-17 and Fig. 1-18, respectively.

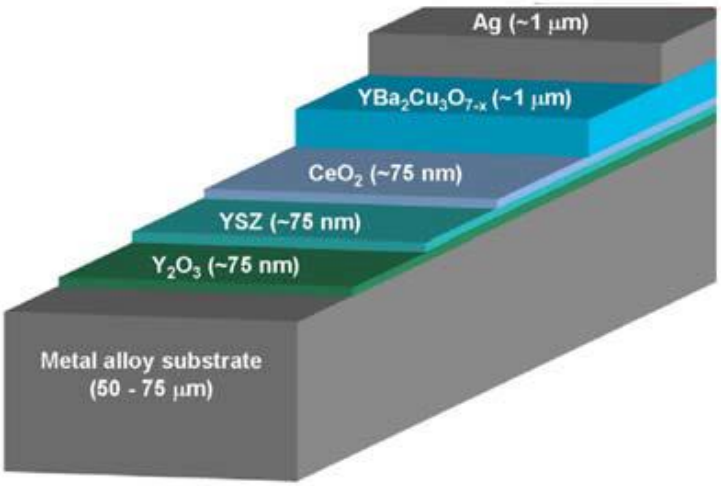

Fig. 1-17 American superconductor corporation's 2G HTS wire structure.

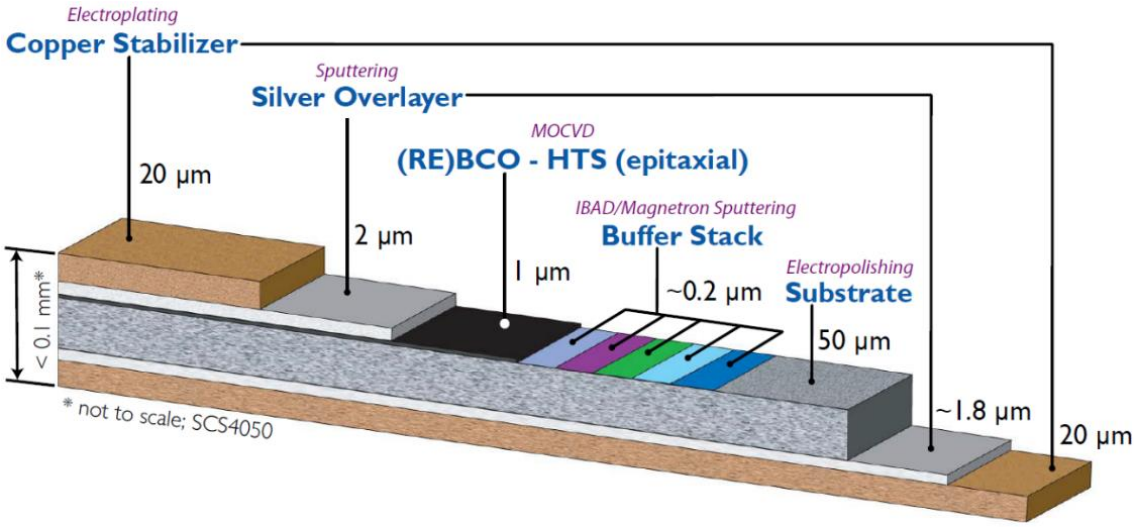

Fig. 1-18 SuperPower 2G HTS wire configuration.

AMSC's Amperium HTS wire conducts approximately 200 times the electrical current of copper wire of similar dimensions. This 2G wire is available in copper (Cu), brass and stainless-steel laminate. Used in power dense coils for applications such as synchronous motors, generators and magnets, the Amperium copper-laminated wire can dramatically reduce the size and weight of large-scale electrical equipment. This product provides significantly greater power throughput and efficiency than copper wires as well as high strength and stability with outstanding bend tolerance. The properties of the AMSC copper-laminated YBCO tapes are listed in Table 1-2.

Table 1-2 Mechanical and electrical properties of the AMSC copper-laminated YBCO tapes.

Type	**8501**			**8502**			**8502-350**
Average thickness (mm)	0.17-0.21			0.18-0.22			0.18-0.22
Minimum width (mm)	4.70			11.9			11.9
Maximum width (mm)	4.95			12.3			12.3
Minimum double bend diameter (mm)	30[i]			30[i]			30[i]
Minimum double bend diameter for spliced wire (mm)	100[i]			100[i]			100[i]
Maximum rated tensile stress (MPa)	150[i]			150[i]			150[i]
Maximum tensile strain at 77 K	0.25%[i]			0.3%[i]			0.3%[i]
Continuous piece length (m)	500			500			500
Minimum I_c (A)[ii]	80	90	100	250	275	300	350
Average J_e (A/cm^2)[iii]	8700	9800	10900	10300	11330	12360	14400

i Greater than 95% I_c retention

ii Critical current at 77 K, self-field, 1 μV/cm, 1 m resolution

iii Engineering current density

SuperPower manufactures long lengths (kilometer-class) of robust and high performing 2G HTS wire (coated conductors), based on ReBCO (rare earth barium copper oxide elements), with variations in width, substrate thickness, silver and copper stabilizer thickness, plus optional insulation. Characteristics of two types of SuperPower HTS wires is presented in Table. 1-3.

It is worth mentioning that these YBCO-based HTS wires have high anisotropy, and the tape performance is greatly affected by magnetic fields perpendicular to *a-b* plane of the tapes, as shown in Fig. 1-19.

Table 1-3 Characteristics of SuperPower 2G wires (Copper Stabilized).

Type	SCS4050	SCS12050
Width (mm)	4	12
Average thickness (mm)	0.1	0.1
Minimum bend diameter (mm)	11	11
Maximum rated tensile stress (MPa)	> 550	> 550
Maximum tensile strain at 77 K	0.45%	0.45%
Minimum I_c (A)	≥ 100	≥300
Continuous piece length (m)	Up to 500	Up to 500

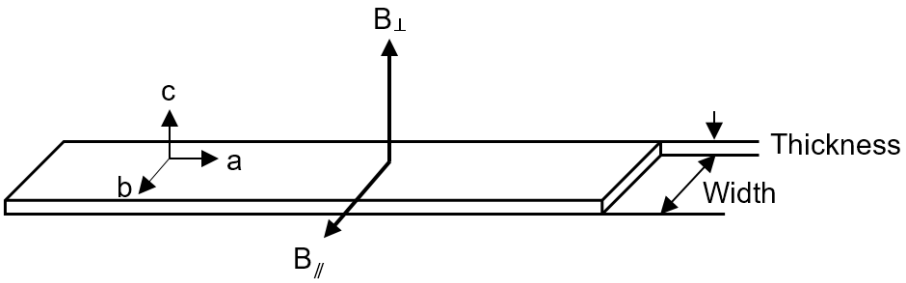

Fig. 1-19 Definition of perpendicular ($B_{\perp}$) and parallel ($B_{//}$) magnetic fields with respect to the superconducting tapes' cross section.

1.3.3 Applications of HTSs to electric power equipment

The advent of commercial HTS wires/tapes has spurred the employment of HTSs to practical application. The much higher current-carrying capability and the promise of low-cost HTS conductors coupled with reasonably priced refrigeration systems have further encouraged application of this technology to a variety of magnets and power equipment. Many prototypes have been constructed for electric power applications such as motors and generators, transformers, power transmission cables, fault current limiters (FCLs), Superconducting Magnetic Energy Storage (SMES). R&D status and advantages of HTS materials to electric power application are illustrated as follows:

(a) HTS motors and generators

Research on superconducting rotary machines has boosted after the discovery of HTS materials. Since the first 125-hp HTS motor was tested in 1996, various HTS machines (both generators and motors) have been proposed. AMSC has engaged in designing and manufacturing HTS motors since 2001. After a 5 MW, 230 r/min HTS ship propulsion motor being successfully completed and tested in 2004 [66], AMSC developed a 36.5 MW, 120 r/min HTS propulsion motor, and the full-power testing is completed in 2008 [67]. Siemens also reported about the successful manufacturing and testing of a 400 kW HTS

motor in 2004 [68]. It is worth noting that all these prototype machines employed expensive BSCCO-2223 HTS tapes, therefore, it is impossible to transition them into products in the viewpoint of economics.

However, currently available YBCO-123 coated conductors promise low-cost and higher current-carrying capability, which encourages renewed interest in developing HTS electric machines. Several concepts of HTS synchronous generators have been proposed for wind power generation, and prominent examples include: the 10 MW SeaTitan wind turbine, which adopts a generator with HTS field coils wound by AMSC's Amperium wires [69]; the 10 MW salient-pole wind turbine HTS synchronous generator [70], which employs race-track YBCO coils to make the field windings; the 5 MW superconducting wind turbine generator, which suggests using Superpower 2G 4050 tapes to manufacture the superconducting field windings [71], and so on.

Majority of developed HTS electric machines adopt HTS wires as field windings. Such machines have plentiful advantages over the conventional ones, which include:

- Smaller and lighter;
- Higher efficiency;
- Higher output power density;
- Longer coil life;
- Less vibration and quieter;

(b) HTS cables

With the increasing demand of improving the electrical capacity and flexibility of the electric grid, it has become an urgent issue to replace the current existing cables or overhead lines with high current-carrying materials. HTS cables are promising to address this issue. And some HTS cables have been demonstrated all over the world [72][73]. Listed below are the key benefits of employing HTS cables to electric grid:

- High power capacity: HTS cables could carry 3-5 times more power than the conventional copper cables of similar physical size.
- Low impedance: HTS cables has lower impedance than conventional cables and overhead lines.
- Low voltage operation: Thanks to the high current capacity, HTS cables can operation at lower voltage than equivalently rated copper cables, which enables reduction on the quantity of transformers and associated ancillary equipment.
- Ease of installation: HTS cables can be installed either in existing circuit or in deep underground.
- Elimination of resistance loss: HTS cables exhibit minimum waste heat or electric losses, and have no soil heating.

(c) HTS fault current limiters

The electric grid inevitably experiences extreme natural events and faults. Fault current limiters (FCLs), such as fuses, are employed to allow an electric grid to keep operating when a fault occurs. However, fuses require manual replacement after a fault. The HTS-FCLs are self-acting and resetting devices that allow the grid to recover quickly following a fault. HTS FCLs have been widely demonstrated [74][75]. Significant advantages of HTS-FCLs include:

- Rapid Response;
- Self-triggering and fail-safe;
- Negligible loss during normal system operation.

(d) HTS transformers

Transformers are the most widely used equipment in an electric grid. Longstanding efforts have been done to demonstrate HTS transformers [76][77], however, their development still lags HTS cables and FCLs. Compared to conventional transformers, potential advantages of HTS transformer are listed below:

- More compact and lighter;
- Longer life;
- Higher efficiency achieved with low AC-loss wire;
- Safer and more reliable;
- Fault current limiting;
- Environmentally friendly

(e) HTS electromagnetic storage

Energy storage devices plays a significant role in storing the energy generated from some intermittent energy sources, such as solar, wind, wave, and so on. HTS materials may be used in two important energy storage devices: flywheels or superconducting coils. The application of HTSs to flywheels, known as the flywheel energy storage system (FESS), is based on the use of HTSs in superconducting bearings [78][79]. And the application of HTSs to superconducting coils, known as SMES, is based on their zero resistance characteristics, which maintaining persistent currents in a superconducting coil [80].

1.4 Concepts of HTS linear generators for wave energy conversion

The successful development and testing of HTS rotary machines have paved the way for developing HTS linear machines. Up to now, HTS linear machines have been proposed for applications to electromagnetic aircraft launch system [81][82] and Maglev trains [83][84][85]. Among them, the machines presented in [82] and [85] employ HTS bulks. HTS

bulk magnets, which can be much stronger that rare-earth permanent magnets, are an efficient way to create excitation field in the machine, but the superconducting magnets are demagnetized if a fault occurs in the cooling system. Without an in-situ magnetizing system, they are not suitable for wave energy converters because of reliability issues. Alternatively, superconducting wires can be used to excite the linear machine. In very recent years, the application of HTS linear generators to direct-drive wave energy conversion has been paid attention by researchers, and several concepts have been proposed [86]-[89].

(a) Superconducting Homopolar / Bipolar Linear Machine

O. Keysan and M. Mueller in University of Edinburgh presented a 640-kW air-cored superconducting linear generator (SCLG) for wave energy converters [87], as presented in Fig. 1-20. Simulations on magnetic flux distribution and induced phase voltage were conducted, and AMSC's copper laminated Amperium wire is used in the HTS field winding in the simulations. Simulation results show that the peak value of airgap flux density is up to 1.43 T, and the phase voltage waveform are plotted with a sinusoidal velocity profile input (peak value of 2.2 m/s). The total mass of the generator is 21.5 tons including the cooling system and mechanical structure. Length of the stator is 7.2 m and that of the translator is 9.6 m. Thrust density of the machine is calculated as 30.3 kN/m^2 at full load.

Biggest advantage of the SCLG is having a stationary superconducting coil, which simplifies the cooling system. Besides, the iron cores divert the magnetic flux so that the HTS wires are subjected to minimum magnetic flux, which maximize the current density of the HTS wires. Furthermore, the translator of the generator is air-cored, which eliminates the attraction forces between stator and translator. However, the SCLG is heavier than a PM counterpart due to the heavy magnetic cores.

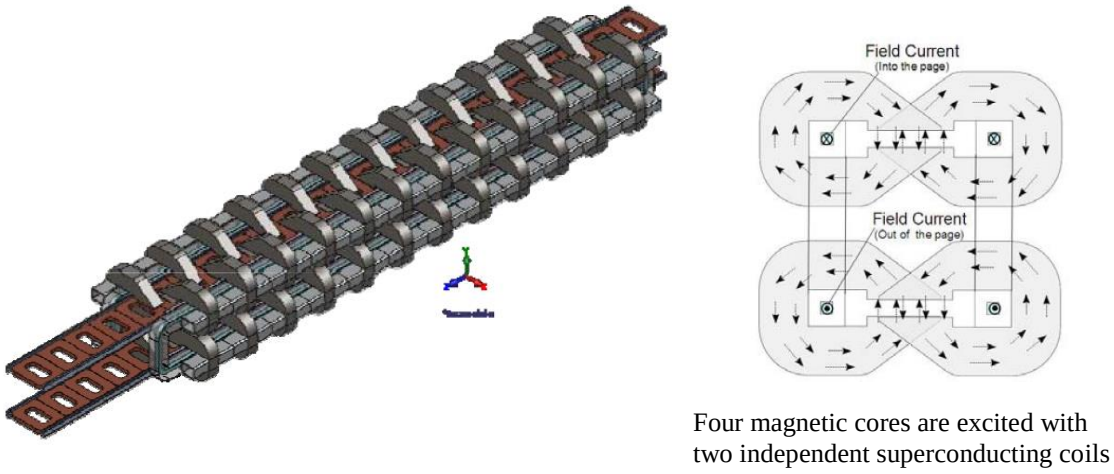

Fig. 1-20 (a) CAD model of the bipolar air-cored superconducting linear generator (isometric view). (b) Flux density vectors in the magnetic cores (front view).

(b) Tubular superconducting flux-switching linear generator

In 2005, Lei Huang et al. from Southeast University, Nanjing, China proposed a tubular superconducting flux-switching linear generator (TSFSLG) based on the VHMs for direct-drive WECs [89][90], as shown in Fig. 1-21. The structure features both 3-phase AC superconducting armature windings and DC superconducting field windings located in the stationary primary, which simplifies the cooling system and avoids the movement of transmission cables. MgB_2 are used to make the armature windings and field windings. Besides, the air gap flux density of the proposed TSFSLG is higher and controllable compared to the permanent magnet flux-switching linear generator (PMFSLG). Moreover, the tubular structure is helpful to reduce the attractive forces between the stator and the translator. No-load and load performance comparison of the TSFSLG with a VHM and a PMFSLG demonstrated that the proposed linear generator has less cogging force, lower voltage regulation, higher efficiency, and higher power density.

However, we suspect that it may need long time to launch the large-scale practical test facilities of such kind of machines due to the complex structure and AC loss of HTSs.

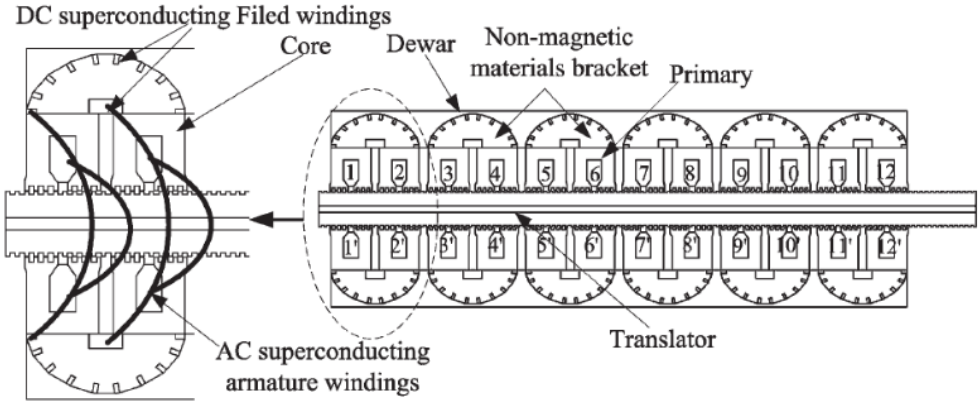

(a)

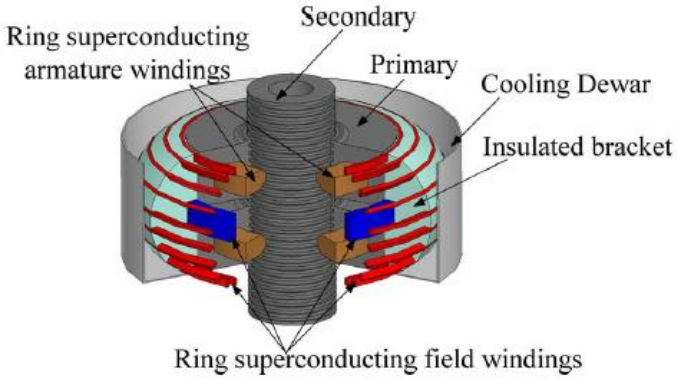

(b)

Fig. 1-21 (a) Structure of the TSFSLG. (b) Structure of the superconducting windings.

1.5 Conclusion

In this chapter, the WEC prototypes and the main power take-off devices are presented, which indicates that: 1) a large amount of WEC prototypes has been proposed and manufactured, however, the technology of capturing the energy contained in waves is still at the R&D stage, and only a small range of devices have been tested at large scale; 2) for the developed WECs, gearbox or hydraulic systems are often used to interface the slow moving prime mover to the conventional high-speed rotary machines, which increase maintenance costs, and maintenance in sea water is more difficult, expensive and limited by weather conditions; 3) direct-drive devices are considered to be more reliable and robust than gearbox or hydraulic systems, which allow generators to respond directly to the movement of ocean.

Nevertheless, due to the low moving speed of waves, the PM-LGs used in direct-drive WECs are physically large and heavy. Besides, the PM-LGs suffer from the drawbacks of PM demagnetization, uncontrollable airgap flux, and high PM cost. These drawbacks brought the requirement for high current-density materials to achieve compact and light machines, and enhance the power density of LGs.

Fortunately, the high current-carrying capability of HTS coils makes it possible to produce high magnetic flux density when they are adopted to electrical machines, which leads to light machine with small volume. Fundamental properties of superconductors, development of HTSs, and application of HTSs to electric power equipment are introduced, which show the state-of-the-art of HTS technologies. The advantages of HTS machines have been demonstrated in ship-propulsion systems, direct-drive wind turbines, electromagnetic launch systems, and Maglev trains. And the successful development and testing of these machines have paved the way for developing HTS-LGs for WECs.

Two HTS-LGs proposed for WECs are presented, despite their advantages of light translator and stationary both armature windings and HTS field windings, we suspect that it may need long time to launch the large-scale practical test facilities of these machines due to their possible drawbacks of complex structure, high AC loss of HTSs, and heavy iron cores.

Chapter II Ocean waves and WEC systems

2.1 Ocean wave parameters

Waves at different places have certain character and energy density. WECs should be designed for the specific location, taking into account the available wave energy resources there. A wave resource is typically described in terms of power per meter of wave crest length. Fig. 2-1 shows an Atlas of the global power density distribution of ocean waves. It is observed that the north and south zones have the largest wave energy resource. However, Europe and Australia have the best sites for capturing wave power because the large wave energy resource and the short distance from deploying sites to users.

In deep water, periods of ocean waves are within the interval from 5 to 15 s, with corresponding wavelengths from 40 to 350 m [91], where are suitable for large-scale WEC devices. Wave height and wave period are the most two important parameters, which determines the wave power density [86][92]. For WEC application, these two parameters determine the peak velocity of heaving buoys, which directly affects the induced voltage characteristics. Besides, wave height affects the oscillating height of the buoy, also the stroke of LGs, thus determining the length of LGs used in WECs.

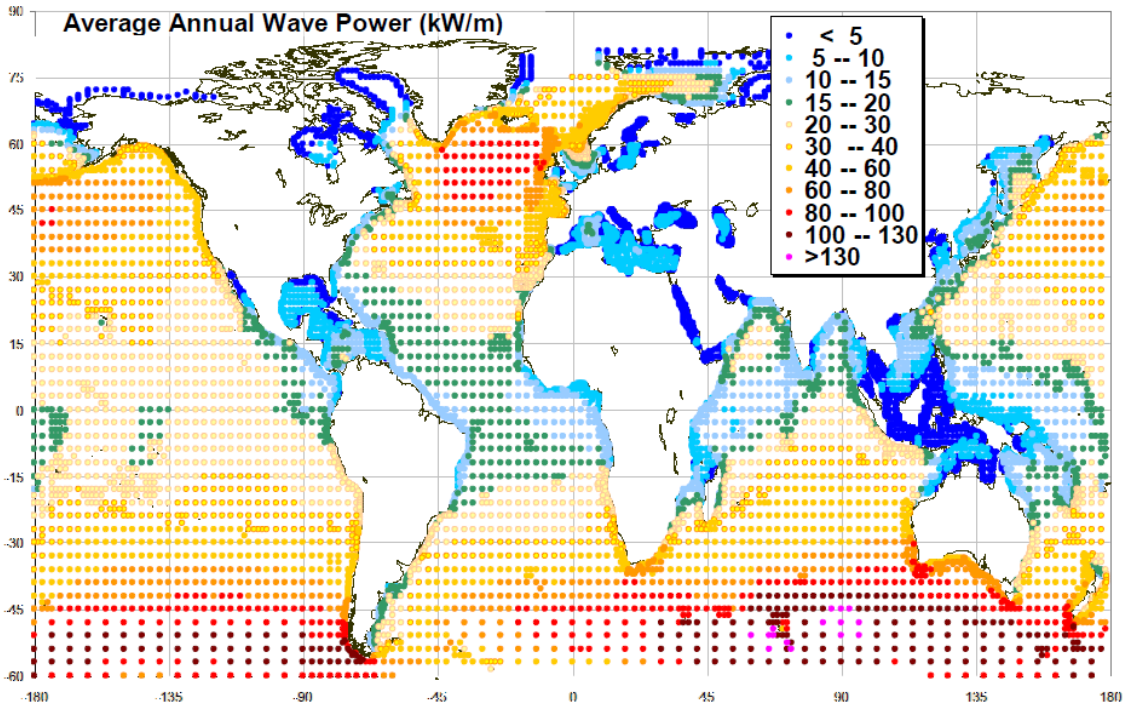

Fig. 2-1 Approximate global power density distribution of ocean waves (kW/m of wave crest length) [© WorldWaves data] [93].

Fig. 2-2 exhibits the mean significant wave height H_{m0} worldwide for 1997 to 2006, which is based on statistical analysis of the 10-year WorldWaves time series. H_{m0} is an important parameter for the statistical distribution of ocean waves, which is higher than the most common waves, however, it is possible to encounter a wave that is much higher than the significant wave. From Fig. 2-2, it is observed that mean H_{m0} in Atlantic Ocean and South Pacific Ocean is up to 4 m, while off the west coast of Ireland and the southwest coast of Australia the mean H_{m0} is about 3-3.5 m. According to Ref. [94] and Fig. 2-1, the estimated average wave power around Ireland and Southwest Australis is greater than 50 kW/m.

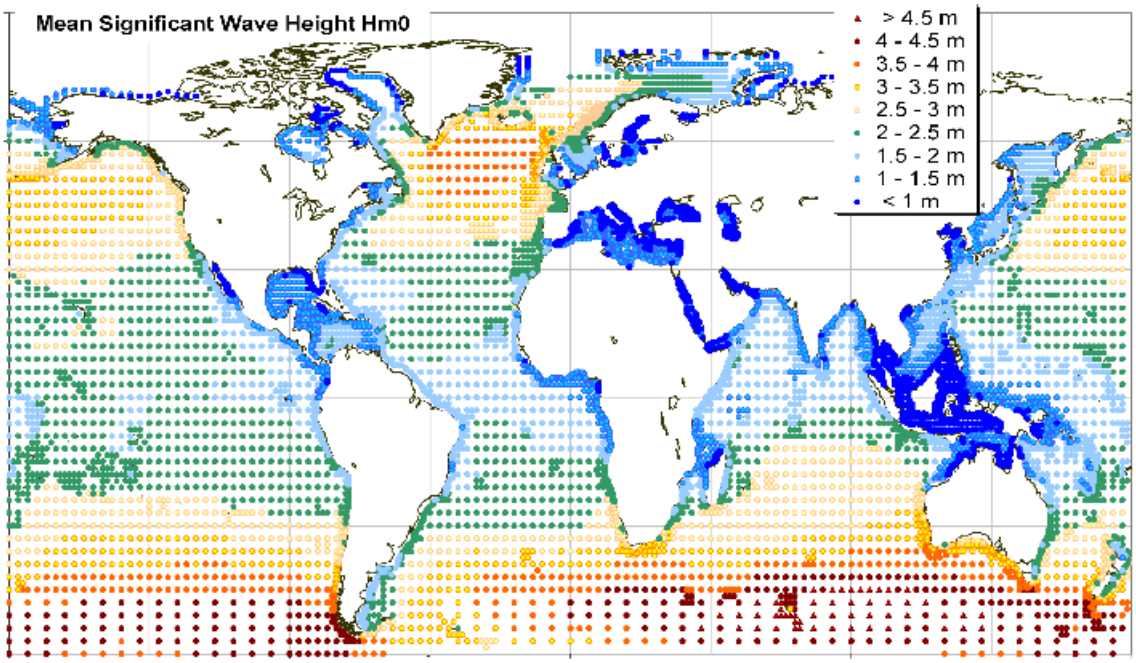

Fig. 2-2 Mean significant wave height for 1997 to 2006 in all WorldWaves grid points worldwide [© WorldWaves data] [95].

In addition, Tables 2-1 and 2-2 show the occurrence of waves with certain parameters and energy flux density transported by waves at Shannon, Atlantic Ocean near south – west coast of Ireland [96], where was chosen in Ref. [96] to simulate an octagonal-shaped linear generator. In those studies, harmonic sinusoidal wave propagation is considered with 5 m wave height and 11 s wave period because this kind of waves take place during 131.4 h per year at Shannon. Moreover, these waves have large energy as seen from Table 2-2.

In our study, we prefer choosing the waves with 4 m in height and 10 s in period, which occur more frequently than the waves with 5 m in height and 11 s in period at Shannon, even a little lower energy. As mentioned previously, the mean H_{m0} off the West coast of Ireland and the Southwest coast line of Australia is 3-3.5 m, which also reveals that the 4 m waves occur more frequently than 5 m waves in these regions. Therefore, studies in this thesis are

Table 2-1 Occurrence of significant wave height *H* and wave period *T* per year at Shannon. [96]

H (m)	*T* (s)															
	0	2	3	4	5	6	7	8	9	10	11	12	13	14	15	18
	2	3	4	5	6	7	8	9	10	11	12	13	14	15	18	20
0.0–0.5	0	0	0	0	0	0	0	0	0	0	0	0	0	0	0	0
0.5–1.0	0	0	0	0	**1**	**4**	**6**	**1**	0	0	0	0	0	0	0	0
1.0–1.5	0	0	0	0	**11**	**32**	**55**	**26**	**3**	0	0	0	0	0	0	0
1.5–2.0	0	0	0	0	**6**	**40**	**51**	**44**	**25**	**5**	0	0	0	0	0	0
2.0–2.5	0	0	0	0	**1**	**23**	**38**	**36**	**30**	**19**	**3**	0	0	0	0	0
2.5–3.0	0	0	0	0	0	**6**	**30**	**32**	**36**	**20**	**7**	**1**	0	0	0	0
3.0–3.5	0	0	0	0	0	0	**14**	**27**	**22**	**19**	**11**	**2**	0	0	0	0
3.5–4.0	0	0	0	0	0	0	**3**	**18**	**19**	**16**	**13**	**7**	**1**	0	0	0
4.0–4.5	0	0	0	0	0	0	0	**8**	**17**	**15**	**12**	**7**	**2**	**1**	0	0
4.5–5.0	0	0	0	0	0	0	0	**3**	**12**	**15**	**10**	**7**	**3**	**0**	0	0
5.0–5.5	0	0	0	0	0	0	0	**1**	**8**	**11**	**8**	**6**	**2**	**1**	0	0
5.5–6.0	0	0	0	0	0	0	0	0	**4**	**9**	**6**	**5**	**2**	**1**	0	0
6.0–6.5	0	0	0	0	0	0	0	0	**1**	**6**	**6**	**5**	**3**	**1**	**1**	0
6.5–7.0	0	0	0	0	0	0	0	0	0	**3**	**4**	**4**	**3**	**1**	0	0
7.0–7.5	0	0	0	0	0	0	0	0	0	**1**	**4**	**3**	**2**	**1**	0	0
7.5–8.0	0	0	0	0	0	0	0	0	0	0	**1**	**2**	**1**	**1**	**1**	0
8.0–8.5	0	0	0	0	0	0	0	0	0	0	**1**	**2**	**1**	**1**	0	0
8.5–9.0	0	0	0	0	0	0	0	0	0	0	0	**2**	**1**	0	0	0
9.0–9.5	0	0	0	0	0	0	0	0	0	0	0	**1**	**1**	**1**	0	0
9.5–10	0	0	0	0	0	0	0	0	0	0	0	**1**	**1**	**1**	0	0
10–11	0	0	0	0	0	0	0	0	0	0	0	0	**1**	0	**1**	0
11–12	0	0	0	0	0	0	0	0	0	0	0	0	0	0	0	0

Table 2-2 Energy table for significant wave height *H* and period *T* per year at Shannon (energy unit is [kWh/m year]) [96].

H (m)	*T* (s)												
	4	5	6	7	8	9	10	11	12	13	14	15	18
	5	6	7	8	9	10	11	12	13	14	15	18	20
0–0.5	0	0	0	0	0	0	0	0	0	0	0	0	0
0.5–1.0	0	**13.5**	**64**	**111**	**20.9**	0	0	0	0	0	0	0	0
1.0–1.5	0	**414**	**1433**	**2823**	**1512**	**195**	0	0	0	0	0	0	0
1.5–2.0	0	**443**	**3488**	**5131**	**5017**	**3186**	**704**	0	0	0	0	0	0
2.0–2.5	0	**122**	**3315**	**6320**	**6785**	**6320**	**4424**	**765**	0	0	0	0	0
2.5–3.0	0	0	**1292**	**7453**	**9010**	**8182**	**6956**	**2666**	**414**	0	0	0	0
3.0–3.5	0	0	0	**4845**	**10,618**	**9669**	**9230**	**5852**	**1157**	0	0	0	0
3.5–4.0	0	0	0	**1386**	**9424**	**11,118**	**10,348**	**9208**	**5389**	**832**	0	0	0
4.0–4.5	0	0	0	0	**5380**	**12,777**	**12,640**	**10,918**	**6922**	**2136**	**1147**	0	0
4.5–5.0	0	0	0	0	**2520**	**11,266**	**15,565**	**11,365**	**8647**	**4002**	0	0	0
5.0–5.5	0	0	0	0	**1026**	**9175**	**13,944**	**11,107**	**9054**	**3260**	**1750**	0	0
5.5–6.0	0	0	0	0	0	**5503**	**13,685**	**9992**	**9051**	**3910**	**2100**	0	0
6.0–6.5	0	0	0	0	0	**1625**	**10,779**	**11,805**	**10,693**	**6929**	**2481**	**2823**	0
6.5–7.0	0	0	0	0	0	0	**6286**	**9180**	**9978**	**8082**	**2894**	0	0
7.0–7.5	0	0	0	0	0	0	**2417**	**10,590**	**8633**	**6216**	**3338**	0	0
7.5–8.0	0	0	0	0	0	0	0	**3025**	**6577**	**3551**	**3815**	**4341**	0
8.0–8.5	0	0	0	0	0	0	0	**3428**	**7453**	**3995**	**4323**	0	0
8.5–9.0	0	0	0	0	0	0	0	0	**8384**	**4527**	0	0	0
9.0–9.5	0	0	0	0	0	0	0	0	**4685**	**5059**	**5434**	0	0
9.5–10	0	0	0	0	0	0	0	0	**5205**	**5621**	**6037**	0	0
10–11	0	0	0	0	0	0	0	0	0	**6519**	0	**7968**	0
11–12	0	0	0	0	0	0	0	0	0	0	0	0	0

decided to be done based on the wave assumptions of 4 m in height and 10 s in period. In addition, ideal waves are considered, which are assumed to be moved in a sinusoidal form as a function of time in the vertical direction.

2.2 Wave energy conversion system

In this study, a concept of a direct-drive WEC device is proposed. Fig. 2-3 displays the electrical system of the WEC. The WEC device mainly consists of a cylindrical buoy and a tubular linear generator (TLG). The buoy is directly coupled with translator of the TLG, and stator of the TLG is attached to seabed. When the translator moves up and down together with the reciprocating buoy, which is directly driven by the waves, voltage can be induced in the TLG. The induced output power is connected to the grid after the signal processing. Here, there are two points which are needed to be emphasized:

1) The translator could be located inside or outer side of the TLG, and designed longer or shorter than the stator depending on some considerations of generator performance and cost.
2) As the buoy velocity in the vertical direction varies with time, electrical frequency of the TLG varies with time in every wave cycle. As a matter of fact, generators producing such kind of output power cannot be directly connected together. And such induced voltage should be first rectified to a direct one.

Moreover, novelties of the WEC device are clarified as follows:

- The buoy is chosen as a cylindrical one to extract more power from the ocean than other shapes, and more maximum output power can be obtained by simply enlarging the buoy;
- The tubular structure is adopted in consideration of reducing the leakage reactance of armature windings and the attractive force between stator and translator, which reduces the bearing load.

About the WEC system, three aspects are involved in this thesis, which are the buoy movement, the electrical design of the TLGs, and the output voltage characteristics of the WEC. Among them, electrical design of the TLGs and their performances are mainly focused on.

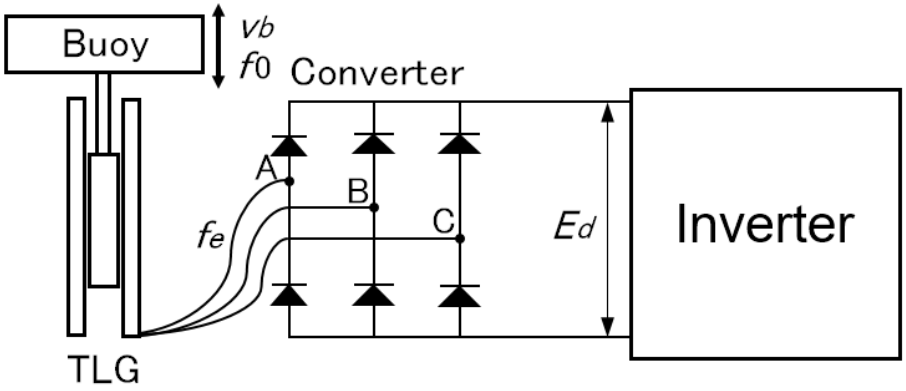

Fig. 2-3 Electrical system of the direct-drive WEC.

2.3 Buoy movement

Buoy of a WEC device plays an important role in power extraction. Dimension of the cylindrical buoy is decided by analyzing its movement during operation. For the floating buoy and translator, the following equation is from the force balance between gravitation and buoyancy.

$$(m_{tr} + m_b)g = \rho g(V_{tr} + hS) \tag{2-1}$$

where m_{tr} and m_b represent the masses of translator and buoy, respectively, which depends on the design results of the LG and the buoy. g is gravity acceleration. ρ is the mass density of sea water. V_{tr} is the volume of the translator. h represents the submerged depth in the sea water of the buoy in the case that the device is in still water. And S is the cross section of the cylindrical buoy.

We assume the wave moves in a sinusoidal form of displacement as a function of time in the vertical direction. The displacement of sea surface is expressed as

$$x_s = A\sin 2\pi f_0 t \tag{2-2}$$

where A and f_0 are the amplitude and vertical movement frequency of waves, respectively. It is worth noting that the "wave height" is the height difference between a crest and a neighboring trough, which is twice the wave amplitude.

Per Eq. (2-2), the vertical movement velocity of sea surface is expressed as

$$v_s = dx_s/dt = 2\pi f_0 A\cos(2\pi f_0 t)\,. \tag{2-3}$$

Consequently, maximum velocity of sea surface is

$$v_{sm} = 2\pi f_0 A\,. \tag{2-4}$$

Next, ascent or descent force of translator and buoy, which is equivalent to input power to the linear generator, can be expressed as

$$F_l = \rho gSl \tag{2-5}$$

where l represents the height of subtracting the h from the displacement difference between the buoy bottom and the sea surface during operation.

On the other hand, reaction force of the linear generator is

$$F_r = P(v_b)/v_b \tag{2-6}$$

where v_b is the velocity of translator part and buoy. $P(v_b)$ represents the output power of linear generator.

In the case of neglecting the friction loss between the buoy and the seawater, $F_l = F_r$. Then, l is expressed as

$$l = P(v_b)/(v_b\,\rho gS)\,. \tag{2-7}$$

For synchronous linear generators, in the cases that the induced voltage E and armature

current I are proportional to v_b, the terminal voltage V is also proportional to v_b, and the ratio of output power $P(v_b)$ to maximum output power P_m is

$$P(v_b)/P_m = (v_b/v_{bm})^2 \tag{2-8}$$

where v_{bm} is the maximum velocity of translator part and buoy.

Consequently, referring to (2-2), (2-7), and (2-8), the displacement of bottom surface of buoy can be expressed as

$$x_b = x_s - h - l = A\sin 2\pi f_0 t - h - \frac{P_m}{v_{bm}^2 \rho g S} \cdot \frac{dx_b}{dt} \tag{2-9}$$

where the acceleration power is neglected, which is much smaller than the generator output power. Then, the following equation is obtained.

$$\frac{C}{v_{bm}^2} \cdot \frac{dx_b}{dt} + x_b = A\sin 2\pi f_0 t - h \tag{2-10}$$

where,

$$C = P_m/(\rho g S)\,. \tag{2-11}$$

By solving the differential equation (2-10), we obtain

$$x_b = \frac{A}{\sqrt{(2\pi f_0 C/v_{bm}^2)^2 + 1}} \cdot \sin(2\pi f_0 t - \varphi) - h \tag{2-12}$$

where,

$$\varphi = \tan^{-1}(2\pi f_0 C/v_{bm}^2)\,. \tag{2-13}$$

Consequently,

$$v_b = \frac{dx_b}{dt} = \frac{2\pi f_0 A}{\sqrt{(2\pi f_0 C/v_{bm}^2)^2 + 1}} \cdot \cos(2\pi f_0 t - \varphi)\,. \tag{2-14}$$

And the maximum velocity of buoy v_{bm} is derived as

$$v_{bm} = \sqrt{\frac{v_{sm}^2 + \sqrt{v_{sm}^4 - 4\times(2\pi f_0 C)^2}}{2}}\,. \tag{2-15}$$

According to above analysis, the waveforms of displacement and velocity of sea surface can be plotted according to Eq. (2-2) and (2-3). To plot the waveforms of buoy bottom displacement and buoy velocity, firstly, the h (submerged height of the buoy in still water) and C (determined by maximum output power and cross-sectional area of the buoy) should be decided. For instance, for a 1 MW WEC operating at 4 m waves, the total height of the buoy is approximately 4 m, and the h can be calculated according to Eq. (2-1) with a given radius of the buoy, thickness of the plates to compose the buoy, and mass density of the buoy material, where m_{tr} is numerically obtained from the electrical design of the LG. And C is

obtained according to Eq. (2-11). Consequently, per Eq. (2-12) and (2-14), the displacement and velocity of buoy bottom during a cycle operation can be obtained. Fig. 2-4 shows the displacement and velocity waveforms of buoy bottom and sea surface of a 1 MW WEC composed of a HTS-TLG and an iron buoy, in the case that A = 2 m, f_0 = 0.1 Hz, $S = \pi \times 6^2$ m^2, buoy height of 4 m, and translator volume and mass obtained from the design results of the HTS-TLG referring Chapter IV. It is shown that the maximum submerged displacement of the buoy bottom surface is 3.0 m, then, the total height of the buoy is decided as 3.5 m considering some margins.

From Fig. 2-4, it is observed that the buoy moves up and down with the same frequency but a lower magnitude and velocity than those of waves, due to the electric power is taken off. Magnitude of the buoy is about 1.84 m, and its maximum velocity is 1.16 m/s, which is decreased by 8 % compared to that of the sea surface due to the electric power is taken off. Moreover, it is noted that the moving part (the buoy and the translator of the HTS-LG) should be heavy so that the buoy bottom is immersed deeply enough under seawater during operation. However, mass of generator translator is desired to be as light as possible to reduce the mechanical tension on the buoy.

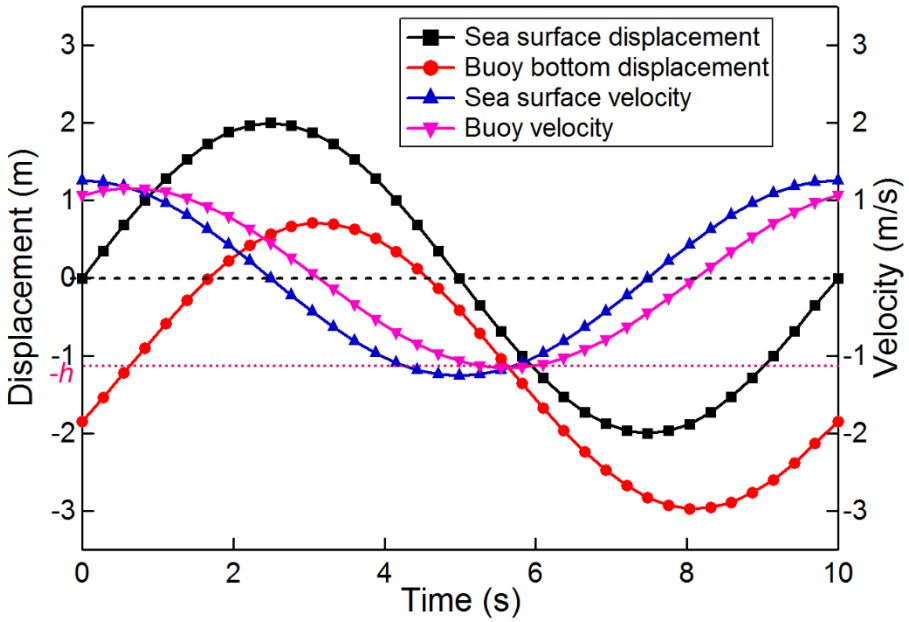

Fig. 2-4 Displacement and velocity of sea surface and buoy bottom.

2.4 Maximum output power and buoy size

The ratio of maximum output power P_m to the cross-sectional area of the buoy S plays a significant role to the amount of extracted energy. The buoy should be large enough to absorb the maximum wave energy, but on the other hand, a substantially large buoy could increase

the construction cost and reduce the mechanical stability. In the following, the relation of maximum output power and buoy size is studied.

Firstly, assuming $v_{bm}/v_{sm} = \cos\alpha$ in Eq. (2-15), we obtain

$$v_{sm}^2 \sin 2\alpha = 4\pi f_0 C \tag{2-16}$$

Referring to Eq. (2-4) and (2-11), the following expression is deduced

$$\begin{aligned} P_m &= \pi\rho g f_0 A^2 S \cdot \sin 2\alpha \\ &= \pi^2 \rho g f_0 A^2 r^2 \cdot \sin 2\alpha \end{aligned} \tag{2-17}$$

where r is the radius of the heaving buoy.

Eq. (2-17) indicates that radius of the buoy has a significant influence on the maximum output power. Moreover, the P_m is proportional to $f_0 A^2$ when the buoy size is decided, which means that the amplitude of waves has bigger influence on the maximum output power compared to the wave frequency. In the following, the way of determining the buoy size is first studied, then, the influence of wave amplitude and frequency on the maximum output power is analyzed.

To obtain the required output power, buoy size can be determined according to Eq. (2-17). For instance, if $(P_m)_{\max} = \pi\rho g f_0 A^2 S$ is constant, the value of $P_m / (P_m)_{max}$ varies from 0.866 to a peak value of 1 when α is from $\pi/6$ to $\pi/4$. Considering some margins, we suggest $P_m / (P_m)_{max}$ being 0.866, as a result, the Eq. (2-17) can be expressed as

$$P_m = 83.8 \times f_0 A^2 r^2 [\text{kW}]. \tag{2-18}$$

Per Eq. (2-18), Fig. 2-5 exhibits the variation of maximum output power P_m of the TLG with wave amplitude A in the cases that buoy radius is 6 m, 5 m, 4 m, and 3 m, respectively. Here, it is worth mentioning that wave frequency varies with wave amplitude, as listed in Table I [96][97], in which the maximum output power for the buoy with radius of 6 m is also shown. It is further noted that the buoy with radius of 6 m can obtain 1.2 MW maximum output power in the case that $f_0 = 0.1$ Hz and $A = 2$ m. Considering the friction loss of sea water, it is decided to use the buoy with radius of 6 m to get the 1 MW maximum output power in Chapter IV. Moreover, Fig. 2-5 shows that the P_m increases linearly with the increase of A when $A \geq 1$ m, because the value of $f_0 A^2$ increases linearly with the increasing A when $A \geq 1$ m. Referring to Fig. 2-5, it is easy to decide the maximum output power and the buoy size by measuring the wave amplitude in a certain location.

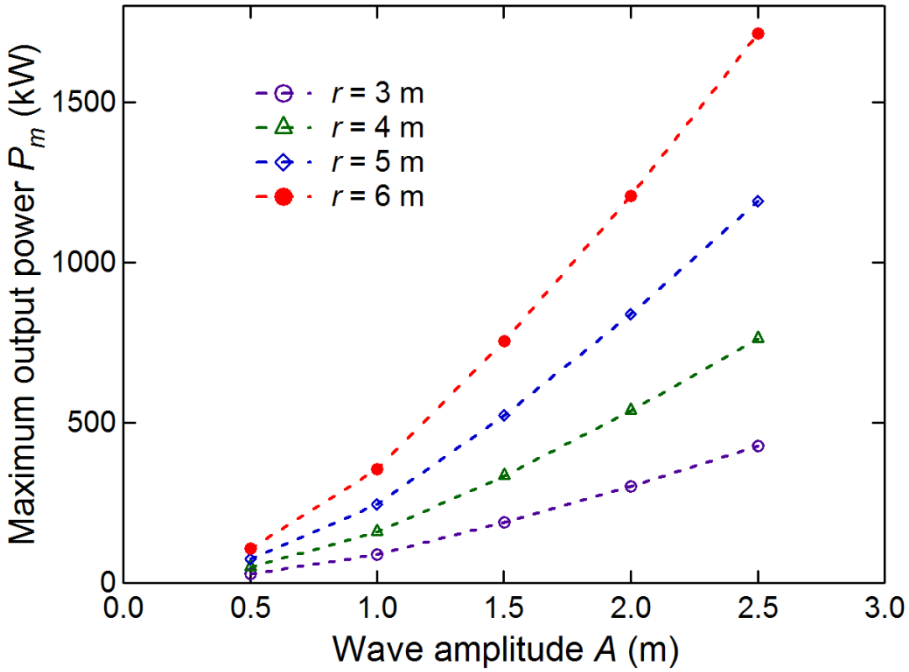

Fig. 2-5 Variation of maximum output power with wave amplitude under different buoy radii.

Table 2-3 Sea condition and maximum output power for the buoy with radius of 6 m.

Wave height (m)	Period (s)	Maximum output power (kW)
0.5	7	27
1.0	7	108
1.5	8	212
2	8.5	355
2.5	8.5	554
3	9	754
3.5	9.5	972
4	10	1206
4.5	11	1388
5	11	1713

2.5 Conclusion

In this chapter, ocean wave characteristics are firstly investigated to ensure that the studies in this thesis are carried out based on realistic wave data. The global power density distribution of ocean waves and the Atlas of mean significant wave height imply that there are some locations containing a plentiful wave resource and suitable for deploying large-scale WECs, like the regions off the west coast of Ireland and the southwest coast of Australia. The waves of 4 m in height and 10 s in period frequently occur in these regions, therefore, the studies of this thesis are decided to be done based on the wave assumptions of

4 m in height and 10 s in period, and ideal sinusoidal waves are considered.

Then, electrical system of a direct-drive WEC is displayed, and the structural merits of the WEC device are highlighted. The WEC features a cylindrical buoy to extract significant output power and a TLG to reduce the attractive force between stator and translator and the leakage reactance of armature windings.

Next, based on the wave assumptions, the buoy movement during one-cycle operation is analyzed. It is demonstrated that:

- the buoy moves with the same frequency but lower magnitude and velocity than those of waves;
- the buoy should be heavy enough to extract more power from ocean waves.

At last, the relation of maximum output power and buoy size is analyzed, which shows an easy way of determining the maximum output power and the buoy size by measuring the wave amplitude in a certain location.

Chapter III Electrical design study of PM-TLGs for WECs

This chapter aims to present the electrical design of 1 MW PM tubular linear generators (PM-TLGs) for WECs. Firstly, conceptual structure of a WEC is proposed, which mainly consists of a cylindrical buoy and a PM-TLG. The main contents are about the self-developed electrical design method of PM-TLGs, including the design process, the determination of main machine parameters, the way of calculating leakage coefficient and the new method of evaluating PM operating point. Design results of three PM-TLGs with different PM thicknesses are presented, with magnetic flux analyzed to verify the correctness of the design results.

3.1 Conceptual structure of a WEC with a permanent magnet tubular linear generator (PM-TLG)

Conceptual structure of a WEC is proposed, which consists of a cylindrical buoy, a PM-TLG and a base, as displayed in Fig. 3-1 (a). Stator of the PM-TLG is attached to the base, which is grounded to seabed. Translator is connected to the buoy. When wave moves up and down, the translator is forced up and down by the heaving buoy, in which way, the energy generated by vertical motion of sea water can be directly converted to electrical power without gearbox or hydraulic systems.

Fig. 3-1 (b) depicts the cross section of the PM-TLG. PMs are mounted with alternating polarities on the translator, and the stator containing conventional copper windings is attached to the seabed. The advantages of the proposed PM-TLG are as follows.

- The stator containing armature windings is fixed to the seabed, which can avoid the movement of cables used for transferring the generated electrical power.
- The PM part is designed shorter that the stator for the sake of saving expensive PMs.
- The light PM part is connected to the heaving buoy as a translator to reduce the mechanical tensions on the buoy.
- The PM part is located outside of the stator, which benefits for increasing the magnetic flux of field PMs and reducing the resistance loss of armature windings, compared to the inner PM structure.

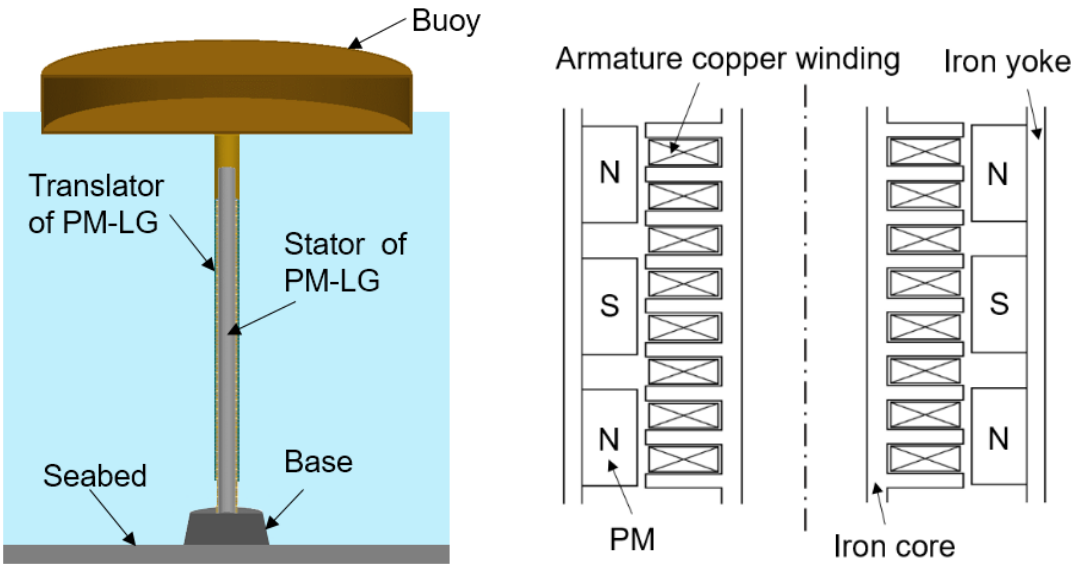

(a) (b)

Fig. 3-1 (a) Conceptual structure of the proposed WEC device. (b) Partial cross section of the PM-TLG.

3.2 Electrical design method of PM-TLGs

3.2.1 Basic specifications and design process

The generator and the buoy are sized according to the wave parameters. Basic specifications of the PM-TLG are selected considering the assumed wave height of 4 m and frequency of 0.1 Hz, which are listed in Table 3-1. The maximum output power is decided as 1 MW taking into account the losses that must be supplied by the buoy, converter efficiency and generator efficiency. Total air gap length is decided as a relatively large value of 12 mm in consideration of the long air gap structure and the efficient water cooling of linear generators. Mechanical clearance between outer surface of the stator and inner surface of the translator is 8 mm. Main machine parameters, such as number of PM poles, pole pitch, PM thickness, electric loading, PM width/pole pitch, and armature conductor current density are given within a certain range, which are decided by studying their influence on basic generator performance.

Fig. 3-2 shows the electrical design flowchart of PM-TLGs. Step 1 illustrates basic specifications. Machine parameters of armature and translator part, as well as the air gap flux density are described in step 2-6. The magnetomotive force (MMF) under no-load condition is also calculated in step 6. The MMF under load condition is obtained in step 7-8. Then, a three-dimensional (3-D) model is established to analyze magnetic field and calculate two leakage coefficients, which play key roles on generator performance and make the design results adequate, in step 9. The generator performance is finally obtained in step 10.

Table 3-1 Basic specifications of a 1 MW PM-TLG.

Item	Value
Maximum output power (MW)	1
Wave height (m)	4
Wave frequency (Hz)	0.1
Terminal voltage (V)	660
Line current (A)	875
Airgap length (mm)	12
Slot number / pole / phase N_{pp}	1
Number of PM poles	24-72
Pole pitch (mm)	131-236
PM thickness (mm)	47.5-72.5
Electric loading (A/cm)	800-1200
PM width/pole pitch	0.65-0.85
Current density of armature conductors (A/mm^2)	1.75-4.25
Magnetic flux density in armature core back (T)	1.30
Magnetic flux density in PM yoke (T)	1.45

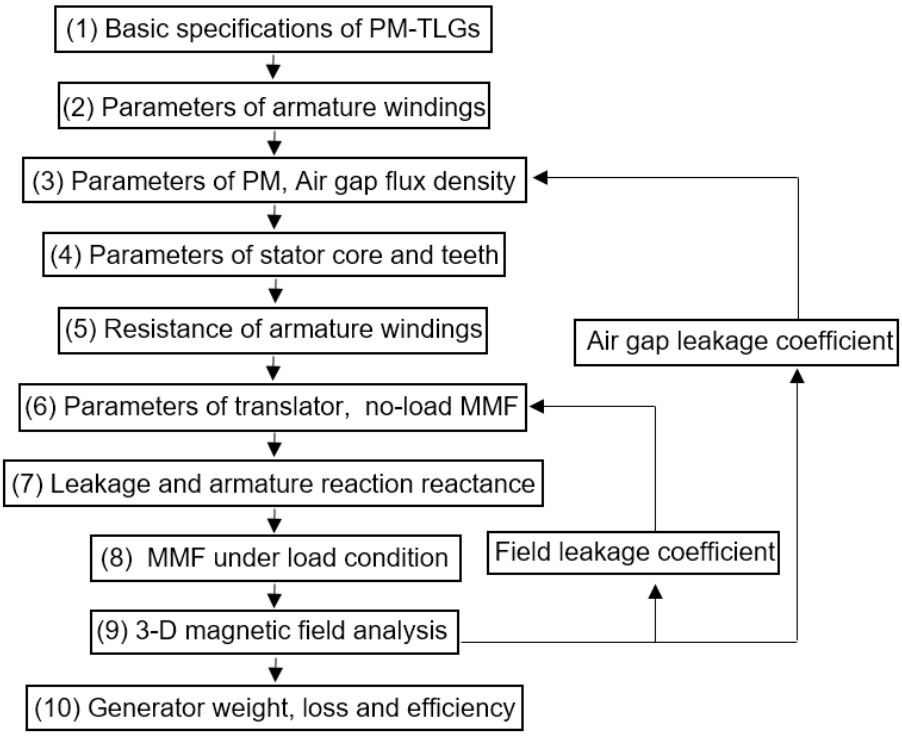

Fig. 3-2 Electrical design flowchart of PM-TLGs.

3.2.2 Determination of main machine parameters

To get the efficient PM-TLG with less weight and cost, the influence of main machine parameters on the basic generator performance is studied, and the main machine parameters are determined iteratively considering the generator weight, PM weight, and generator efficiency, which is illustrated as follows.

A. Influence of number of poles on generator performance

Firstly, the influence of number of poles on the basic generator performance is studied, and the results are shown in Fig. 3-3. We found that the generator efficiency increases with the increasing number of poles, but both generator weight and PM weight decrease. This is because the ratio of the effective armature length, which generates the induced voltage, to the total armature length is higher with a larger number of poles. Besides, the increasing number of poles leads to long generators with smaller diameter due to the determined line voltage. So, in the viewpoint of lighter generators and PMs, as well as higher generator efficiency, the larger number of poles is better. However, too long PM-TLGs have the problems of mechanical strength and attachment. Therefore, the number of PM poles of 42 is preliminarily decided considering the assumed allowable generator length of 11.5 m, in which case both generator weight and PM weight are relatively low, and the generator efficiency is more than 80%.

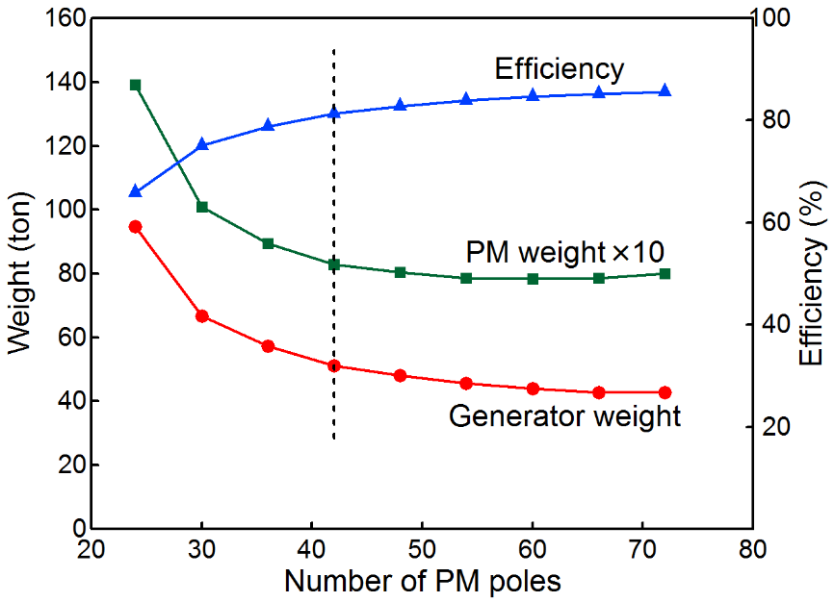

Fig. 3-3 Variation of generator weight, PM weight, and generator efficiency with respect to number of poles.

B. Influence of pole pitch on generator performance

Pole pitch directly determines the length, electrical frequency, and stator slot size of the PM-TLG. The influence of pole pitch on the basic generator performance, with a given number of PM poles of 42, is presented in Fig. 3-4. It is found that the pole pitch has a little influence on the generator weight, PM weight, and generator efficiency if it is beyond 184 mm, in which case the PM-TLG exhibits relatively light weight, low PM weight, and high efficiency.

Moreover, the number of poles and the pole pitch are given with different values, and each set of the number of poles and pole pitch keeps the same generator length of about 11.5 m. Fig. 3-5 shows the variation of generator weight, PM weight, and generator efficiency with respect to pole pitch. It is worth noting that, different with Fig. 3-4, the number of PM poles is different for each set of data, which is annotated under the generator weight line in Fig. 3-5. It is seen that in the case that pole pitch is 184 mm with 42 PM poles, the generator has lightest PMs, highest efficiency, and a pretty light generator weight. So, pole pitch of 184 mm and number of PM poles of 42 are decided.

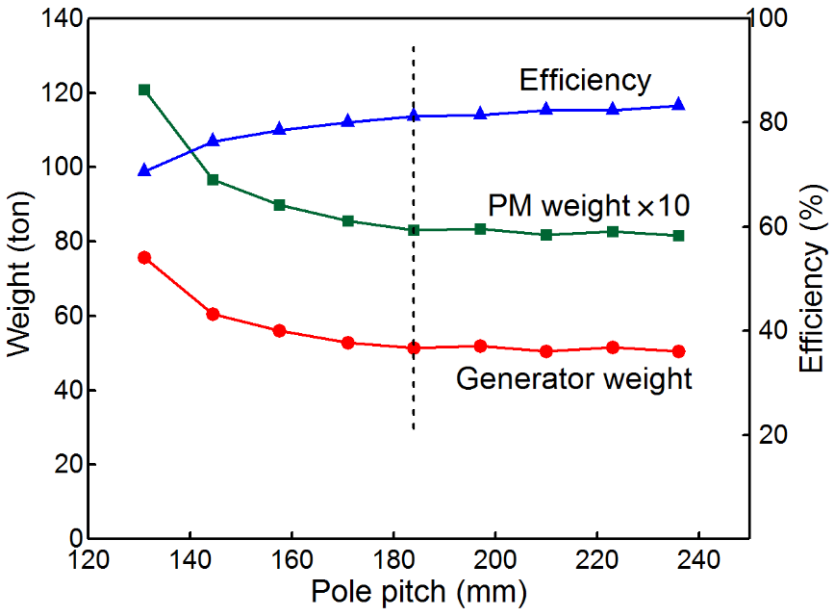

Fig. 3-4 Variation of generator weight, PM weight, and generator efficiency with respect to pole pitch (with 42 PM poles).

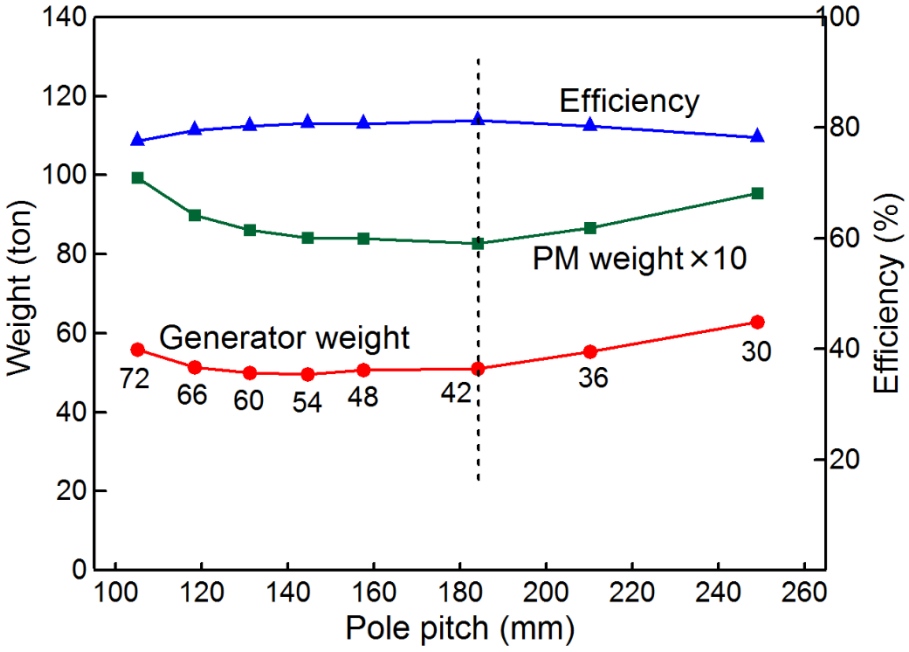

Fig. 3-5 Influence of pole pitch and number of poles on generator weight, PM weight, and generator efficiency (generator length about 11.5 m).

C. Influence of PM thickness on generator performance

PM thickness is an important parameter, which plays a role in the reduction of generator weight and cost. Here, the PM thickness means the length of PMs along the generator radial direction. Fig. 3-6 shows the influence of PM thickness on the basic generator performance. It is observed that the generator weight decreases with the increase of PM thickness. PM weight decreases but begins to increase beyond a PM thickness of 55 mm with the increasing PM thickness. This is because for tubular PM-TLGs, the PM weight is proportional to the product of PM thickness and diameter of PM center, with a given PM width/pole pitch and number of poles. With the increase of PM thickness, the effective PM magnetic flux density increases, and the diameter of PM center decreases for a given magnetic flux per pole, as shown in Fig. 3-7, which is the relationship between diameter of stator teeth center and PM thickness. As a result, the product of PM thickness and diameter of PM center decreases due to the decreasing diameter of PM center, but begins to increase beyond a PM thickness of 55 mm due to the increasing PM thickness.

The generator efficiency increases with the increasing PM thickness, which is caused by the higher magnetic flux density of PMs and the decreased loss of armature windings. And the loss of armature windings is proportional to the diameter of stator teeth part.

As shown in Fig. 3-6, the design result with PM thickness of 60 mm shows pretty light generator weight and PM weight with a high efficiency more than 80%. Besides, thicker PMs lead to high costs. Consequently, the PM thickness is decided as 60 mm.

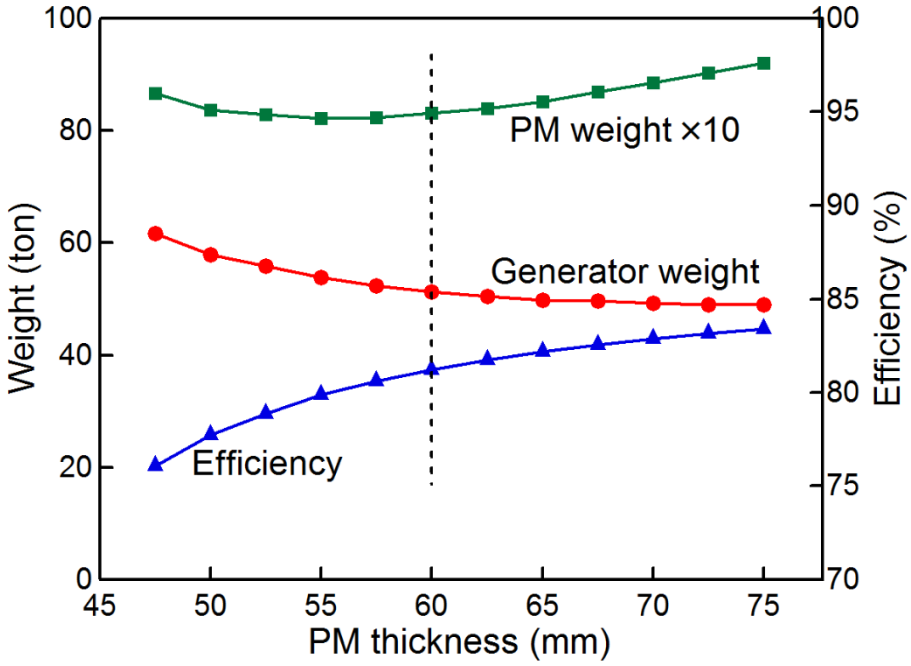

Fig. 3-6 Variation of generator weight, PM weight, and generator efficiency with respect to PM thickness.

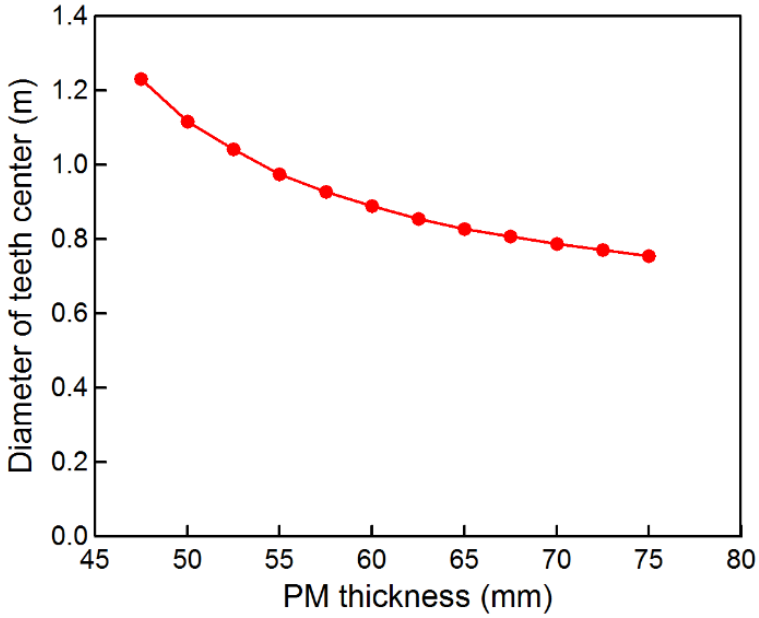

Fig. 3-7 Relationship between PM thickness and diameter of stator teeth center.

In addition, the influence of electric loading, PM width/pole pitch, and current density of armature conductors on the basic generator performance has also been studied. And the determination of the main machine parameters is summarized in Table 3-2.

Table 3-2 Determination of main machine parameters of a 1 MW PM-TLG.

Item	Value
Number of PM poles	42
Number of armature poles	62
Pole pitch (mm)	184
PM thickness (mm)	60
Electric loading (A/cm)	1000
PM width/pole pitch	0.73
Current density of armature conductors (A/mm^2)	3

3.2.3 Calculation of leakage coefficient

Two leakage coefficients caused by field windings are defined to make design results more accurate considering the large air gap of the PM-TLG. One is field leakage coefficient σ, which is expressed as $\sigma = \Phi_{ff}/\Phi_{af}$. Here, Φ_{ff} is the average interlinkage magnetic flux on field PM part, and Φ_{af} is that on armature winding part. The other one is the air gap leakage coefficient $\sigma_g = \Phi_{ff}/\Phi_{gf}$, where, Φ_{gf} is the average interlinkage magnetic flux in the air gap.

A 3-D quarter model of the one-pole 1 MW PM-TLG is established by using MagNet7.4.1.4 (Infolytica Inc.) to analyze magnetic field and calculate the leakage coefficients σ and σ_g in detail, as shown in Fig. 3-8. Magnetization direction of the PM is set as radially outward, which provides a main magnetic flux for other parts in the radial direction. The average interlinkage magnetic flux Φ_{af}, Φ_g and Φ_{ff} can be derived by calculating the magnetic flux density in different circumferential surfaces of the armature winding part, air gap region and field PM part in simulation, respectively. Furthermore, the armature leakage coefficient σ and the air gap leakage coefficient σ_g can be calculated.

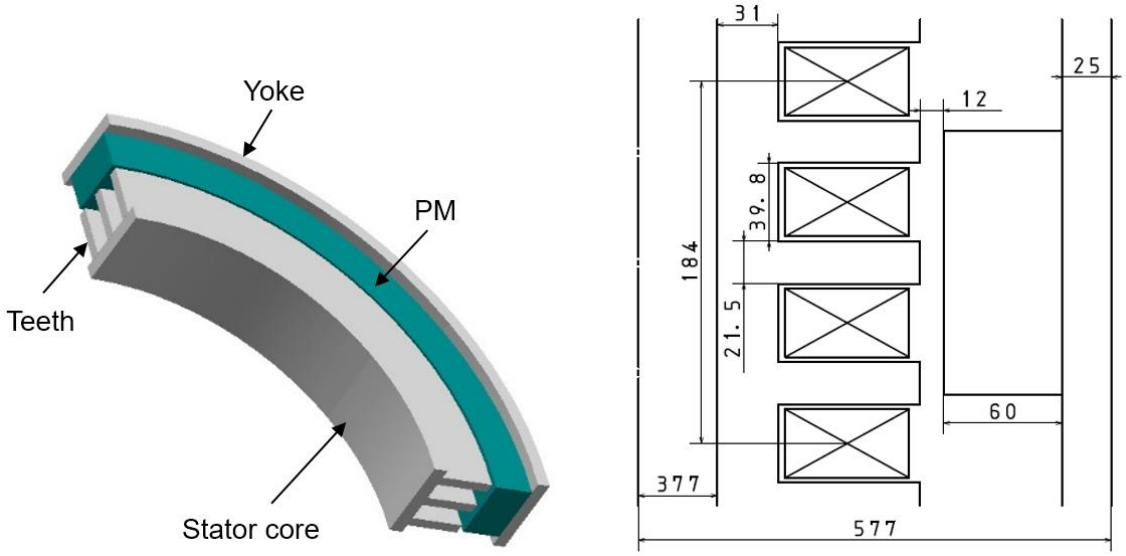

Fig. 3-8 3-D quarter model of the one-pole PM-TLG without armature windings.

In the case that PM thickness is 60 mm, the simulation work under no-load condition is conducted. Fig. 3-9 explains the way of obtaining accurate value of σ and σ_g, which exhibits the magnetic flux distribution in the different circumferential surfaces of armature winding part, air gap region, and field PM part in the "teeth center case" and the "slot center case", together with the average values and design values. Firstly, to get Φ_{ff} and Φ_{af}, the armature winding region and the PM are divided into five equal segments along their radii, respectively, and the magnetic fluxes in the circumferential surfaces of the center of each segment are calculated, as indicated by the vertical dashed lines. The magnetic fluxes are calculated under the "teeth center case" and the "slot center case", respectively. Then, the average value of magnetic flux under these two cases is feedback to modify machine parameters. The process mentioned above is repeated till the difference between the calculated values σ_n, σ_{gn} and the feedback values σ_{n-1}, $\sigma_{g(n-1)}$ from the previous step is less than an allowable value, namely, $|(\sigma_n-\sigma_{n-1})/\sigma_n|<0.01$, and $|(\sigma_{gn}-\sigma_{g(n-1)})/\sigma_{gn}|<0.01$. After iterative calculation, the σ and σ_g are obtained as 1.31 and 1.12, respectively.

Additionally, from Fig. 3-9, we observed that the magnetic flux in the PM part and air gap region are almost the same for these two cases, which are well agreed with design values. And the magnetic flux in the armature part are different due to the armature structure. However, average values of the magnetic flux under these two cases almost coincide with the design values.

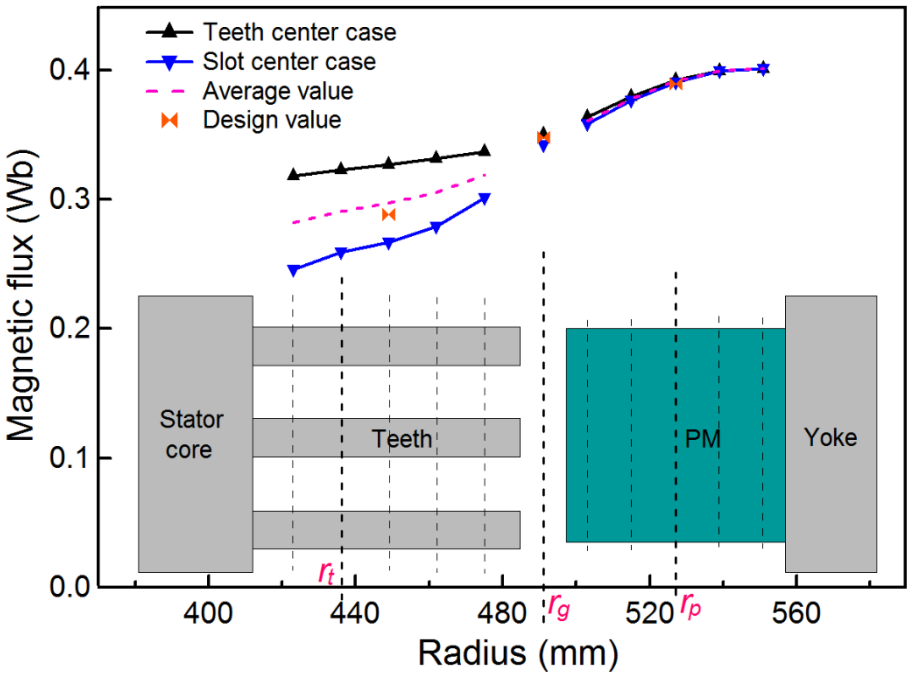

Fig. 3-9 Magnetic flux in the circumferential surfaces under different radial positions.

Fig. 3-10 displays the arrow plot of magnetic flux density under no-load condition with the calculated σ and σ_g under the "teeth center case" and the "slot center case", respectively. It is observed that the magnetic flux density in the air gap B_g is about 0.75 T, effective B_t in stator teeth about 1.8 T, B_p in PM field pole about 0.9 T.

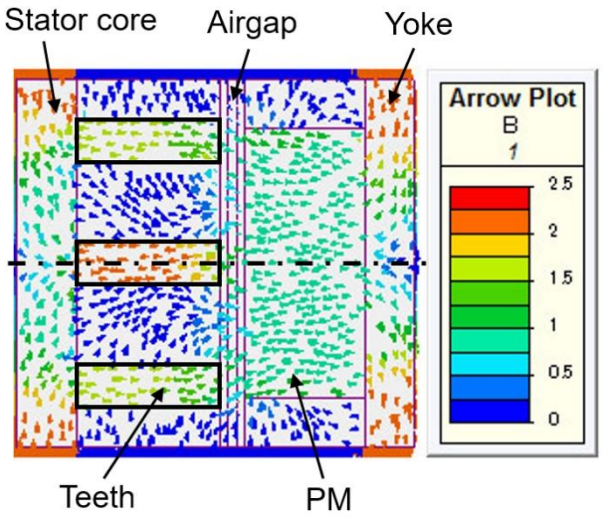

(a)

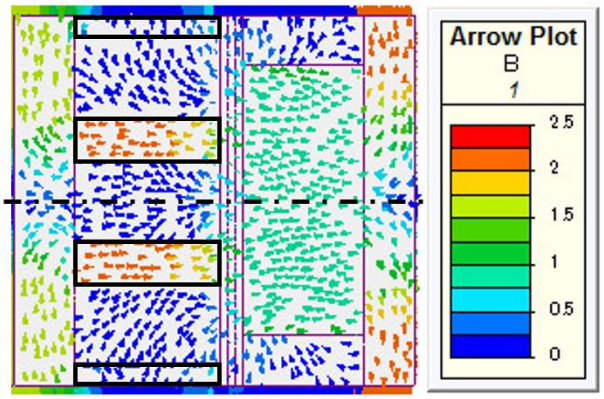

(b)

Fig. 3-10 Magnetic flux distribution (a) under the "teeth center case": the case that the center of field pole is faced to stator teeth; (b) under the "slot center case": the case that the center of field pole is faced to stator slot.

3.2.4 PM operating point

The Neodymium Iron Boron (NdFeB) magnet (HS-40AH, Hitachi Metals Co., Ltd.) is suggested being used in the PM-TLG, which has a residual magnetic flux density of 1.22 T and a coercive force of 895 kA/m at 323 K. The operating point of PM reflects the utilization of PM energy, which directly determines the amount of PMs used in the PM-TLG. The conventional way of evaluating PM operating point, which is based on the magnetic circuit,

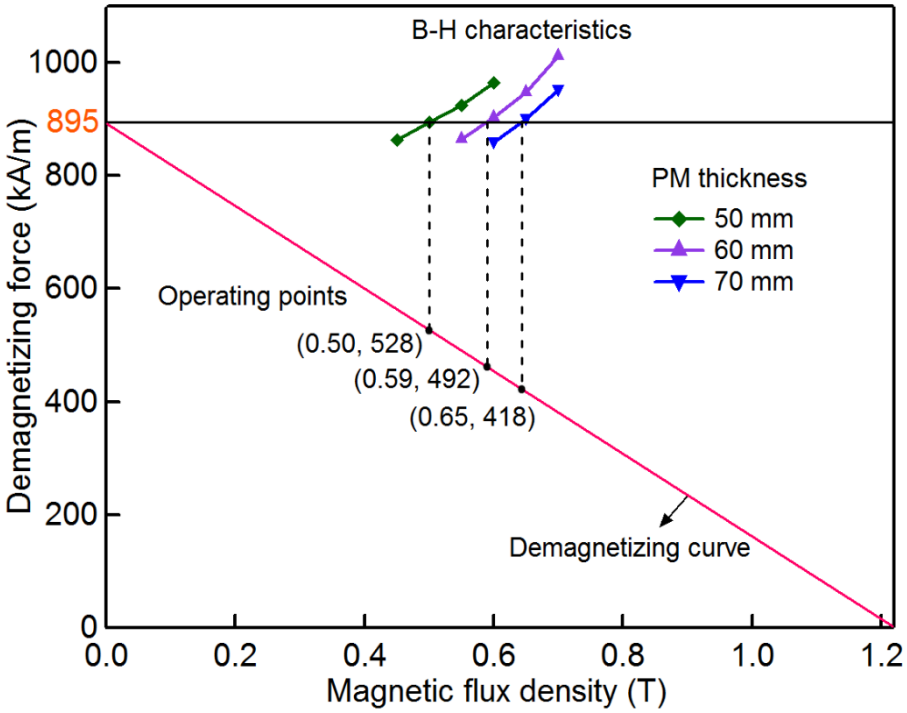

Fig. 3-11 Setting method of PM operating point.

is difficult in the cases of long air gap and magnetic saturation of irons. In order to make it easier and more accurate to evaluate PM operating point, we propose a new method, which is described as follows.

In Fig. 3-11, the PM demagnetizing curve is given, and the PM demagnetizing force H corresponding to the assumed magnetic flux density B under load condition obtained from the design results of PM-TLGs are exhibited in the cases that PM thickness are 50 mm, 60 mm, and 70 mm, respectively. The actual operating magnetic flux density B_{op} is determined from the intersection of above B-H characteristics and the PM coercive force of 895 kA/m. And the operating point is obtained on the demagnetizing curve corresponding to the B_{op}.

In the case that PM thickness is 60 mm, the operating point is determined as the magnetic flux density of 0.59 T and demagnetizing force of 492 kA/m. The thicker PMs lead to the higher magnetic flux density, which is better for generator performance. However, the thicker PMs definitely increase the amount of PMs and the cost.

3.3 Design results and discussion

3.3.1 Design results of 1 MW PM-TLGs

Design results of 1 MW PM-TLGs with different thicknesses of PMs are listed in Table 3-3. Due to the wave characteristics, the electrical frequency of the PM-TLGs is determined as 3.15 Hz. From the design results, it is observed that the PM-TLG with PM thickness of

50 mm has obvious disadvantages in total generator weight and efficiency, even the translator weight and PM weight yields lowest values. Furthermore, by comparing the case that PM thickness is 60 mm to the case that PM thickness is 70 mm, it is found that the total weight is almost the same, but the PM weight is about 9% off. In the viewpoint of reducing costs, the PM thickness is desirable to be 60 mm.

In the case that PM thickness is 60 mm, the generator efficiency is about 81%. The weight is about 51 tons. The length of stator part is 11.5 m, which is 3.7 m longer than the translator to save PMs. Resistance loss of armature windings occupies around 85% of the total loss, which validates that the proposed structure of the PM-TLG (with armature windings inside) contributes to the reduction of total loss.

Table 3-3 Design results of 1 MW PM-TLGs.

Item	Value		
PM thickness (mm)	50	60	70
Maximum electrical frequency (Hz)	3.15	3.15	3.15
Total air gap length(mm)	12	12	12
Number of PM poles	42	42	42
Pole pitch (mm)	184	184	184
Electric loading (A/cm)	1000	1000	1000
Current density of conductors (A/mm^2)	3	3	3
Armature leakage coefficient	1.26	1.31	1.35
Air gap leakage coefficient	1.09	1.12	1.13
PM width/pole pitch	0.73	0.73	0.73
PM flux density (T)	0.50	0.59	0.65
Air gap flux density (T)	0.46	0.53	0.58
Effective stator teeth flux density (T)	1.41	1.65	1.80
Outer diameter of translator (m)	1.4	1.3	1.2
Length of PM part (m)	7.8	7.8	7.8
Length of armature part (m)	11.5	11.5	11.5
No-load MMF (kA/pole)	28.3	36.9	45.1
Load MMF (kA/pole)	44.7	53.7	62.6
Generator weight (ton)	54.5	51.3	50.5
Stator weight (ton)	34.3	30.5	28.5
Copper winding weight (ton)	11.9	10.3	9.5
Iron core weight (ton)	13.6	12.7	12.1
Support, Others (ton)	8.8	7.5	6.9
Translator weight (ton)	20.2	20.8	22
PM weight (ton)	7.8	8.3	9.1
Iron yoke (ton)	5.2	5.4	5.5
Support, Others (ton)	7.2	7.1	7.4
Total loss (kW)	266	231	214
Resistance loss of armature windings (kW)	232	200	184
Iron loss (kW)	4	5	6
Others* (kW)	30	26	24
Efficiency (%)	79.0	81.2	82.4

*Others include stray loss, mechanical loss, and blower power for air cooling.

3.3.2 Analysis of magnetic flux

For the PM-TLG with PM thickness of 60 mm, under no-load condition, the magnetic flux density distribution in different radial positions with respect to axial direction is shown in Fig. 3-12 to Fig. 3-14, including the design values. Fig. 3-12 presents the magnetic flux density distribution in PM center (marked as r_p in Fig. 3-9) along the axial direction. It is observed that for both teeth center case and slot center case, the average value of B_p with the length of field pole in r_p is almost same, which is 0.91 T. And the design value under no-load condition is 0.90 T, almost the same with the simulation result.

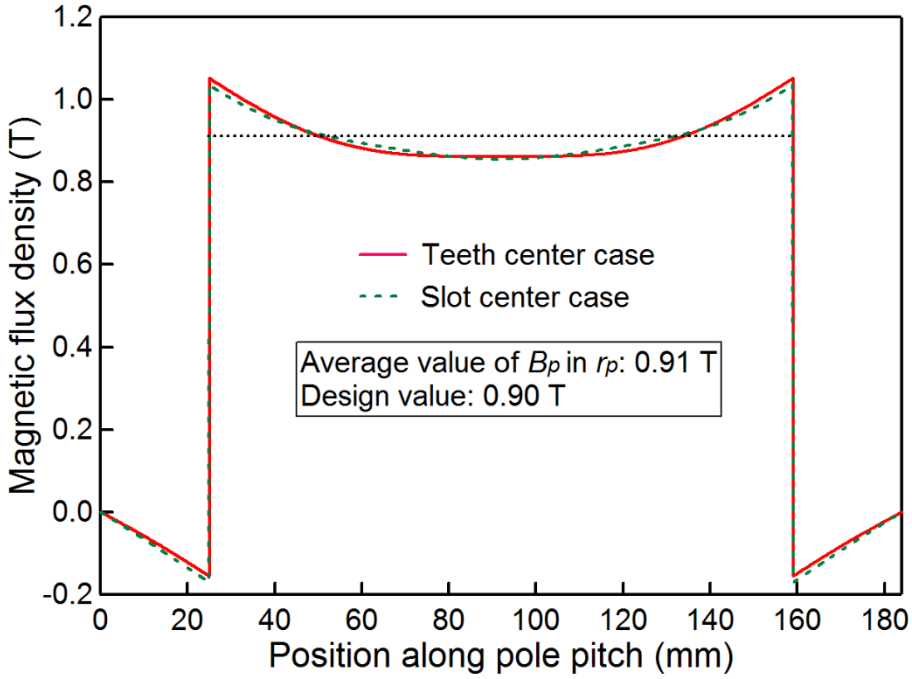

Fig. 3-12 Distribution of B_p in r_p along axial direction.

The magnetic flux density distribution in air gap center (marked as r_g in Fig. 3-9) is displayed in Fig. 3-13. For both teeth center case and slot center case, the B_g distribution in r_g are symmetrical to the center of the pole, and exhibit the slot-tooth distribution corresponding to the stator structure. The mean value of magnetic flux density with the effective length of the field pole is 0.76 T for the teeth center case, and 0.74 T for the slot center case. And the average B_g of these two cases is 0.75 T, which is almost same with the design value of 0.74 T.

Fig. 3-14 presents the distribution of B_t in r_t (as shown in Fig. 3-9), where is about 1/3 position of the stator teeth and close to the stator core. It is worth noting that the magnetic flux density in different radial positions of teeth part is related to diameter of the position, and the magnetic flux density in r_t is treated as the average value of stator teeth part. The B_t

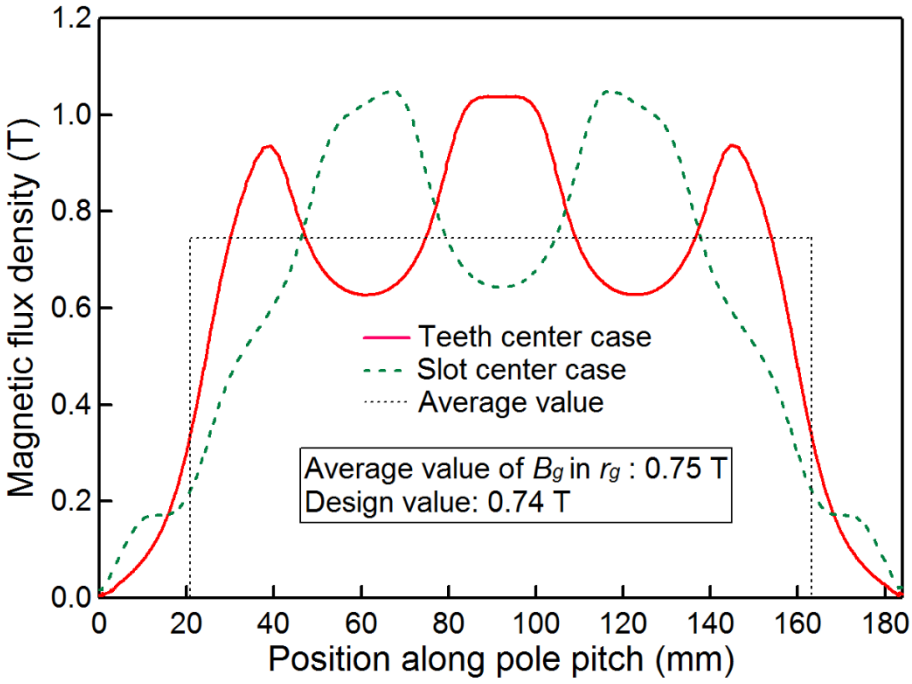

Fig. 3-13 Distribution of B_g in r_g along axial direction.

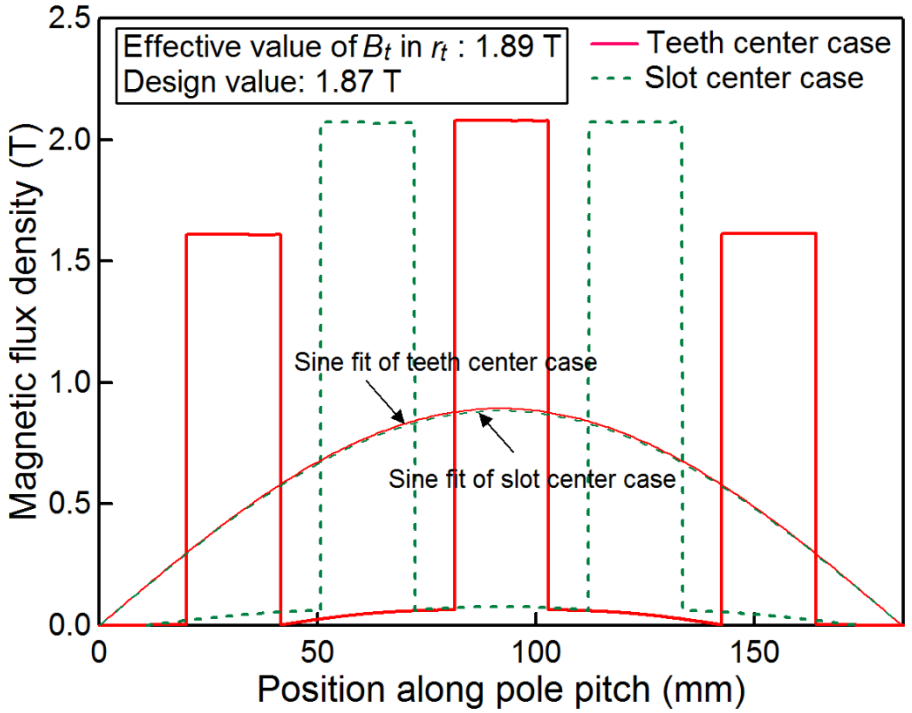

Fig. 3-14 Distribution of B_t in r_t along axial direction.

in r_t yields good agreement with the structural slot-tooth distribution for both teeth center case and slot center case. Furthermore, it is found that the maximum values of fundamental waves are 0.89 T for teeth center case, and 0.88 T for slot center case, respectively. The average effective value of the fundamental waves for these two cases is $[(0.88+0.84)/2]/\sqrt{2}$

= 0.63 T, and it is calculated that the average effective magnetic flux density in stator teeth is 0.63 × 61.3 (slot pitch) / 21.5 (teeth width) =1.80 T. Considering the 5% insulators of teeth part, we treat the average effective magnetic flux density in stator teeth as 1.80/0.95 = 1.89 T, which is a little higher than the design value of 1.87 T.

As illustrated above, the design values of the magnetic flux density in different parts are in pretty good agreement with the calculated ones. Therefore, it is demonstrated that the design results are adequate.

3.4 Conclusion

In this chapter, a 1 MW tubular PM-TLG is designed for a WEC based on ocean wave parameters, in which the PM-TLG is directly driven by a cylindrical heaving buoy. The main conclusions are listed as follows:

(1) Conceptual structure of the WEC is proposed, which features a cylindrical buoy and a tubular PM-TLG. Translator of the PM-TLG is designed shorter than the stator to save PMs, and the PMs are located outside of the stator, which benefits for increasing the magnetic flux of field PMs and reducing the resistance loss of armature windings.

(2) Electrical design method of the PM-TLG is developed and described in detail, especially the approach of determining main machine parameters, the way of calculating leakage coefficients, and the easy and accurate method of evaluating PM operating point.

(3) Optimum design results of PM-TLGs with different PM thicknesses (50 mm, 60 mm, and 70 mm) are presented, and it is demonstrated that the generator with PM thickness of 60 mm exhibits the best trade-offs between generator performance and cost.

(4) For the PM-TLG with PM thickness of 60 mm, the magnetic flux density distribution is analyzed. The good agreements of simulation results with design values verified the accuracy of the design results.

Chapter IV Electrical design study of HTS-TLGs for WECs

PM linear generators are becoming popular in direct-drive WEC systems [98][99], however, PM generators with PMs located in the translator suffer from the possibility of PM demagnetization by armature reaction field. Even the movement of PMs can be avoided by changing the structure [100], these machines still has the drawbacks of high PM cost and uncontrollable airgap flux due to the PM excitation. Fortunately, the exceptional high current density in the superconductors makes it possible to significantly improve the power density of machines. Especially, the discovery of HTS materials results in the great advancement of superconductor coils which can be practically applied to electric machines based on the relatively less stringent refrigeration system [101]. Compared with conventional machines, the HTS machines have the distinct advantages of higher power density, higher torque density, higher efficiency and low life cycle cost [102].

This chapter aims to present the key electrical design technologies of a 1 MW HTS-TLG for the WEC presented in Chapter II. Conceptual structure of the HTS-TLG is firstly described. Then, the developed electrical design method is described in detail, including the design process, the determination of main machine parameters, the calculation of MMF, and the methods of obtaining leakage coefficients and HTS heat loss by using 3-D simulation. Furthermore, the motion of translator part is analyzed, and the induced voltage waveforms are plotted to demonstrate the feasibility of using this device to obtain desirable output power. And an economical way of connecting the output power to grid is proposed. Moreover, the cooling system is proposed and designed. The various heat losses are calculated and the input power of cryocooler is evaluated.

4.1 Conceptual structure of HTS-TLGs

Conceptual structure of the WEC device is displayed in Fig. 4-1 (a). There are four main components: the base, the support, the HTS-TLG, and the buoy. The base is fixed to seabed. The support connecting to stator of the HTS-TLG is attached to the base. Translator of the HTS-TLG is coupled with the reciprocating buoy, and is connected to seabed via a spring. The spring retracts the translator in the wave troughs, preventing the translator from moving out of the stator in the cases that waves are much higher than the assumed one (wave height of 4 m, as shown in Table I). The cylindrical buoy is chosen because significant output power can be obtained, and the output power can be increased by simply enlarging the buoy.

Fig. 4-1 (b) depicts the cross section of the HTS-TLG. The inside translator is composed of field iron yoke, field iron poles, HTS field windings, and cryogenic vessels. It is worth noting that each HTS coil has its own cryogenic vessel, and the HTS coils are connected in three sections in parallel through the iron pole pieces by using adiabatic tubes. Considering the electromagnetic forces on the HTS coils, cryogenic vessels are designed to fix the HTS coils, which will be presented in Chapter V. Besides, a refrigerator is set inside of the heaving buoy, in which way, positions of the adiabatic tubes and the cryostats are relatively stationary despite the moving HTS field part. Exciting power of the refrigerator is supplied by the rectified output power of the HTS-LG, which could be stored in a battery. Both the battery and power supplies of the HTS coils are also put inside of the buoy. Stator of the HTS-TLG consists of three-phase armature copper windings and iron back cores. Slot number/pole/phase is decided as 1 for easy assembly consideration. The armature phase coils are connected in 2 separate sections in parallel, and the phase coils in each section are connected in series. During operation, adjacent ring-shaped HTS coils are excited by DC currents with same amplitude but opposite direction to generate alternating magnetic poles as indicated in Fig. 1(b). On the other hand, the translator is forced up and down by the heaving buoy. Consequently, the alternating magnetic poles move past the armature coils, and voltage is induced.

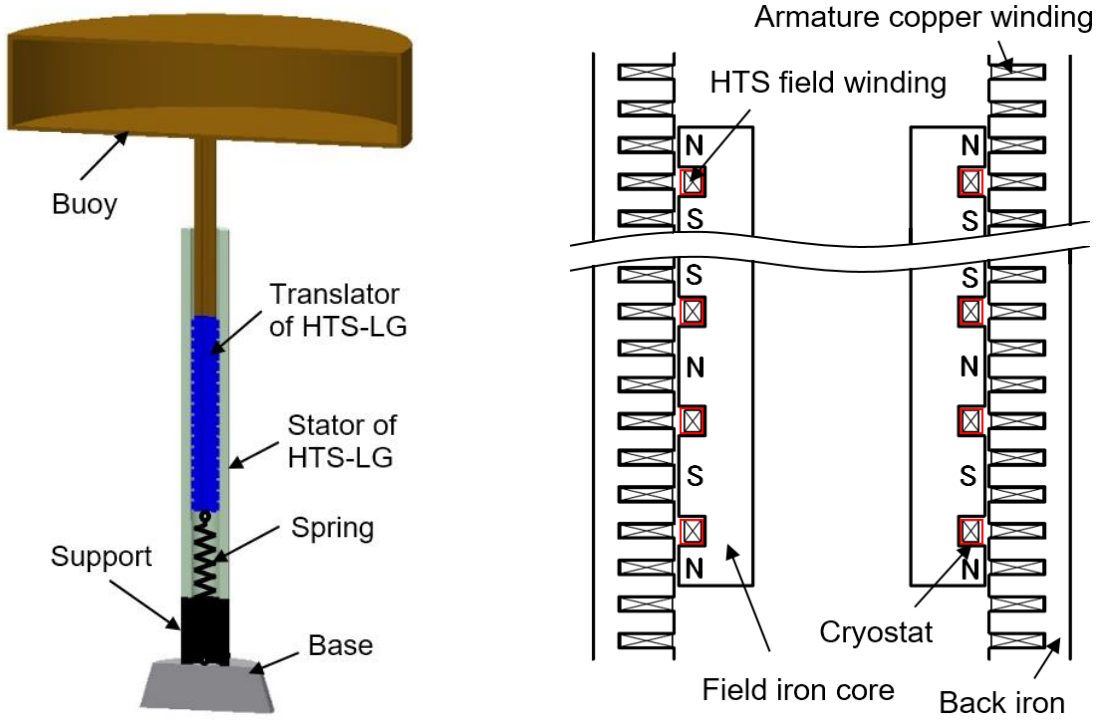

(a) (b)

Fig. 4-1 (a) Conceptual structure of the WEC device. (b) Cross-sectional view of the HTS-TLG.

About the connection of HTS coils, robustness of the HTS-LG would be greatly increased if HTS coils were connected in parallel. However, if all the coils are connected in parallel, the exciting current would be very large; on the other hand, it may lead to induced circulating AC currents. The HTS-LG designed in this paper has 18 HTS coils in total. These coils are connected in 3 separate sections in parallel and use 6 leads with three separate power supplies. With the 18 HTS coils, 18 (17+1/2 × 2) equivalent field poles are formed by adopting half iron poles in both ends of the translator, as shown in Fig. 4-1(b).

Features of the HTS-TLG are described as follows.

- The tubular HTS-TLG is characterized no coil ends for both HTS windings and copper windings, thereby reducing the amount of HTS and copper wires, leakage flux and conduction loss.
- The tubular HTS-LG is adopted in consideration of the little attractive forces between the stator and the translator, which reduces the bearing load. Besides, the tubular structure makes it easy to support HTS coils and copper coils, which are placed around iron poles and stator teeth.
- The tubular HTS-LG has ring-shaped coils in both the HTS field windings and copper windings. These coils do not require the end windings needed for conventional generator coils that span several slots in the iron core, thereby reducing the amount of HTS and copper wires, leakage flux, and per-unit armature resistance and inductance.
- The HTS field part is chosen as the translator considering its light weight, which benefits for reducing mechanical tensions on the heaving buoy, thus reducing maintenance.
- The translator is designed shorter than the stator part for the sake of saving expensive HTS wires, thus reducing cost.
- Each HTS coil has its own cryostat instead of putting the whole field within one cryostat, which benefits for reducing cooling time and making maintenance and repair easier in failure of the HTS windings.

4.2 Electrical design method of HTS-TLGs

To design a HTS-TLG, there are a lot of variable parameters should be taken into account at the same time, such as number of poles, pole pitch, leakage coefficient, teeth width/slot width, magnetic flux density in the armature teeth, HTS operating current, and so on. Therefore, it is very difficult to design a HTS-TLG in the conventional ways. To make the design easier and more flexible, we developed a computer program. Novelty of the program is that electrical design of HTS-TLGs is carried out automatically based on the input calculation equations of machine parameters. The program presents the generator

performance in terms of generator weight, efficiency, cost, and so on, corresponding to the geometric parameters, which makes it easy to obtain accurate machine parameters considering the basic generator performance. Moreover, 3-D simulation is conducted to calculate leakage coefficients and HTS heat loss, which are feedback to the design program to adjust machine geometric parameters. The design process and key design technologies including the determination of main machine parameters, the calculation of MMF and the approaches of obtaining leakage coefficients and HTS heat loss, are presented in detail as follows.

4.2.1 Design process

Fig. 4-2 shows the electrical design flowchart of HTS-TLGs. Basic specifications of HTS-TLGs are given in step 1, which are listed in Table 4-1. Here, it is worth mentioning that we decided the maximum output power of HTS-TLGs as 1 MW taking into account the losses that must be supplied by the buoy, converter efficiency and generator efficiency. Machine parameters of armature and translator part are calculated in step 2-5. The magnetomotive force (MMF) under load condition is derived in step 6. Then, 3-D simulation is conducted to analyze magnetic field in step 7. By using the simulation results, HTS field leakage coefficient and heat loss are obtained, which are feedback to the program to get adequate machine parameters. The generator performance is finally obtained in step 8. The realization of every step is illustrated in detail as follows.

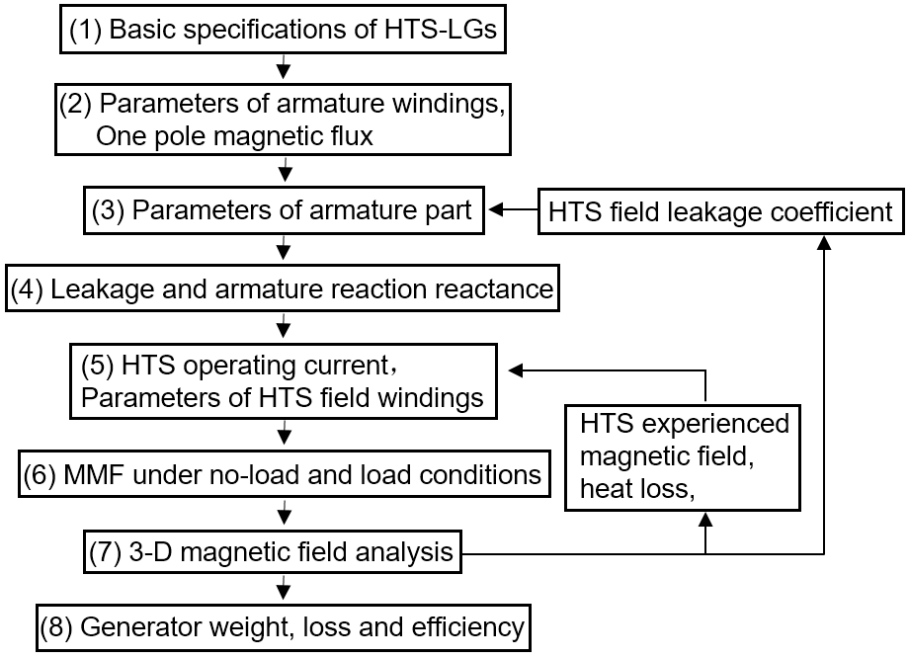

Fig. 4-2 Electrical design flowchart of HTS-TLGs.

Table 4-1 Basic specifications of a 1 MW HTS-TLG.

Item	Value
Wave height (m)	4
Wave frequency (Hz)	0.1
Terminal voltage (V)	660
Line current (A)	875
Air gap length (mm)	12
Slot number / pole / phase	1
Electric loading (A/cm)	1000
Field pole width/pole pitch	0.73
Current density of armature conductors (A/mm^2)	3
Magnetic flux density in armature core back (T)	1.6
Magnetic flux density in field iron yoke (T)	2.0

Step 1— Basic specifications of HTS-TLGs

Basic specifications of 1 MW HTS-TLGs are listed in Table 4-1. The wave is assumed as 4 m in height and 0.1 Hz in frequency as mentioned in Chapter II. Besides, as the generator is long, air gap length of 12 mm should be necessary to prevent the contact of stator and translator, which consists of 8 mm mechanical clearance and 2 mm sealing sheets in both the outer surface of field poles and the inner surface of armature teeth. And there are several linear bearings mounted between the stator and the translator to keep them aligned properly. Moreover, it is worth mentioning that we decided the maximum output power of HTS-LGs as 1 MW taking into account the losses that must be supplied by the buoy, converter efficiency and generator efficiency.

Step 2—Parameters of armature windings and required magnetic flux per pole

- Slot pitch is decided with a given pole pitch and slot number/pole/phase N_{pp}. Then, the number of armature conductors/slot connected in series q is calculated with a selected electric loading and armature conductor current, which is determined by line current and parallel number of armature conductors a.
- Cross-sectional area of armature conductors is further calculated by using a selected armature conductor current density, and then slot dimension is determined.
- Furthermore, the required maximum magnetic flux per pole in armature part Φ provided by HTS coils is calculated, which is relative to the terminal voltage, the maximum electrical frequency, and the effective number of armature conductors connected in series n_e. Here, $n_e = q \cdot P_f \cdot N_{pp} / a$, where, P_f is the number of field poles.

Step 3—Parameters of armature part

- With an assumed field leakage coefficient σ, we deduce the diameter of field pole center, which is $D_f = \sigma\Phi / (\pi \cdot l_f \cdot B_f)$. Here, l_f is the field pole width, and B_f is the flux density in the field poles, which is initially assumed. Diameter of air gap center is further decided.

- With the determined slot depth, inner diameter of armature back iron D_i is further decided. Moreover, height of armature back iron h is deduced by $\Phi/2 = \pi \cdot (Di+h) \cdot h \cdot B_c$, where, B_c is the flux density in the back iron. Then, outer diameter of the armature back iron is determined.
- With the determined dimension of armature teeth, the magnetic flux density in teeth part can be calculated.
- The length of armature winding/turn is calculated by using the decided diameters of armature part, and the resistance of armature windings is further obtained.

Step 4—Leakage and armature reaction reactance

Based on the terminal voltage, line current, electrical frequency, and some armature parameters, the armature leakage coefficient is deduced. The armature leakage reactance and reaction reactance are further obtained.

Step 5—Parameters of HTS field windings

Exciting current of HTS windings is dependent on the heat loss generated by HTS coils. Then, number of turns of HTS windings is decided considering the approximate *MMF* under load condition. Furthermore, total length of HTS wires is calculated.

Step 6—MMF under no-load and load conditions

- The required MMF of armature teeth, back iron, field pole, and iron yoke is calculated by using the iron steel *B-H* characteristics, respectively. The MMF under no-load condition is the sum of the above values and the MMF of air gap.
- MMF under load condition is calculated considering the MMF under no-load condition, and the MMF of the armature reaction and leakage reactance.

Step 7—3-D magnetic field analysis

A 3-D model of the HTS-TLG is established by using MagNet7.4.1 (Infolytica Inc.). To get accurate design results, two pivotal machine parameters are calculated based on the simulation results. Firstly, the accurate value of HTS field leakage coefficient is obtained, which is feedback to Step 3, modifying the geometric and electromagnetic parameters of the HTS-TLG. Moreover, HTS heat loss is derived based on the simulation results, which is feedback to Step 5, determining the operating current of HTS coils. It is worth noting that the HTS operating current affects the number of turns of HTS coils used in the HTS-TLG, changing the cross-section area of HTS coils. Correspondingly, the height of HTS coils together with the height of field poles are adjusted.

Step 8—Generator weight, loss and efficiency

After every machine parameter is determined, the weight of the HTS-TLG is calculated. Different kinds of loss are evaluated, and the total loss and efficiency of the HTS-TLG are obtained.

Main features of this electrical design method are described here.

- The electrical design is carried out automatically, and main machine parameters are determined by studying their influence on basic generator performance.
- The design process contains two feedback loops, in which the leakage coefficient and HTS exciting current are obtained by simulation to make the design results adequate.

4.2.2 Calculation of magnetomotive force (MMF)

The MMF under both no-load and load conditions is calculated by using the similar conventional ways. Phasor diagram of HTS-TLGs is displayed in Fig. 4-3 to obtain the MMF, and the symbols in the phasor diagram are defined as

E_0 —— Induced voltage under no-load condition

E_i —— Internal voltage V_t —— Terminal voltage

I_a —— Line current θ —— Power-factor angle

R_a —— Resistance of armature windings

X_a —— Armature reaction reactance

X_q —— Quadrature-axis armature reaction reactance

X_l —— Leakage reactance δ —— Load angle

AT_i —— MMF inducing internal voltage *Ei*

AT_a —— MMF compensating for armature reaction

AT_0, AT_2 —— MMF under no-load and load condition

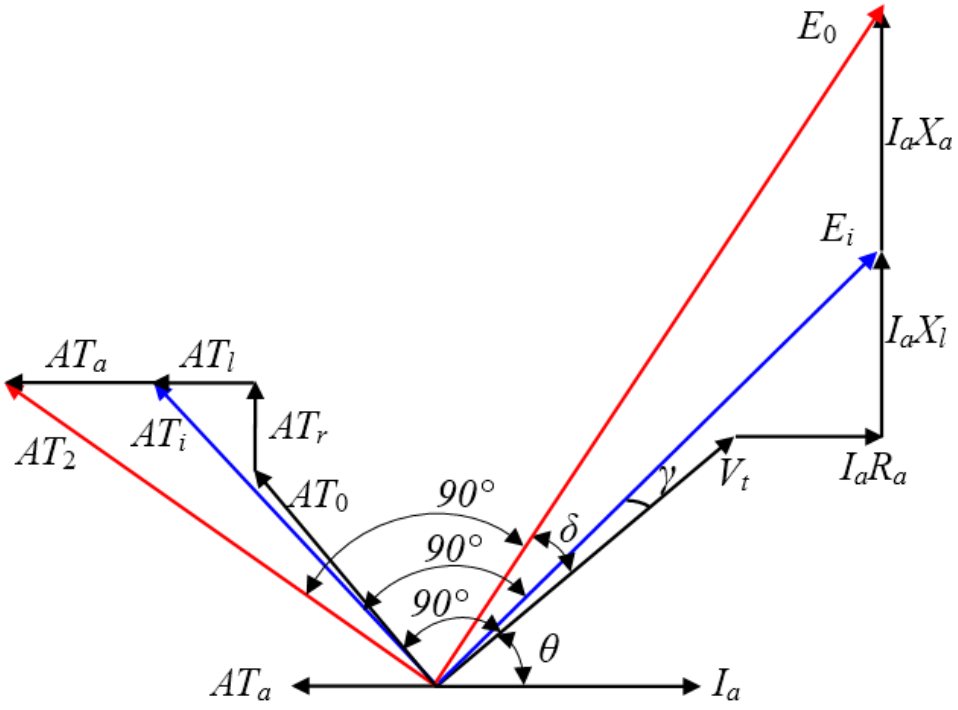

Fig. 4-3 Phasor diagram of HTS-TLGs.

Referring to Fig. 4-3, the MMF corresponding to the internal voltage is expressed as

$$\begin{aligned} AT_i &= AT_0 \times \frac{E_i}{V_t} \\ &= AT_0 \times \frac{\sqrt{(V_t \cos\theta + I_a R_a)^2 + (V_t \sin\theta + I_a X_l)^2}}{V_t} \\ &= AT_0 \times \sqrt{(r_a + \cos\theta)^2 + (x_l + \sin\theta)^2} \end{aligned} \tag{4-1}$$

where

$$r_a = I_a R_a / V_t \ , \quad x_l = I_a X_l / V_t \ .$$

On the other hand, the MMF corresponding to the armature reaction flux is shown as

$$AT_a = 1.35 \times \frac{K_w \cdot n_e}{P_f} \cdot I_a \times \sqrt{\frac{K_{dm}^2 (\sin\theta + x_l + x_q)^2 + K_{qm}^2 (\cos\theta + r_a)^2}{(\sin\theta + x_l + x_q)^2 + (\cos\theta + r_a)^2}} \tag{4-2}$$

where K_w is the winding factor. n_e is the series number of effective armature conductors per phase, where, effective armature conductors mean the conductors which are overlapped with the field part in position. P_f is number of field poles. x_q is the quadrature-axis armature reaction reactance in per unit, expressed as $x_q = I_a X_q \ / \ V_t$. K_{dm} and K_{qm} are direct-axis and quadrature-axis magnetic flux reduction factor caused by armature reaction, respectively, which are expressed as

$$K_{dm} = \frac{\alpha\pi + \sin(\alpha\pi)}{4\sin(\frac{\alpha\pi}{2})} \ , \quad K_{qm} = \frac{\alpha\pi - \sin(\alpha\pi) + \frac{2}{3}\cos(\frac{\alpha\pi}{2})}{4\sin(\frac{\alpha\pi}{2})}$$

where α is the field pole width/pole pitch. Here, field pole width means the length of field iron pole along the generator axial direction.

Then, the MMF under load condition is expressed as

$$\begin{aligned} AT_2 &= \sqrt{AT_i^2 + AT_a{}^2 + 2AT_i AT_a \sin(\theta + \gamma)} \\ &= \sqrt{AT_i^2 + AT_a{}^2 + 2AT_0 AT_a (x_l + \sin\theta)} \ . \end{aligned} \tag{4-3}$$

4.2.3 Parameter survey

Based on the developed electrical design method, main machine parameters are firstly determined by studying their influences on the basic generator performance. Here, the basic generator performance is presented in terms of weight of HTS-TLGs, HTS length, and efficiency of HTS-TLGs, which are considered because 1) heavy machines increase the difficulty in construction, transportation and installation, as well as high costs; 2) HTS tapes are expensive, and shorter HTSs mean lower costs; 3) generator efficiency should be as high

as possible to make full use of wave energy. The main machine parameters, such as the number of poles, pole pitch, magnetic flux density in field iron pole, magnetic flux density in armature teeth, and HTS operating temperature play significant roles in determining the geometric and electromagnetic characteristics of HTS-TLGs, thus affecting the basic generator performance. Selection of these parameters is illustrated in detail as follows.

A. Influence of generator length on performance of HTS-TLGs

Long generators have the difficulty to keep air gap uniform, but benefit for reducing generator weight. Fig. 4-4 exhibits the generator weight, the total HTS length, and the generator efficiency derived from the design results as a function of generator length. Here, the generator length is the length of outer armature part of HTS-TLGs. We observed that with the increase of generator length, the generator weight decreases then increases, which is explained as follows. For TLGs, the output power $P \propto D \cdot L$, and the weight $W \propto D^2 \cdot L$ ($\propto 1/L$ at constant P), therefore, the generator weight decreases with the increasing generator length. However, limited by the inner diameter of the HTS-TLG, the diameter of the HTS-TLG cannot be decreased to a required value when the generator is longer than 12.4 m. Therefore, increasing generator length at a constant minimum diameter causes increasing generator weight. It is further noted that the HTS length increases with the increasing generator length. Additionally, the efficiency decreases with the increasing generator length, which is caused by the increasing resistance loss of armature windings and the increasing input power of cryocooler for more HTS coils.

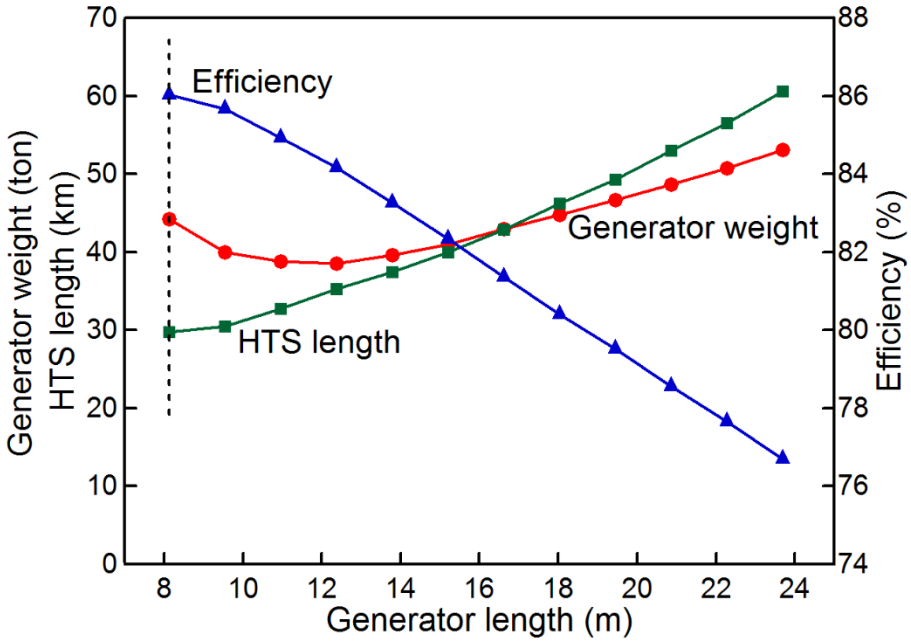

Fig. 4-4 Variation of HTS generator weight, HTS length, and generator efficiency with respect to length of the HTS-TLG.

The generator length is decided as about 8 m (with HTS field part about 4 m, containing 18 HTS coils) considering the mechanical stability of WECs in off-shore application, even the generator is not lightest in this case. However, the HTS tapes are shortest (29.8 km), and the generator efficiency is highest (86.0%), which makes this selection promising for large-scale WEC application.

B. Influence of pole pitch on performance of HTS-TLGs

Pole pitch directly determines the electrical frequency of HTS-TLGs. Smaller pole pitch leads to higher electrical frequency, but on the other hand results in less number of effective armature conductors. The required magnetic flux per pole is inversely proportional to the product of these two parameters with the given terminal voltage, and determines the design results of HTS-TLGs.

Fig. 4-5 shows the variation of generator weight, HTS length, and generator efficiency with respect to pole pitch of HTS-TLGs, and the required magnetic flux per pole under each pole pitch is also given. It is noted that under each pole pitch, the generator length keeps about 8 m. From Fig. 4-5, we observed that with the increasing pole pitch 1) the generator weight decreases then increases; 2) the generator efficiency increases then decreases; 3) and the HTS length keeps decreasing. Besides, it is worth mentioning that both the generator weight and the efficiency changes quickly when the pole pitch is beyond 236 mm, resulted from the sharply increased magnetic flux per pole. The pole pitch is decided as 236 mm considering the relatively light machine, short HTS wires, and high generator efficiency.

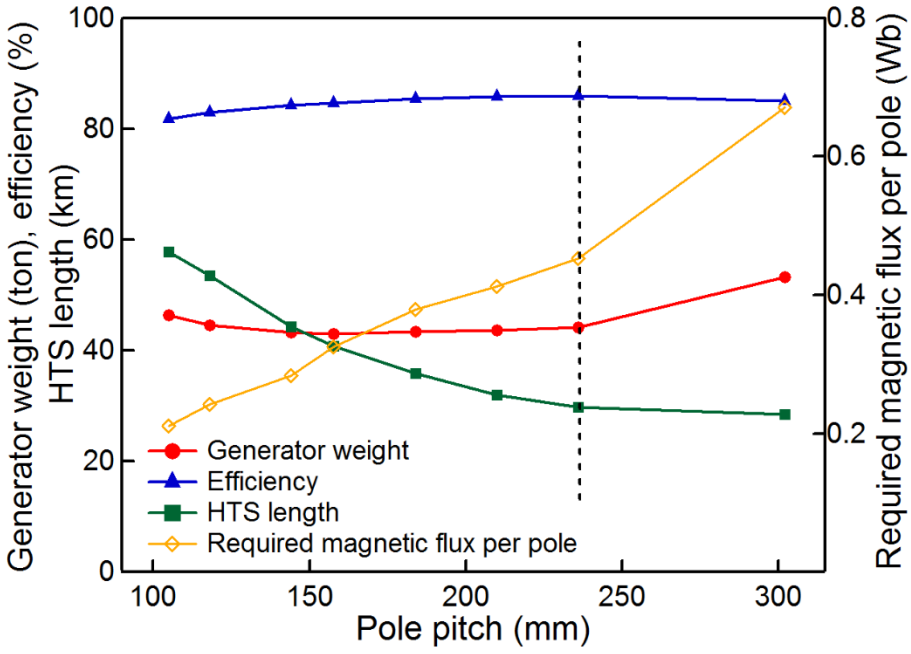

Fig. 4-5 Variation of generator weight, HTS length, and generator efficiency with respect to pole pitch of HTS-TLGs (generator length about 8 m).

C. Influence of magnetic flux density in field iron pole on performance of HTS-TLGs

Magnetic flux density in field iron pole B_f directly determines the diameter of field pole center $D_f = \sigma\Phi / (\pi \cdot l_f \cdot B_f)$, as discussed in Section 4.2.1, thus affecting the diameter of the generator. Fig. 4-6 exhibits the influence of B_f on generator weight, HTS length, and generator efficiency. It is noted that the results are obtained under the constant generator length of 8.1 m and pole pitch of 236 mm. We observed that with the increase of B_f, generator weight decreases, resulted from the decreasing generator diameter; besides, generator efficiency increases, caused by the decreasing length of armature windings due to the decreasing diameter of armature part; moreover, HTS length decreases then increases when the B_f is beyond 1.84 T, which is the result of the decreasing diameter of field part and the increasing number of turns of HTS coils. Here, the number of turns of HTS coils increases with the increasing B_f because that the load MMF increases, caused by the increasing magnetic flux density in air gap, armature teeth, field pole, and iron yoke. The B_f is decided as 1.89 T considering the trade-offs among the generator weight, efficiency, and HTS length.

D. Influence of magnetic flux density in armature teeth on performance of HTS-TLGs

As a matter of fact, the magnetic flux density in armature teeth B_t is varied by changing the diameter of field pole center D_f under the constant generator length and pole pitch. Therefore, the influence of B_t on the basic generator performance follows the tread of the influence of B_f, as seen from Fig. 4-7. The B_t is decided as 2.06 T considering the relatively light generator weight, high efficiency, and short HTS wires.

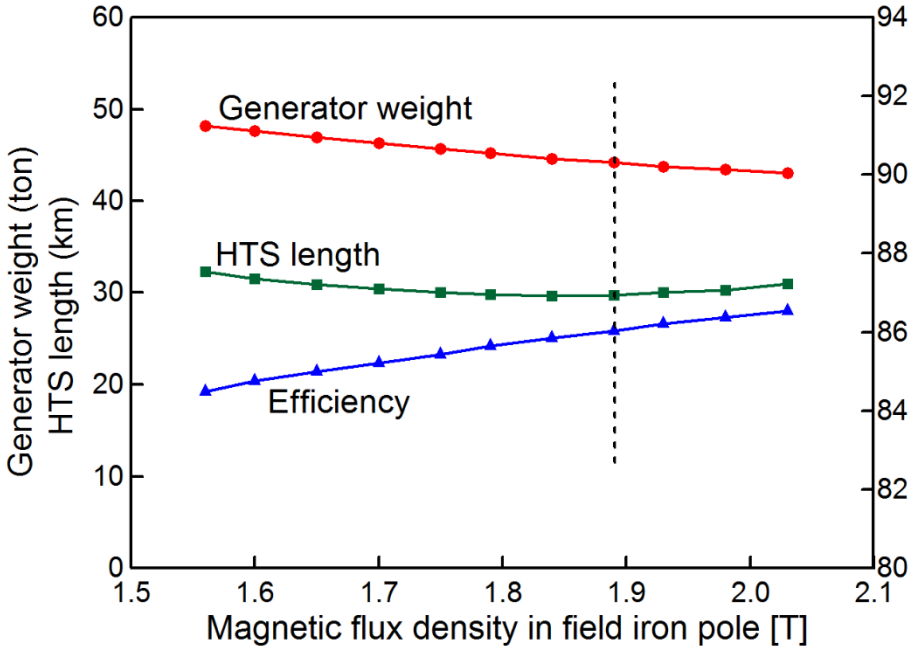

Fig. 4-6 Variation of generator weight, HTS length, and generator efficiency with respect to B_f of HTS-TLGs.

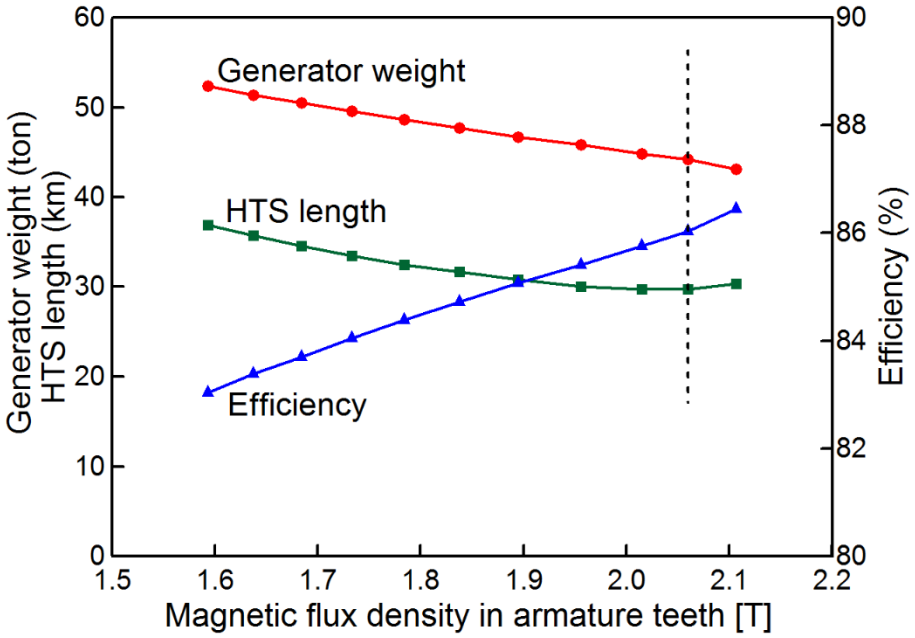

Fig. 4-7 Variation of generator weight, HTS length, and generator efficiency with respect to B_t of HTS-TLGs.

E. Influence of HTS operating temperature on performance of HTS-TLGs

HTS operating temperature determines the critical current density of HTSs and influences the input power of cryocooler of HTS-TLGs, which is dependent on the temperature difference between the operating temperature and the surrounding temperature. To study the influence of HTS operating temperature on the basic generator performance, we firstly calculated the required input power to cryocooler of the 1 MW HTS-TLG under different operating temperatures, as shown in Fig. 4-8, which reveals that the input power of cryocooler decreases with the increase of operating temperature.

Furthermore, we studied the basic generator performance under different operating temperatures, which is shown in Fig. 4-9. It is found that the operating temperature has a little influence on the generator weight. It is also observed that with the increase of operating temperature, the HTS length increases, which is caused by the decreasing critical current density. And the efficiency increases because of the decreasing required input power of cryocooler, as shown in Fig. 4-8. Considering the stringent limits upon the volume of the cooling systems in off-shore application, we decided the operating temperature as 77 K due to the low required input power of cryocooler about 8 kW.

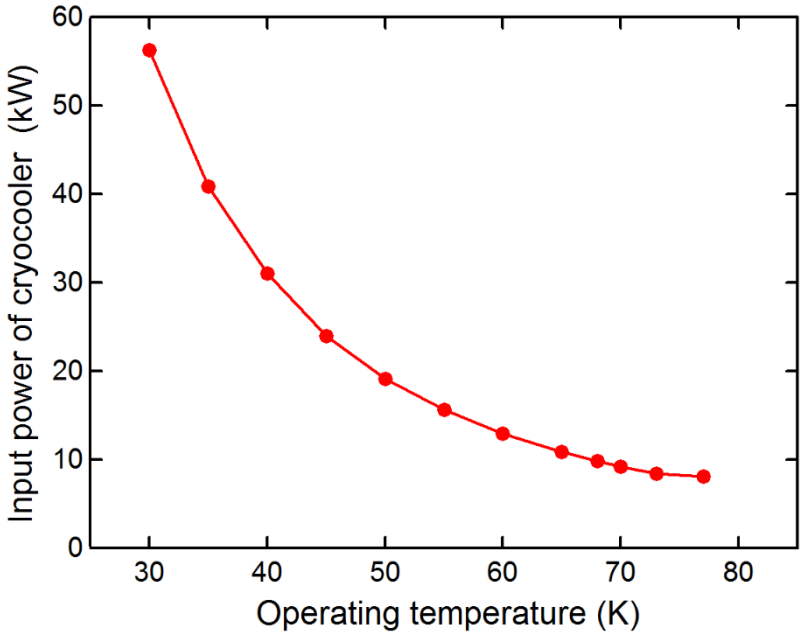

Fig. 4-8 The input power of cryocooler as a function of operating temperature.

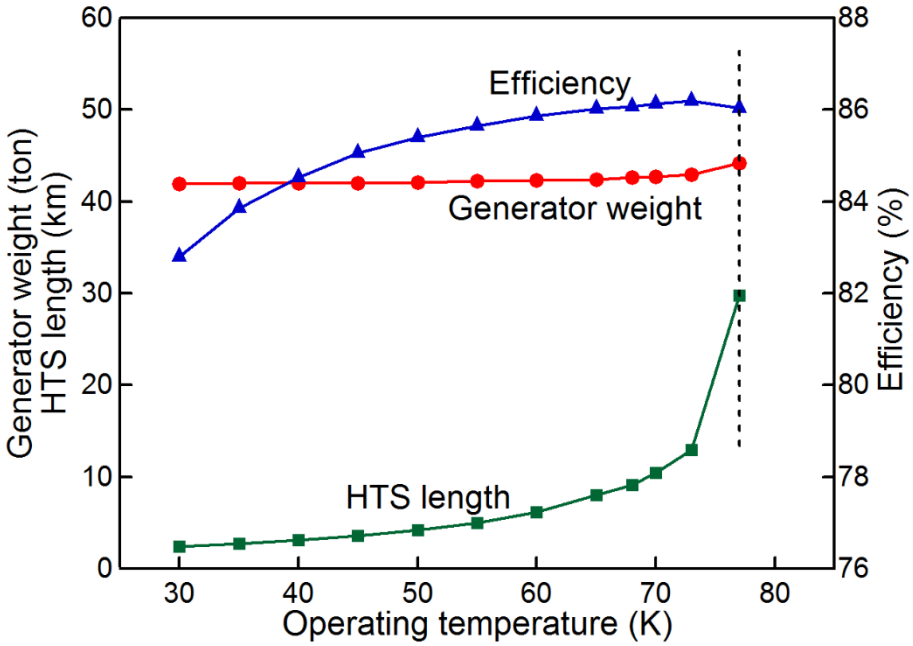

Fig. 4-9 Variation of HTS generator weight, HTS length, and generator efficiency with respect to operating temperature.

The influence of other main machine parameters such as electric loading, field pole width/pole pitch, and current density of armature conductors on the basic generator performance has also been studied. And the determination of the main machine parameters of the HTS-TLG is summarized in Table 4-2.

Table 4-2 Determination of main machine parameters of a 1 MW HTS-TLG.

Item	Value
Operating temperature (K)	77
Number of field poles	18
Number of armature poles	34
Pole pitch (mm)	236
Magnetic flux density in field iron pole B_f [T]	1.9
Magnetic flux density in armature teeth B_t [T]	2.1
Electric loading (A/cm)	1000
Field pole width/pole pitch	0.73
Current density of armature conductors (A/mm^2)	3

4.2.4 3-D simulation

A 3-D quarter model of the 1 MW HTS-TLG is shown in Fig. 4-10. Using this model, leakage coefficients and HTS heat loss are calculated to make design results more accurate. The methods of obtaining leakage coefficients and HTS heat loss with 3-D simulation are illustrated in detail as follows.

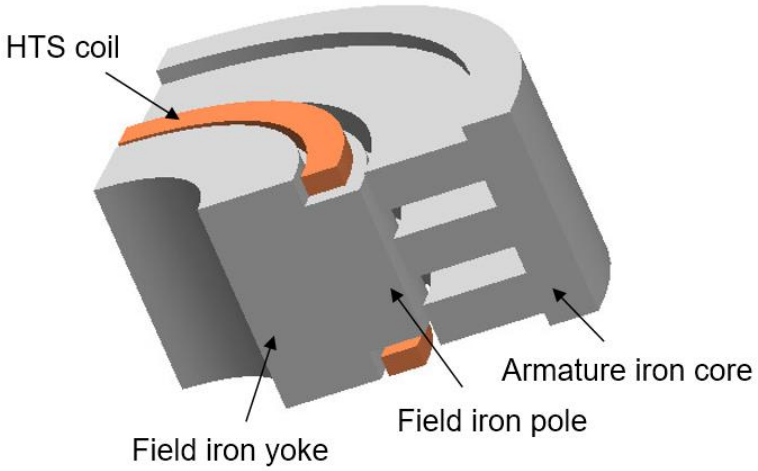

Fig. 4-10 3-D quarter model of the one-pole HTS-TLG without armature windings.

A. Calculation of HTS field leakage coefficient

In consideration of the large air gap of the HTS-TLG, two kinds of leakage coefficients are defined, which can make the design results more accurate. They are field leakage coefficient σ defined as the ratio of average interlinkage magnetic flux on field HTS part Φ_{ff} to that on armature winding part Φ_{af}, namely $\sigma = \Phi_{ff}/\Phi_{af}$, and air gap leakage coefficient σ_g defined as the ratio of average interlinkage magnetic flux on field HTS part Φ_{ff} to that in the airgap Φ_{gf}, namely $\sigma_g = \Phi_{ff}/\Phi_{gf}$.

The flowchart of calculation on these two leakage coefficients are shown in Fig. 4-11. The initial assumed values of σ and σ_g are 1.3 and 1.1, respectively. Based on these values,

generator parameters are preliminarily decided. Two models are established to calculate the leakage coefficients under two cases, as shown in Fig. 4-12 (a) ("teeth center case") and Fig. 4-12 (b) ("slot center case"). New values of the σ and the σ_g are obtained for the "teeth center case" (σ_{t1}, σ_{gt1}) and the "slot center case" (σ_{s1}, σ_{gs1}) by simulation, respectively. The average values $\sigma_1 = (\sigma_{t1}+\sigma_{s1})/2$ and $\sigma_{g1} = (\sigma_{gt1}+\sigma_{gs1})/2$ are feedback to decide machine parameters again. The process mentioned above is repeated till the difference between the calculated values σ_n, σ_{gn} and the feedback values σ_{n-1}, $\sigma_{g(n-1)}$ obtained from the previous step is less than an allowable value, namely, $|(\sigma_n-\sigma_{n-1})/\sigma_n| < 0.01$, and $|(\sigma_{gn}-\sigma_{g(n-1)})/\sigma_{gn}| < 0.01$. Then, the σ_n and σ_{gn} are obtained as the final design values to make the machine parameters adequate. For the 1 MW HTS-TLG, the σ_n and σ_{gn} are calculated as 1.24 and 1.07, respectively.

The HTS excitation current is varied during operation to keep the generator output voltage constant under varying loads and wave heights. It should be noted that the simulation of calculating leakage coefficients is conducted under no-load condition, and the input current is 46 A for the total 906-turn HTS coils.

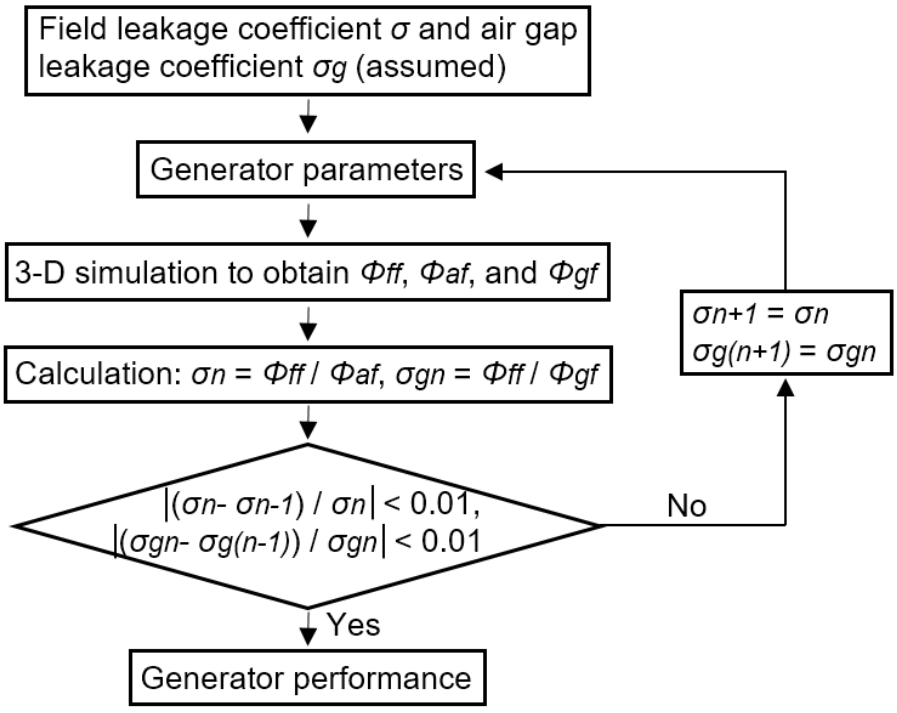

Fig. 4-11 Flowchart of calculating leakage coefficients.

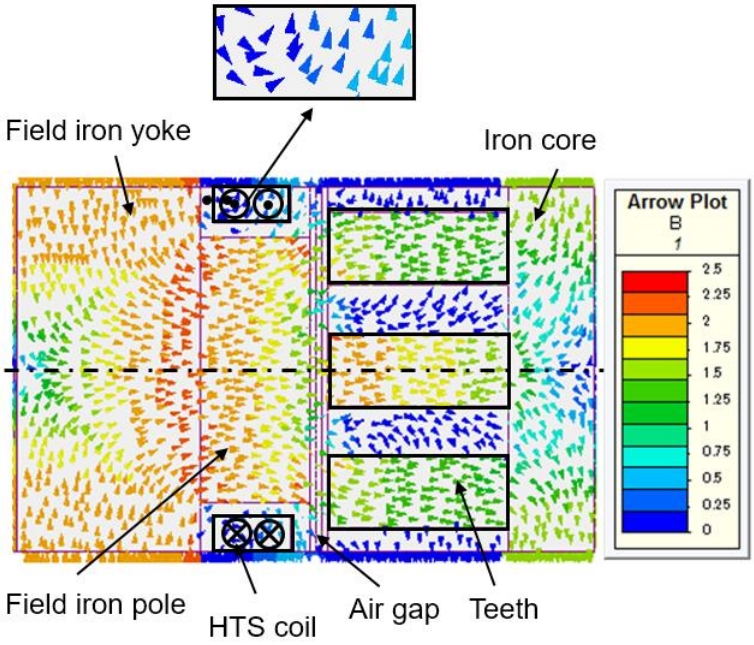

(a)

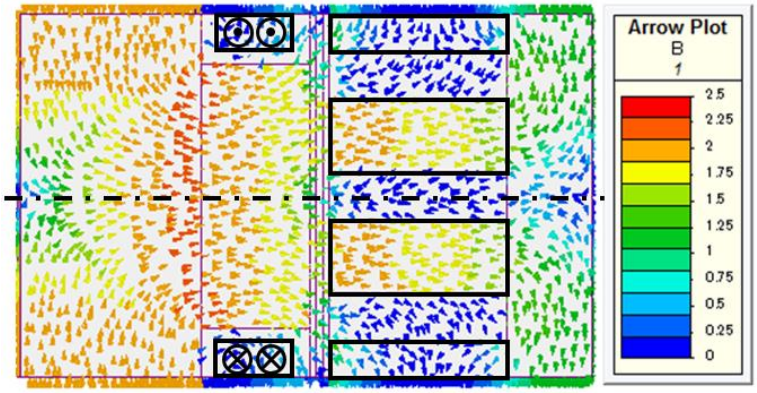

(b)

Fig. 4-12 Magnetic flux distribution in the cross section of the HTS-TLG in the case that (a) the center of field pole is faced to stator teeth; (b) the center of field pole is faced to stator slot.

Fig. 4-13 displays the values of magnetic fluxes in different circumferential surfaces under the “teeth center case” and the “slot center case”. Additionally, the average values of magnetic fluxes under these two cases are also shown in Fig. 4-13, as well as the design values. It is observed that the average interlinkage magnetic flux in each part under these two cases is well agreed with the design values, which demonstrates that the design results are accurate.

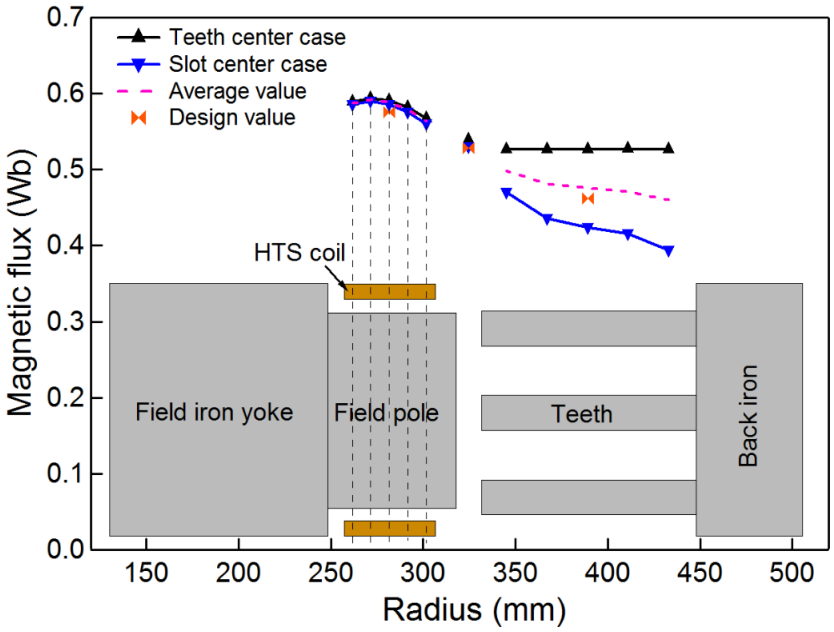

Fig. 4-13 Magnetic flux in the circumferential surfaces under different radial positions.

B. Calculation of HTS Heat Loss

HTS heat loss due to HTS flux flow affects the performance of HTS coils. The significances of calculating HTS heat loss lie in two aspects: One is to restrict the total HTS heat generation, which contributes to protect the HTS coils. On the other hand, HTS operating current decided by the HTS heat loss affects the volume of HTS coils used in the HTS-TLG. Therefore, with the determined HTS operating current, we adjust the height of field poles to fit the height of HTS coils in the design process, which makes design optimal. The HTS heat loss is evaluated by integrating the product of the current and voltage along the total length of the HTS coil [103], which is expressed as

$$W = \sum_{z,r,\varphi} \left\{ V_c I \left(\frac{I}{I_c(T,B,\theta)} \right)^{n(T,B,\theta)} r\Delta z \Delta r \Delta \varphi \right\} \tag{4-4}$$

where V_c is the critical voltage (in general 1 μV/cm). I is the HTS operating current. I_c (T, B, θ) and n (T, B, θ) are the critical current and n-value of HTS, which are dependent on the operating temperature T, applied magnetic flux density B, and flux angle θ. Here, T is decided as 77 K for easy cooling consideration. B and θ are obtained from 3-D simulation. Besides, n (T, B, θ) is set as 20 because of the low experienced magnetic flux density less than 0.5 T, as shown in Fig. 4-12. z, r, and φ are thickness, radius and angle of the HTS coil.

We plan to adopt the ReBCO superconductors, which has the I_c-B, θ properties at 77 K as shown in Fig. 4-14. Here, it is noted that the θ represents the angle between magnetic flux density and the c axis of HTS wires, as indicated by the inset of Fig. 4-14.

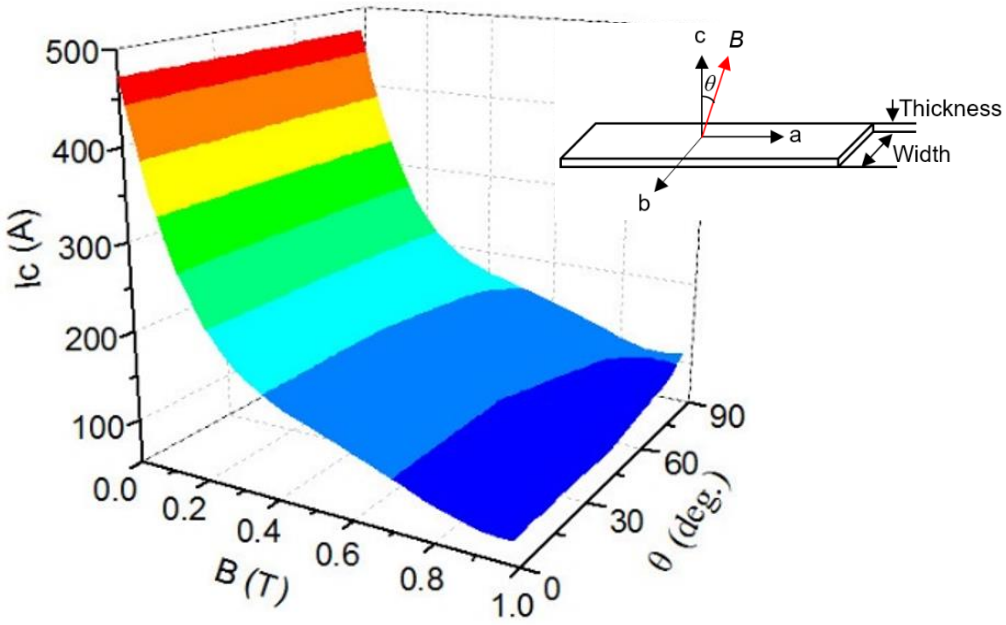

Fig. 4-14 I_c - B, θ properties of ReBCO at 77 K.

With 3-D simulation results of magnetic flux distribution in the HTS coil part, the total HTS heat loss for the entire machine at operating field currents of 66 A to 82 A is obtained, as shown in Fig. 4-15 [104]. Here, it is worth mentioning that the HTS operating currents are the load currents because the influence of armature reaction magnetic fluxes on the field of HTS coil is very small, mainly passing through iron poles. In this case, we considered non-linearity characteristics of HTS coils and the HTS heat generation was calculated based on the magnetic flux distribution in the HTS coils.

From Fig. 4-15, it is observed that the total heat loss is less than 20 W when HTS operating current is less than 72 A. And the heat is rapidly generated beyond the operating current of 77 A, at which point the total heat loss is 90 W. Here, the allowable heat loss is assumed to be 100 W taking the cooling capacity of the refrigerator into account. Moreover, considering actual cooling capacity and the HTS coil performance (load factor 0.85), the HTS operating current is set as 77 × 0.85 = 66 A.

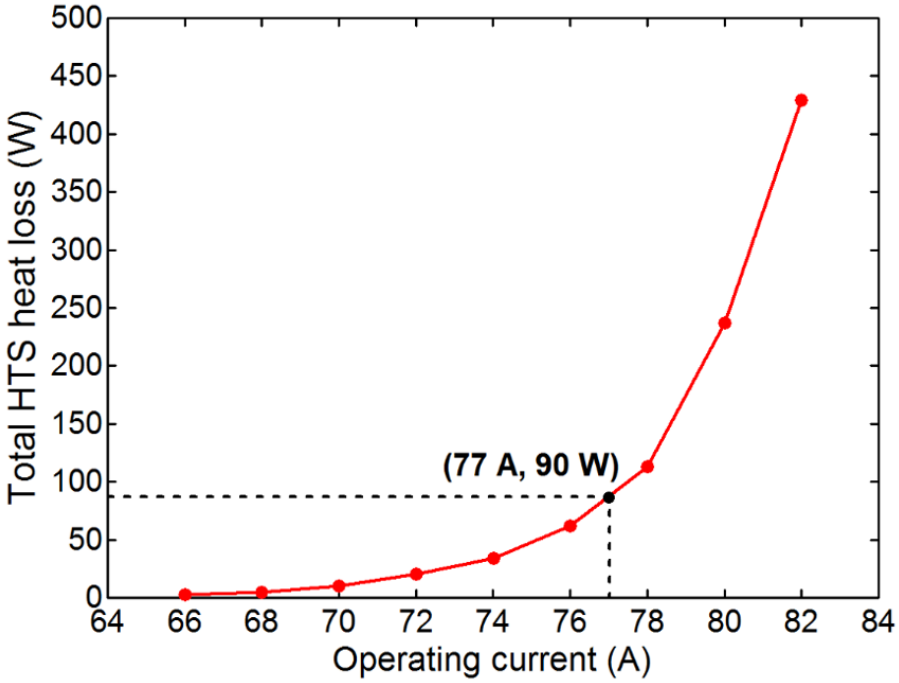

Fig. 4-15 Total HTS heat loss versus the operating current.

4.3 Design results of a 1 MW HTS-TLG

Design results of the 1 MW HTS-TLG are shown in Table 4-3. It is observed that electrical frequency of the HTS-TLG is 2.46 Hz, determined by the translator velocity and pole pitch, which is much higher than the wave frequency. Magnetic flux density in the air gap is up to 1.35 T, about twice that of conventional electric machines. The length of field part is 4.3 m, which is 3.7 m shorter than the stator for the sake of reducing HTS cost. The generator weight is about 44 tons. Efficiency of the HTS-TLG is up to 86%, including the required input power of cryocooler. The weight of HTS wires is only 0.4 tons, which implies the potential of reducing cost by applying HTS generators to WECs. In addition, weight of the translator is only 9.5 tons, which reduces the bearing load and the mechanical tensions on the heaving buoy.

Table 4-3 Design results of a 1 MW HTS-TLG.

Item	HTS-TLG
Operating temperature (K)	77
Maximum electrical frequency (Hz)	2.46
Number of field poles	18
Number of armature poles	34
Pole pitch (mm)	236
Field pole height (mm)	78
Field pole flux density (T)	1.9
Air gap flux density (T)	1.35
Effective armature teeth flux density (T)	2.05
Outer diameter of translator (m)	1.1
Length of field part (m)	4.3
Length of generator (m)	8.1
Number of turns per HTS coil	906
no-load HTS current (A)	46
No-load MMF (kA/pole)	42.0
Load MMF (kA/pole)	59.9
HTS winding weight (ton)	0.4
Total length of HTS windings (km)	30
Cryocooler weight (ton)	1.0
Generator weight (ton)	44.2
Stator weight (ton)	34.7
Translator weight (ton)	9.5
Total loss (kW)	162
Resistance loss of armature windings (kW)	126
Iron loss (kW)	10
Input power of cryocooler (kW)	8
Others* (kW)	18
Efficiency (%)	86.0

*Other losses include stray loss, mechanical loss, and blower power for air cooling.

4.4 Induced voltage and output power

4.4.1 Induced voltage

Firstly, we plot the electrical frequency of the HTS-TLG in Fig. 4-16(a) based on the following expression

$$f_e = \frac{v_{bm}}{2\tau}\left|\cos(2\pi f_0 t - \varphi)\right| \tag{4-5}$$

where v_{bm} is assumed as 1.2 m/s based on Fig. 2-4 in Chapter II, and τ is the pole pitch of the HTS-TLG, which is obtained from the design results as listed in Table 4-3.

Next, the flux linkage produced in the armature copper winding part is formulated as

$$\Psi(t) = \Psi_m \sin(\frac{\pi}{\tau} x_b) \tag{4-6}$$

where Ψ_m is the peak flux linkage.

Thereby, the induced phase voltage is obtained as

$$e_u = -n_e \cdot \frac{k_w}{k_\psi} \cdot \frac{d\Psi(t)}{dt} = \sqrt{2}E_0 \cdot \cos\left(\frac{\pi}{\tau}x_b\right) \cdot \cos(2\pi f_0 t - \varphi) \tag{4-7}$$

where, n_e is the series number of conductors per phase, k_w the winding factor, k_Ψ the flux distribution factor, and E_0 is the effective value of induced phase voltage. Per (4-7), a typical waveform of the induced phase voltage is depicted in Fig. 4-16(b). After a 3-phase bridge rectifier, the rectified 3-phase voltage under no-load condition is obtained in Fig. 4-16(c) according to the following expression

$$\begin{aligned} E_{d0} &= |e_u| + |e_v| + |e_w| = \sqrt{2}E_0 \cdot \left|\cos(2\pi f_0 t - \varphi)\right| \cdot \\ &\left\{\left|\cos\left(\frac{\pi}{\tau}x_b\right)\right| + \left|\cos\left(\frac{\pi}{\tau}x_b - \frac{2}{3}\pi\right)\right| + \left|\cos\left(\frac{\pi}{\tau}x_b + \frac{2}{3}\pi\right)\right|\right\}. \end{aligned} \tag{4-8}$$

From Fig. 4-16 (a), we observed that the electrical frequency varies in a sinusoidal form caused by the continuously changing velocity of the buoy. Consequently, the induced phase voltage varies in both amplitude and frequency during a wave cycle, as shown in Fig. 4-16 (b). It is worth noting that generators producing such kind of output power cannot be directly connected together due to the different frequencies. As a matter of factor, such induced voltage should be first rectified to a direct one. The rectified wave form after a 3-phase bridge rectifier is plotted in Fig. 4-16(c), which performs as a single wave form.

Moreover, the average value of the 3-phase rectified voltage E_d under load condition is evaluated as

$$\begin{aligned} E_d &= \frac{3\sqrt{2}}{\pi} \cdot \sqrt{3}E \cdot \left|\cos(2\pi f_0 t - \varphi)\right| \\ &= \frac{3\sqrt{2}}{\pi} \cdot V_t \cdot \left|\cos(2\pi f_0 t - \varphi)\right| \end{aligned} . \tag{4-9}$$

Here, the commutation angle is assumed to be zero. E is the phase voltage under load condition. And the 3-phase windings are in Y connection, in which case $V_t = \sqrt{3}E$.

On the other hand, the rectified current is

$$I_d = \frac{\pi}{\sqrt{6}} \cdot I_a \cdot \left|\cos(2\pi f_0 t - \varphi)\right| \tag{4-10}$$

where, I_a is the phase current.

From (4-9) and (4-10), the output power is obtained as

$$P_d = E_d I_d = \sqrt{3}V_t I_a \cos^2(2\pi f_0 t - \varphi) \tag{4-11}$$

Then, the average output power is

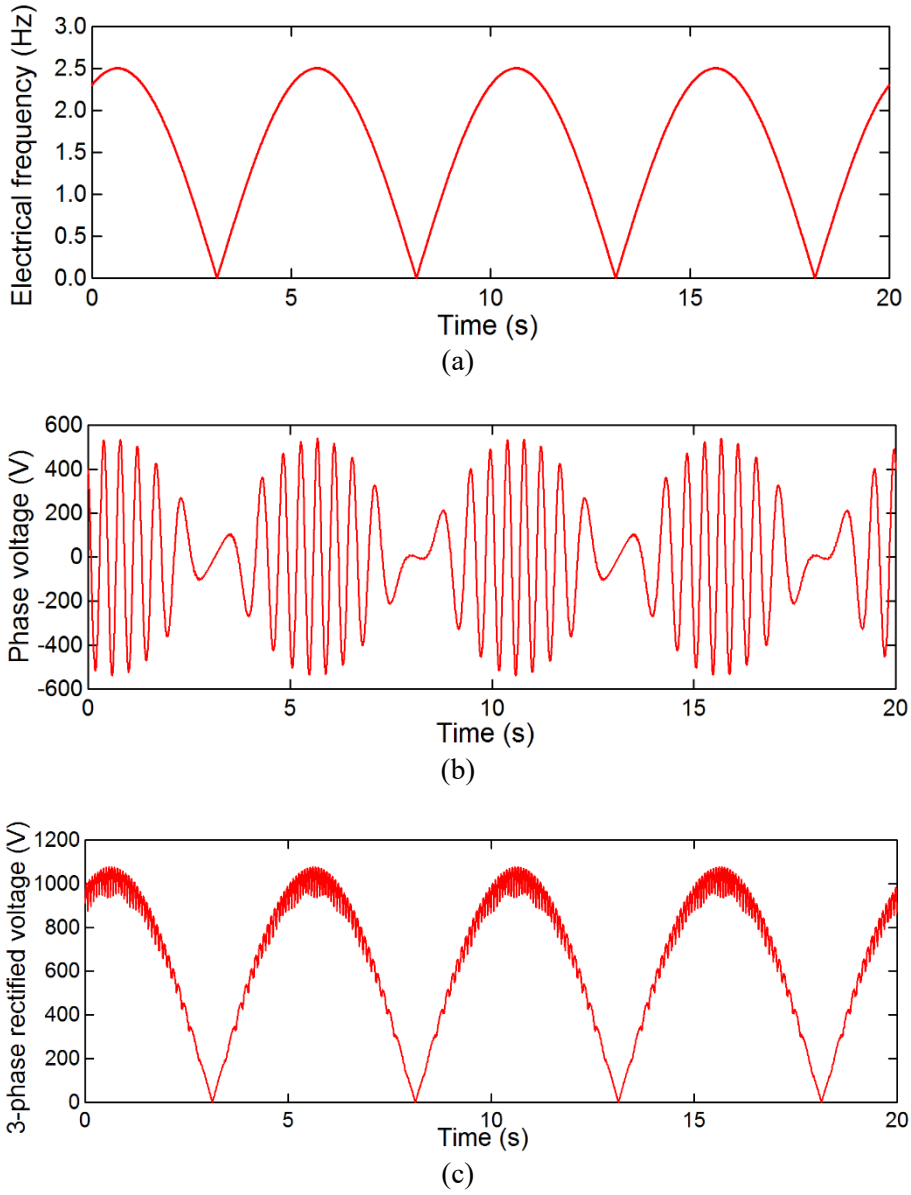

Fig. 4-16 Time dependence of (a) electrical frequency of the HTS-TLG; (b) induced phase voltage under load condition; (c) 3-phase rectified voltage under load condition.

$$P_{av} = \sqrt{3} V_t I_a \cdot \frac{1}{2} = \frac{1}{2} P_m \tag{4-12}$$

where P_m is the maximum output power of the HTS-TLG. It is indicated that the average output power is half of the maximum output power, and is evaluated as 500 kW.

4.4.2 Grid connection of output power

To connect the rectified output power produced by many WEC units to grid, there are basically two options. Here, each WEC unit includes a buoy, a linear generator, and a rectifier. One option is that each WEC unit has its own transmission cable to shore (Option-1). This

option features very simple configuration, however, it involves high installation costs of transmission cables and is not recommended to this study due to the long distance from WECs to grid. And the other option is to first connect all WEC units in one array, then, transmit the power of the array to grid by using one transmission cable (Option-2). This option could also be extended further. For instances, all the WEC units are first connected in several arrays, then transmit the power of these array to grid by using a small number of cables (Option-3), or connect each array in parallel, then, transmit the total power by using one cable (Option-4). These four options of connecting large amounts of WEC units for transmission can be found in Ref. [105] for detail.

Generally, expensive filters are required to do signal processing before the output power of WECs is connected to grid. To reduce cost of power conditioning, here, an economic concept is proposed. For the 1 MW WEC, as stated previously, the 3-phase rectified voltage of the HTS-TLG performs as a single wave form (period of T = 5 s). To connect such kind of output voltages to grid, it is suggested that every three WEC units are connected as one array, and the output power of the arrays could be transmitted to grid by using one cable or a small number of cables. Here, it is worth mentioning that the three WEC devices in one array are located to ensure that the output voltages differ T/3 in phase angle, as indicated in Fig. 4-17. This figure also shows relationships of the rectified voltages of the three WEC units. Fig. 4-18 plots the waveform of transmission voltage of one array, which shows that the transmission voltage of each array fluctuates around 2000 V.

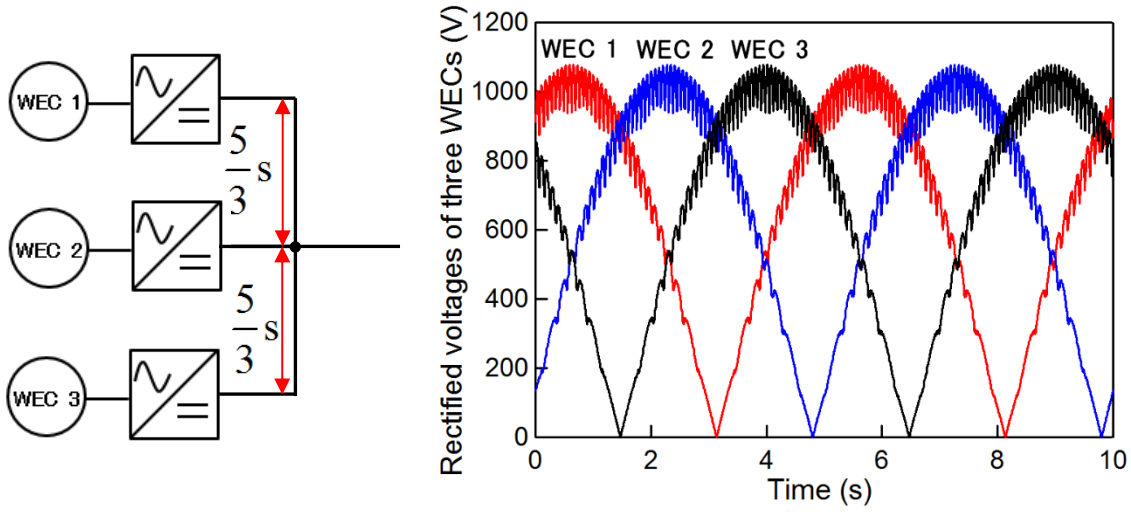

(a) (b)

Fig. 4-17 Connection of three WEC units. (a) Line diagram of one WEC array; (b) Rectified voltages of three WECs in one array.

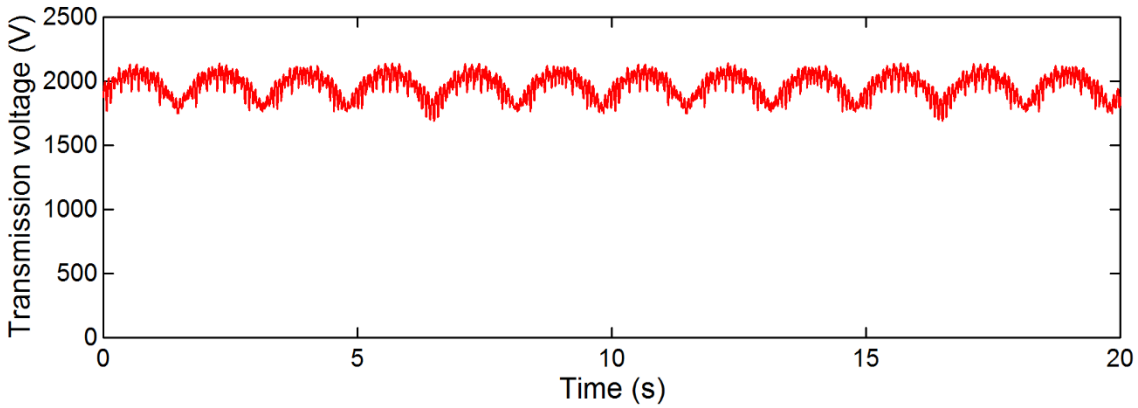

Fig. 4-18 Transmission voltage of three WEC units.

4.5 Conceptual structure of the improved WEC with the cooling system

For the proposed WEC, a large amount of mechanical parts is needed to fix the stator of TLGs to seabed, which are prone to be broken especially in harsh environment. To reduce the risk of being broken, structure of the WEC is improved to locate the converter at sea surface with moorings to keep it in place.

Fig. 4-19 shows the conceptual structure of the improved WEC with the HTS-TLG adopted. Compared to the previous structure, in addition to the heaving buoy used to extract wave power, another buoy is surrounded the outer armature part of the HTS-TLG. Size of the buoy is calculated to float the armature part in sea water, which is moored to seabed. On the other hand, Fig. 4-19 also shows the cryogenic cooling system of the WEC. Cryogenic tank and cryocooler are put inside of the heaving buoy, and are connected to the HTS coils with adiabatic tubes. HTS coils are interconnected through the iron pole pieces by using adiabatic tubes. The red arrows indicate the flow of LN_2, which is implanted to the cryogenic vessels from some tubes and comes out from the other tubes as gas, which is cooled down and re-used. Input power of the cryocooler comes from the output power of the HTS-TLG, which is rectified by using a converter, then is stored in a battery. The battery also provides the exciting current to HTS coils.

Moreover, location of bearings used between the stator and the translator is indicated in the magnified figure in Fig. 4-19. Bearings are installed in the upper and lower part of the outer surface of the translator to keep the airgap.

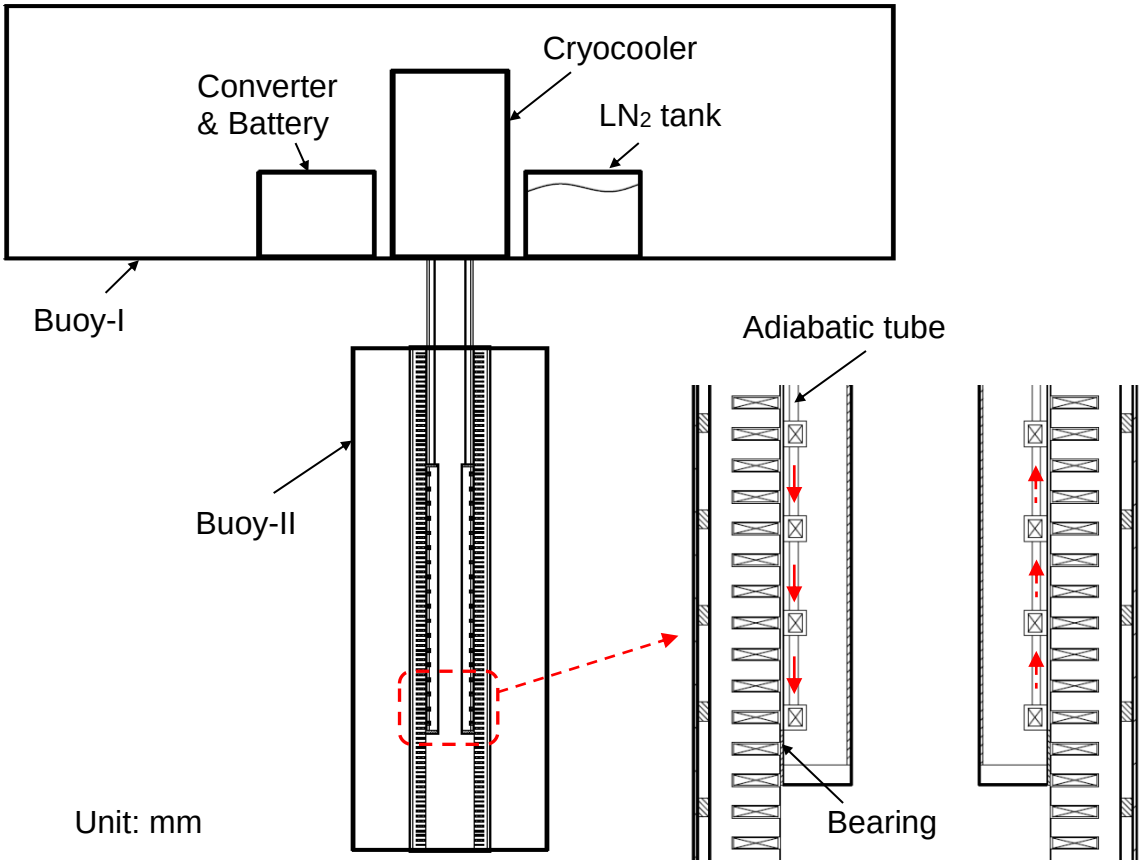

Fig. 4-19 Conceptual structure of the improved WEC with the cooling system.

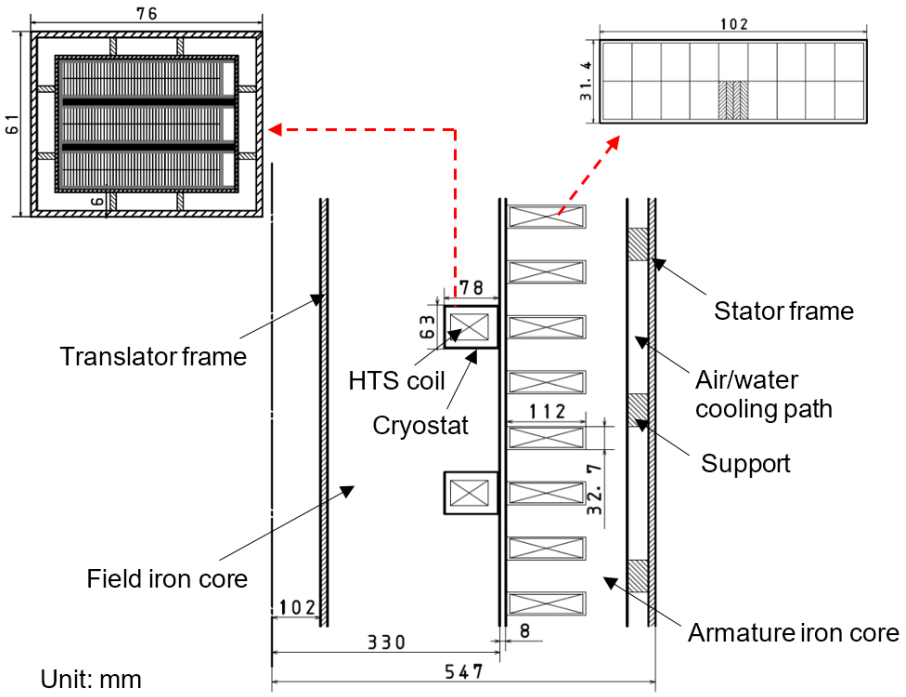

Fig. 4-20 Cross sectional view of the HTS-TLG, showing the configuration in detail.

For more detail, Fig. 4-20 shows the configuration of the HTS-TLG. For the field part, cross-sectional dimension of the slot that accommodates cryogenic vessel is 78 mm×63 mm, which is suited to put the cryogenic vessel with cross-sectional dimension of 76 mm × 61 mm. For the armature part, the cross-sectional dimension of slot and the configuration of armature conductors can be seen from Fig. 4-20. The armature conductors are arranged in two layers, which are wrapped with insulation tapes, then are inserted in the armature slots. Mechanical clearance between the outer surface of field part and the inner surface of armature part is 8 mm. Between the armature iron core and the stator frame, a cooling path is set for air or water cooling.

4.6 Cryogenic vessel and input power of cryocooler

4.6.1 Cryogenic vessel

Fig. 4-21 shows the cross section of the cryogenic vessel / cryostat (76 mm × 61 mm in dimension). Configuration of the cryogenic vessel is described here. The AMSC-8501 YBCO tapes (approximately 5 mm in width and 0.2 mm in thickness as described in Table 1-2) are used for winding HTS coils. In each cryogenic vessel, the HTS coils are arranged as three layers, which are stacked together to make one ring-shaped winding. Each layer comprises a double pancake HTS coil, surrounded with winding frames. The total number of turns per HTS winding is 906 turns (302 turns for the HTS coil in each layer).

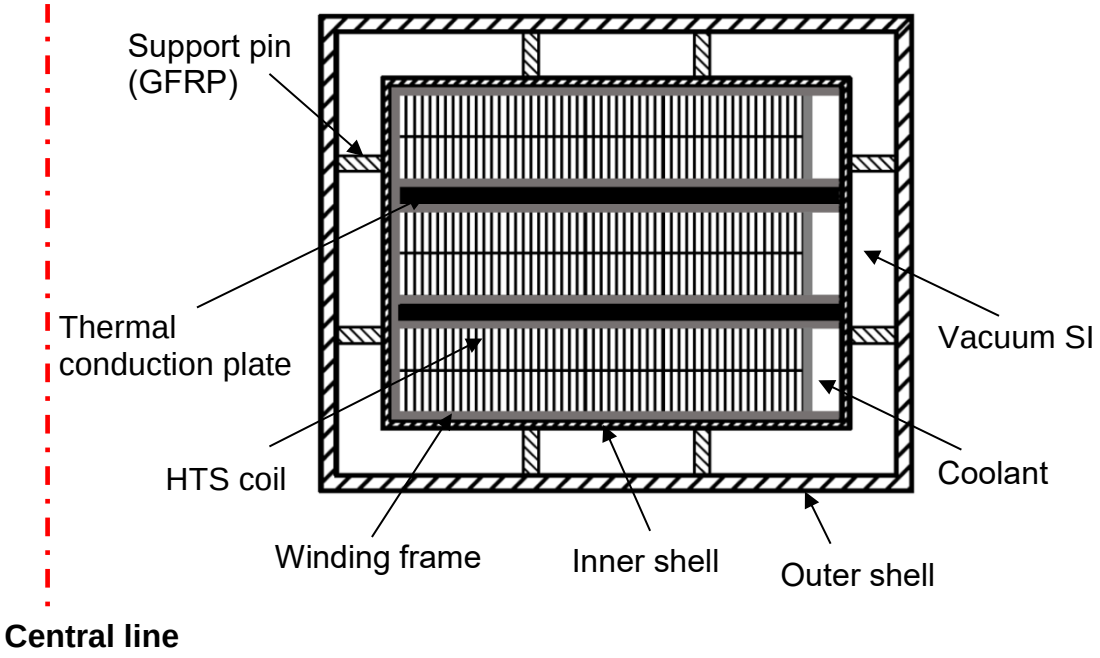

Fig. 4-21 Cross sectional view of the cryogenic vessel.

Approximately 550 m HTS tapes are needed to wind each double pancake HTS coil, and about 1650 m HTS tapes are used in each cryogenic vessel. Between the three-layer HTS coils there are thermal conduction plates for efficient cooling. In the right side of HTS coils, the frames are directly touched with coolant. Cross sectional area of the space for coolant is 11 mm×3 mm×3. Between the inner shell and the outer shell, there are support pins, which are made of GFRP, and have a length of 6 mm. The space between the inner shell and the outer shell is filled with super insulation (SI).

4.6.2 Various heat and input power of cryocooler

Input power of cryocooler plays a significant role in the selection of HTS cooling method and the design of cooling system. Input power of cryocooler of a HTS-TLG is dependent on the total heat generated in the HTS cryogenic vessel, which includes the conduction heat through GFRP pins, the invading heat through SI, the heat generated by HTS coils, and the conduction heat in conductor contact portion. Evaluation of these heat losses are presented as follows.

(1) Conduction heat through GFRP pins

The calculation of conduction heat through GFRP pins is expressed as

$$W_1 = \lambda A N P_f (\mathrm{T}_1 - \mathrm{T}_2) / L \ . \tag{4-13}$$

Here, λ is the thermal conductivity of GFRP, which varies with temperature, as listed in Table 5-1. A is the cross-sectional area of the GFRP pin, which is $\pi \times 2^2/4 \approx 3.14$ mm^2. N represents the number of pins per pole, which is 20×8 (20 pins in each side). And P_f is the number of field poles of the HTS-TLG. T_1 and T_2 are the temperatures in the ends of the pin, respectively. L is the length of the pin, which is 6 mm.

Table 5-1 Variation of GFRP thermal conductivity (λ) with temperature.

Temperature (K)	300	200	150	100	85	77
λ of GFRP (W/m·K)	0.8	0.62	0.525	0.425	0.37	0.345

By dividing the pin into 5 segments, and assuming the invaded heat in lower temperature side of each segment is the same (namely, $\mathrm{Q}_0 = \mathrm{Q}_1 = \mathrm{Q}_2 = \mathrm{Q}_3 = \mathrm{Q}_4$ in Fig. 4-22), the temperature distribution along the length of GFRP pin is obtained, as shown in Fig. 4-22. The higher end temperature T_1 is 300 K, and the lower end temperature T_2 is 77 K. It is noted that the temperature in the position that 0.401 mm away from the lower temperature side of the pin is 100 K. The average thermal conductivity between 77 K to 100 K is about 0.4 W/m·K. Then, the GFRP conduction heat W_1 can be evaluated as

$$W_1 = 0.4 \times 3.14 \times 20 \times 8 \times 18 \times (100 - 77) / 0.401 \times 10^{-3} = 207 \ \ [\mathrm{W}] . \tag{4-14}$$

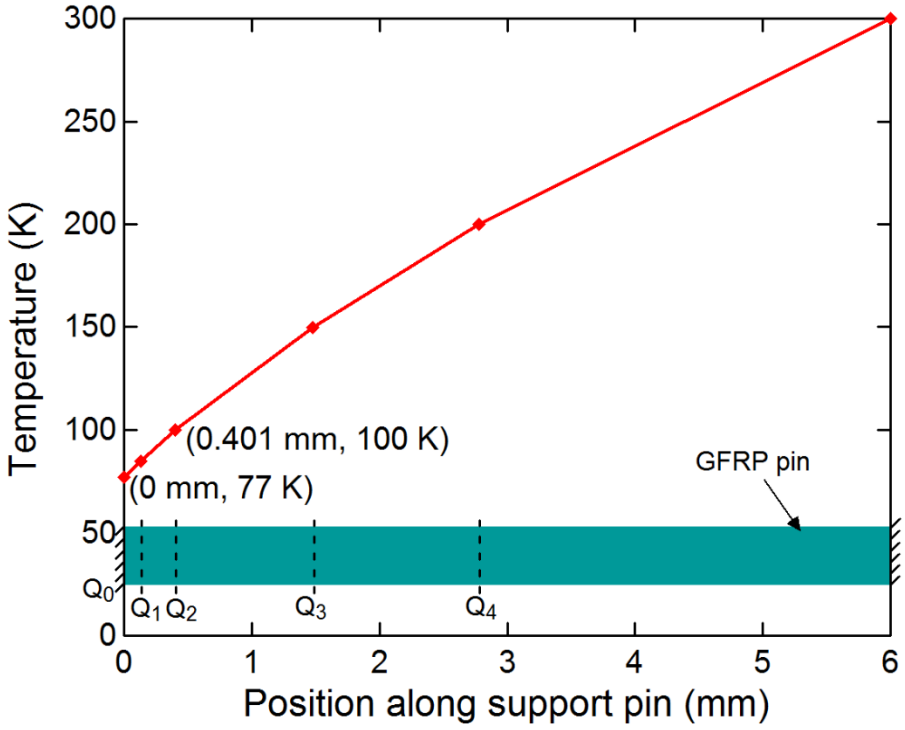

Fig. 4-22 Temperature distribution along the length of support pin.

(2) Invading heat through SI

The invading heat through SI is calculated as

$$W_2 = \lambda_{si} A_{si} P_f (\mathrm{T}_{1si} - \mathrm{T}_{2si}) / L_{si} \tag{4-15}$$

where λ_{si} is the thermal conductivity of SI, which is 3×10^{-4} W/m·K. A_{si} is the cross-sectional area of SI, and A = 1.5×0.452 = 0.678 m^2. T_{1si} and T_{2si} are the temperatures in the ends of the SI, which are 300 K and 77 K, respectively. And L_{si} is the length of SI, which is 6 mm. Consequently, the conduction heat through SI is

$$W_2 = 3\times10^{-4}\times0.678\times18\times(300-77)/6\times10^{3} = 136 \ \ [\mathrm{W}] \tag{4-16}$$

(3) Heat generated by HTS

As illustrated in Chapter III, at operating current of 77 A, the total HTS heat loss of the entire machine is 90 W. The actual operating current is decided as 66 A, at which the total HTS heat loss is evaluated as about half of that generated at 77 A. Therefore, the total HTS heat loss is evaluated as W_3 = 50 W.

(4) Heat loss in conductor contact portion

The resistance in conductor contact portion is considered to be less than 1 $\mu\Omega$. Then, under the operating current of 66 A, the heat generated in conductor contact portion is

$$W_4 = 1\times10^{-6}\times66^2\times2\times18 \approx 0 \ \ [\mathrm{W}]. \tag{4-17}$$

(5) Total heat generated by cryogenic vessels

As illustrated above, main heat of cryogenic vessels comes from the GFRP pins and the SI. The total heat loss is

$$W = W_1 + W_2 + W_3 + W_4 = 207 + 136 + 50 + 0 = 393 \ \ [\mathrm{W}]. \tag{4-18}$$

(6) Input power of cryocooler

Input power of cryocooler is determined by the coefficient of performance (COP) of a refrigerator, which stands for the efficiency of a refrigerator. The COP is expressed as

$$COP = \frac{Q}{P} \tag{4-19}$$

where, Q represents the heat generated by the considered system, and P is the required input power to the refrigerator. With the development of cryogenic refrigeration technology, COP of a refrigerator at 77 K can be up to 0.0622 [106]. With this kind of refrigerators, the input power to cryocooler is

$$P = \frac{393}{0.0622} \times 1.1 \times 1.15 = 8.0 \ \ [\mathrm{kW}] \tag{4-20}$$

where the 10% power is considered for cryogenic pumps, and another 15% power is for some margins considering long-time operation.

As discussed above, a Brayton-cycle refrigerator with 400 W cooling capacity at 77 K is suggested being adopted, which requires 8 kW input power considering coefficient of performance (COP) of the refrigerator. Another option is to use the cryogenic tank [107] to supply LN_2 to the HTS cryostats. And it is calculated that the HTS-LG consumes LN_2 about 210 L/day.

4.7 Conclusion

In this chapter, a HTS-TLG is designed for the WEC. The main contents and significant results are listed as follows:

(1) Structures of the proposed WEC and the HTS-TLG are described, which shows a very simple configuration with potential of reducing cost and maintenance.

(2) Electrical design process of HTS-TLGs is illustrated in detail. Novelty of the design program is that the electrical design is carried out automatically based on the input calculation equations of machine parameters. The program presents the generator performance corresponding to the geometric parameters, which makes it easy to obtain accurate machine parameters by studying the influences of main machine parameters on the basic generator performance.

(3) As the key technologies of designing HTS-TLGs, the determination of main machine

parameters, the method of calculating MMF, and the way of obtaining leakage coefficients and HTS heat loss by using 3-D simulation are described in detail. According to the calculating results of HTS heat loss, HTS operating current is decided as 66 A, in which condition the total HTS heat loss of the entire machine is evaluated as 50 W.

(4) Optimum design results of a 1 MW HTS-TLG is presented, which show a generator length of 8 m, a total weight about 44 tons, and an efficiency about 86%. Main features include: a) high air gap flux density of 1.35 T, about twice that of conventional electric machines; b) little amount of HTS wires adopted (only 0.4 tons), which implies a potential of reducing generator cost; c) a very light translator about 9.5 tons, which reduces the bearing load and the mechanical tensions on the heaving buoy.

(5) Waveforms of induced voltages of the 1 MW HTS-TLG are plotted, which demonstrate the feasibility of using this WEC to obtain desired output power. As the buoy velocity changes with time, electrical frequency of the HTS-TLG varies in amplitude. As a result, the induced voltage varies in both amplitude and frequency.

(6) An economic way of connecting the output power of many WECs to grid is proposed. It is suggested connecting every three WECs as one array, and allocating the WECs in each array to ensure that the output voltages differ $T/3$ in phase angle.

(7) Structure of the WEC is improved to locate the stator at the sea surface, thus reducing the mechanical parts to fix the stator to seabed. Besides, for the WECs with HTS-TLGs adopted, cryogenic cooling system is presented.

(8) Configuration of the cryogenic vessel is proposed, including the arrangement of the HTS coils. Various heat losses of the cryogenic vessels are calculated, which demonstrates that heat generation of the HTS-TLG mainly comes from the GFRP pins and SI. Total heat loss was estimated about 400 W. A cryocooler with 400 W capacity at 77 K will require 8 kW input power.

Chapter V Performance comparison of different TLGs

Conceptual structure of the WEC device has been described previously. A buoy on the sea surface moves vertically driven by the waves, which is connected to the translator of a TLG. Stator of the TLG is grounded to seabed via mechanical support part. In this chapter, different TLGs designed for the WEC are compared and discussed. Firstly, three types of TLGs are described, which are HTS-TLG, PM-TLG, and Cu-TLG depending on the different field exciting components. These TLGs are compared from the aspects of main machine parameters, the geometric and electromechanical characteristics, and the costs. Furthermore, design results of the HTS-TLG are compared to those of another HTS-TLG, which is designed based on different wave data of 2.5 m in height and 2.5 s in period.

5.1 Three types of TLGs

The three types of TLGs are identified as HTS-TLG, PM-TLG, and Cu-TLG by the different field exciting components, which are made of HTS coils, PMs, and conventional copper windings, respectively. The TLGs are chosen as they have little attractive force between the stator and the translator, as well as low armature resistance and inductance. Conceptual structures of these TLGs are described as follows, and the electrical design method is further introduced.

Fig. 5-1(a) depicts the partial cross section of the HTS-TLG. The stator is composed of HTS field windings, cryogenic vessel to support HTS coils, field iron poles, and iron yoke. And the translator is made of iron-cored armature copper windings. Merits of the HTS-TLG lie in that HTS field part is inside of the HTS-TLG, and is designed shorter than the stator to reduce the amount of HTS wires, thus reduce the cost. Moreover, this structure makes it easy to support the HTS coils because the cryogenic vessels containing HTS coils are put around the iron poles.

Fig. 5-1(b) shows the cross-sectional view of the PM-TLG, in which PMs are mounted on the translator with alternating polarity. Armature part of the PM-TLG consists of iron-cored armature windings. It is worth mentioning that the inner armature part is fixed to seabed as a stator, and the outer PM part is chosen as a translator which is designed shorter than the stator to save PMs, in consideration of 1) avoiding the movement of cables used for transferring the generated electric power; 2) reducing the mechanical tensions on the buoy by connecting the buoy with the lighter PM part. On the other hand, the outer PM structure

benefits for reducing the generator volume compared to the inner PM structure due to the determined magnetic flux per pole in the armature part

Fig. 5-1(c) shows the cross-sectional view of the Cu-TLG. The outer armature part is composed of iron-cored copper windings, and is chosen as the stator to avoid the movement of transmission cables. The inner field part is the translator, which is shorter than the outer stator. Conventional copper windings are adopted to form the field exciting component.

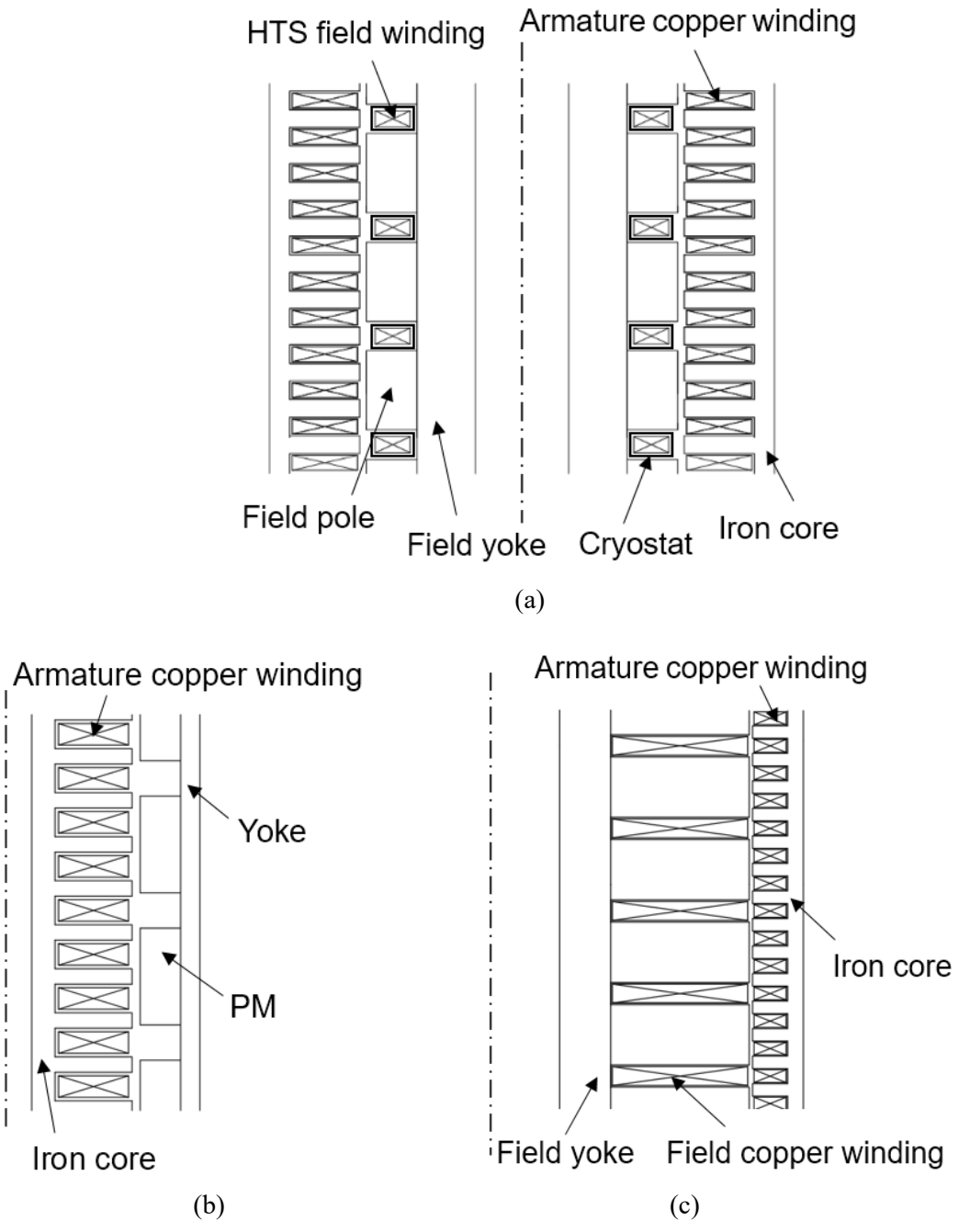

Fig. 5-1 Cross-sectional view of (a) the HTS-TLG; (b) the PM-TLG; (c) the Cu-TLG.

5.2 Optimal design of Cu-TLGs

To get optimal design of the Cu-TLG, main machine parameters are first determined by studying their influences on the basic performance of Cu-TLGs. Then, the field leakage coefficient and the air gap leakage coefficient are calculated to make design results more accurate. These methods are the same as what have been done to design the PM-TLG and the HTS-TLG.

5.2.1 Determination of main machine parameters

Design results under different generator length is shown in Fig. 5-2, which shows the basic generator performance of the Cu-TLG with respect to different generator length. Here, the generator length represents the length of outer armature part. It is observed that when the length of the Cu-TLG is 8.1 m, both the generator weight and the field copper winding weight are lightest, together with the highest generator efficiency. With the increase of generator length, the generator weight and the field copper winding length decrease then increase when the generator length is beyond 8.1 m. The reasons are the same as explained in Section 4.2.3. On the other hand, the generator efficiency keeps increasing till the generator length is up to 8.1 m due to the increasing ratio of the effective armature length to the total armature length. However, when the generator is longer than 8.1 m, increasing the generator length at constant maximum diameter leads to an increase in the length and resistance of the armature windings, thus decreasing the efficiency.

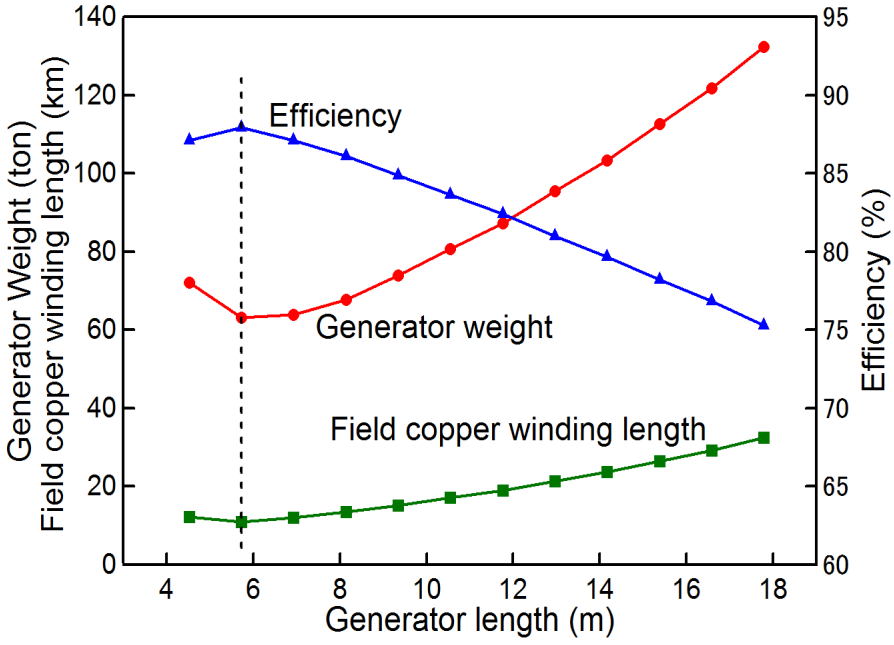

Fig. 5-2 Variation of Cu generator weight, field copper winding weight, and generator efficiency with respect to length of the Cu-TLG.

Fig. 5-3 shows the influence of pole pitch on the basic performance of Cu-TLGs. It is worth noting that the number of field poles is the same for each case, therefore, the increasing pole pitch leads to longer generator with smaller diameter. As a result, it is observed that increasing pole pitch at a constant minimum diameter results in increasing weight of Cu-TLGs, decreasing efficiency of Cu-TLGs, and decreasing length of field copper windings. The reasons are the same as explained in Section 4.2.3.

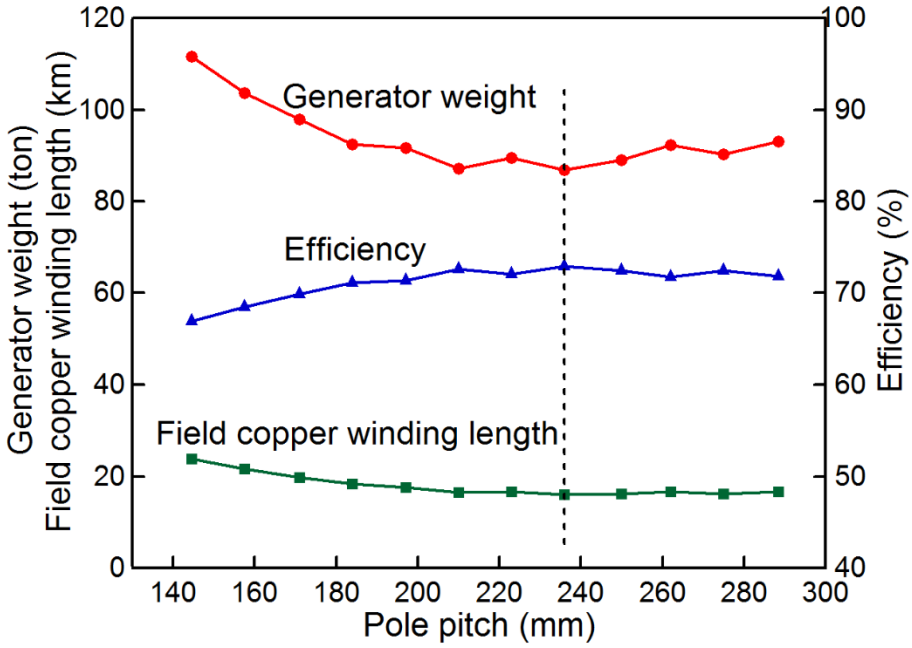

Fig. 5-3 Variation of Cu generator weight, field copper winding weight, and generator efficiency with respect to pole pitch of the Cu-TLG.

5.2.2 Calculation of leakage coefficient

With 3-D simulation, the magnetic fluxes in the circumferential surfaces under different radial positions of the Cu-TLG are shown in Fig. 5-4, under the "teeth center case" and the "slot center case", respectively. It shows that the magnetic fluxes in the armature winding regions are much lower than those in the field winding regions for both the two cases, due to the flux leakage caused by the long field pole height (380 mm). And the flux in the armature winding region under the "slot center case" is much lower than that under the "teeth center case". The field leakage coefficient is the ratio of the average Φ_{ff} to the average Φ_{af}, which is calculated as 1.383 for the "teeth center case" and 1.659 for the "slot center case", respectively. Consequently, the field leakage coefficient is calculated as $\sigma_f = (1.383+1.659)/2 \approx 1.52$. The air gap leakage coefficient is the ratio of the average Φ_{ff} to the average Φ_{gf}, which is calculated as $\sigma_g = (1.335+1.387)/2 \approx 1.36$

In addition, the average magnetic flux density in the circumferential surfaces of different

parts (field copper winding region, air gap center, and armature winding region) is also exhibited in Fig. 5-4. It is observed that the average magnetic flux density drops sharply in the field copper winding part due to the long field pole height (380 mm). As a result, the flux density in the armature winding part is much lower than that in the field winding part. Additionally, by comparing the flux density in the armature winding part under the "teeth center case" and the "slot center case", it is seen that the flux density under the "slot center case" is much lower than that under the "teeth center case" (Maximum difference about 24% lower).

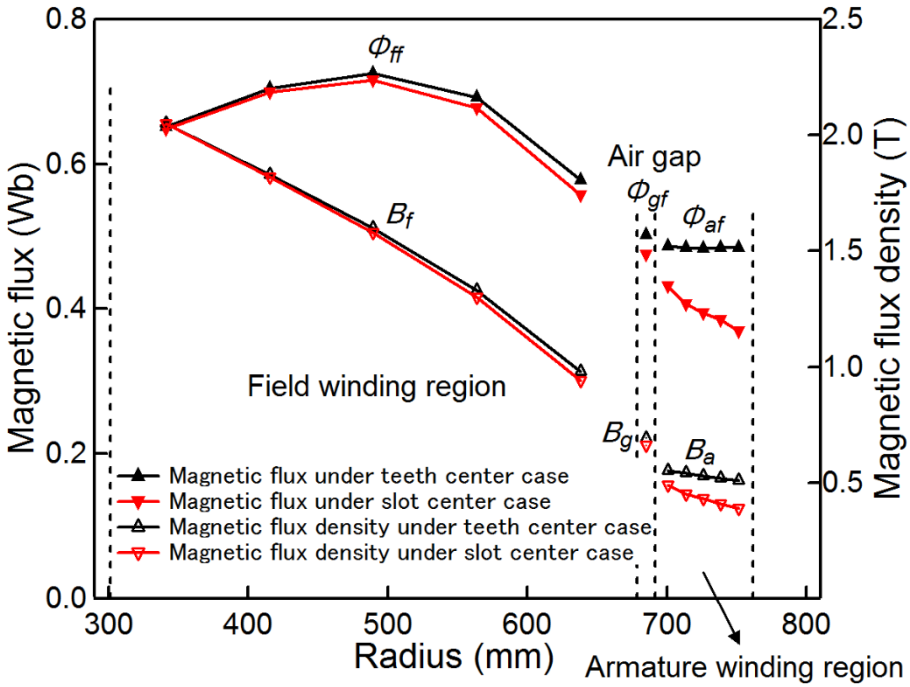

Fig. 5-4 Magnetic flux and the average flux density in the circumferential surfaces under different radial positions of the Cu-TLG.

5.3 Design results of three types of TLGs and performance comparison

Design results of the three types of TLGs are presented in Table 5-1. We will compare the performance of these TLGs from two aspects. One is to compare the geometric and electromagnetic performance, such as generator weight, size, efficiency, field conductor/ PM weight, magnetic flux density, and so on, to select a most suitable one for off-shore WEC. The other aspect is to compare the cost, which plays an important role in the commercialization of the WECs.

Table 5-1 Design results of 1 MW TLGs for WECs.

Item	Cu-TLG	PM-TLG	HTS-TLG
Operating temperature (K)	348	323	77
Maximum electrical frequency (Hz)	2.46	3.15	2.46
Number of field poles	18	42	18
Number of armature poles	34	62	34
Pole pitch (mm)	236	184	236
Field pole height (mm)	380	60	78
Field leakage coefficient	1.52	1.31	1.24
Air gap flux density (T)	0.64	0.53	1.35
Outer diameter of generator *Do* (m)	1.7	1.3	1.1
Inner diameter of generator *Di* (m)	0.1	0.6	0.2
Length of generator *Ls* (m)	8.1	11.5	8.1
Generator volume $\pi/4 \times (Do^2 - Di^2) \times Ls$ (m^3)	18.3	12.0	7.4
Load MMF (kA/pole)	36.5	53.7	59.9
Cu/PM/HTS field conductor weight (ton)	7.8	8.3	0.4
Total length of Cu/PM/HTS field conductor (km)	16	—	30
Weight of cryocooler (ton)	—	—	1.0
Generator weight (ton)	86.9	51.3	44.2
Stator weight (ton)	42.5	30.5	34.7
Translator weight (ton)	44.4	20.8	9.5
Total loss (kW)	372	231	162
Resistance loss of armature windings (kW)	234	200	126
Iron loss (kW)	6	5	10
Input power of cryocooler (kW)	—	—	8
Resistance loss of field windings (kW)	105	—	—
Others* (kW)	27	26	18
Efficiency (%)	72.9	81.2	86.0

*Other losses include stray loss, mechanical loss, and blower power for air cooling.

5.3.1 Comparison of geometric and electromechanical characteristics

From Table 5-1, we observed that the length of both Cu-TLG and HTS-TLG is shorter than the PM-TLG, which is about 7/10 of that of the PM-TLG. However, the total weight of the Cu-TLG is much higher than that of the PM-TLG and the HTS-TLG. The disadvantage in weight, especially the heavy translator, makes the Cu-TLG difficult in off-shore WEC application. The heavy translator increases requirements for mechanical strength of bearings and the mechanical construction of the buoy. Besides, efficiency of the Cu-TLG is low due to the high resistance loss of the armature copper windings and the field copper windings.

Next, the PM-TLG with length of 11.5 m and diameter of 1.3 m has a total weight about 51 tons, and an efficiency about 81%. Translator weight of the PM-TLG is about 21 tons, much lighter than that of the Cu-TLG. Therefore, the acceptable weight and length make the PM-TLG a candidate of the WEC device.

Furthermore, we observed that the air gap flux density of the HTS-TLG is up to 1.35 T due to the adoption of HTS wires, which is out of reach for the conventional Cu-TLG and

the PM-TLG. Thanks to the high air gap flux density achieved by the HTS coils, the HTS-TLG yields a very compact structure, with about 3/5 volume of the PM-TLG and much less volume than the Cu-TLG. Correspondingly, the HTS-TLG has a lightest weight about 44 tons, which is about 85% of the weight of the PM-TLG, and half of that of the Cu-TLG. In addition, efficiency of the HTS-TLG is highest even the cooling system is used. The most compact structure, the lightest weight, and the highest efficiency make the HTS-TLG the preferred candidate in off-shore WEC application.

5.3.2 Comparison of cost

To investigate the potential of these three types of TLGs used for WECs in commercial application. We compared the costs of these TLGs, and the comparison results are listed in Table III. Here, HTS future price is assumed as 3 Y/(Am) at 77 K (self-field), which is about US 27 $/(kAm) at the current exchange rate of 111 Y per US $. PM present price is assumed as 30 Y/g, about 270 $/kg. Refer to each item of the Cu-TLG, costs of the PM-TLG and the HTS-TLG is normalized. We found the total cost of the HTS-TLG is lowest, which is 0.7 times of that of the Cu-TLG. Due to the high-priced and large number of PMs used in the PM-TLG, the cost of the PM-TLG is highest, about 1.9 times of that of the Cu-TLG, which implies that the PM-TLG is not a promising one for large-scale WEC application in the economical viewpoint.

In Table 5-2, accessories of the TLGs include the air-cooling device, lubricant device, exciting devices for the Cu-TLG and the HTS-TLG, and the cryogenic refrigeration system for the HTS-TLG. Cost of accessories of the PM-TLG is lowest due to the absence of exciting device for the field PMs. Besides, miscellaneous works include assembly, test, and transportation.

Table 5-2 Cost comparison of 1 MW TLGs.

Item	Cu-TLG	PM-TLG	HTS-TLG
Operating temperature (K)	348	323	77
Cost of field conductor/PM	1	21.3	1.4
Cost of field part	1	4.7	0.8
Cost of armature copper windings	1	0.9	0.5
Cost of armature part	1	0.8	0.7
Cost of accessories	1	0.4	1.0
Cost of miscellaneous works	1	1.7	1.1
Cost of LGs	1	1.9	0.7

5.3.3 Main performance and evaluation

We list the main items in Table 5-3 to show the features of these TLGs in WEC application, which are summarized as follows:

- The Cu-TLG has a small ratio of generator length versus its outer diameter (8.1 m versus 1.7 m), which implies a good structural robustness of the generator. Nevertheless, the heavy weight brings a big challenge in mechanical structure and strength of the buoy.
- The PM-TLG presents relatively light weight and high efficiency, which makes it an option in WEC application. However, due to the large number of high-priced PMs are used, this PM-TLG is the most expensive one.
- The HTS-TLG exhibits lightest weight, highest efficiency and lowest cost among these three types of TLGs. Particularly, HTS wires used to form the field exciter are only 0.4 tons, much less than the weight of field copper windings and PMs, which indicates the potential of reducing cost by using the HTS-TLG.

Table 5-3 Performance comparison of 1MW TLGs.

Item	Cu-TLG	PM-TLG	HTS-TLG
Operating temperature (K)	348	323	77
Field pole height (mm)	380	60	78
Generator length (m)	8.1	11.5	8.1
Outer diameter of LGs (m)	1.7	1.3	1.1
Stator weight (ton)	42.5	30.5	34.7
Translator weight (ton)	44.4	20.8	9.5
Generator weight (ton)	86.9	51.3	44.2
Generator efficiency (%)	72.9	81.2	86.0
Generator cost (pu)	1	1.9	0.7
Estimation	Poor	Fair	Good

5.4 Performance comparison of different HTS-TLGs

Another HTS-TLG, represented as HTS-TLG※, is designed based on the wave data of 2.5 m in height and 2.5 s in period, in which case maximum stroke of the HTS-TLG※ is 2 m, and the peak velocity is about 2.5 m/s, which are close to the wave assumptions in Ref. [42] and [87]. In Ref. [42], a direct-drive C-GEN machine is tested with a hydraulic ram driving it at 0.4 Hz and 2 m/s. And in Ref. [87], maximum stroke of a direct-drive air-cored SCLG is 2.4 m, and the peak velocity is 2.2 m/s. Electrical design of the HTS-TLG※ was conducted in order to: 1) investigate the advantages of the proposed structure compared to that presented in Ref. [87]; 2) figure out the influence of wave data on the design results of the HTS-TLGs by comparing the machine performance and cost of the HTS-TLG to those of the HTS-TLG※, which are designed with different wave data.

5.4.1 Design results of a 2 MW HTS-TLG and discussion

Design results of the 2 MW HTS-TLG※ are presented in Table 5-4. For the HTS-TLG※, it is worth mentioning that the line current is 1750 A. Slot number/pole/phase is 1. Current density in armature copper conductor is assumed to be 3 A/mm^2 and the fill factor is 0.7. Electric loading is 1000 A/cm. And field pole width/pole pitch is 0.73. The design results show that the 2 MW HTS-TLG※ is 9.3 m long, and 0.8 m in outer diameter. And the HTS-TLG※ exists total weight of 28.2 tons (including the cooling system), translator weight of 6.8 tons, HTS field winding length of 17 km (AMSC's HTS wires with 5 mm × 0.2 mm in cross-sectional dimension), and an efficiency of 92.6 %.

Table 5-4 Design results of the 2 MW HTS-TLG※.

Item	HTS-TLG※
Operating temperature (K)	77
Maximum output power (MW)	2
Maximum electrical frequency (Hz)	8.4
Number of field poles	48
Number of armature poles	62
Pole pitch (mm)	149
Field pole height (mm)	63
Air gap flux density (T)	1.16
Outer diameter of generator *Do* (m)	0.8
Inner diameter of generator *Di* (m)	0.1
Length of generator *Ls* (m)	9.3
Generator volume $\pi/4 \times (Do^2 - Di^2) \times Ls$ (m^3)	4.7
Load MMF (kA/pole)	26.8
HTS field winding weight (ton)	0.2
Total length of HTS field windings (km)	17
Generator weight (ton)	27.2
Stator weight (ton)	20.4
Translator weight (ton)	6.8
Total loss (kW)	160
Resistance loss of armature windings (kW)	98
Iron loss (kW)	21
Input power of cryocooler (kW)	8
Others* (kW)	30
Efficiency (%)	92.6

*Other losses include stray loss, mechanical loss, and blower power for air cooling.

Table 5-5 compares the main machine performance of the 2 MW HTS-TLG※ to that of the air-cored SCLG proposed in Ref. [87]. For the HTS-TLG※, with the wave assumptions of 2.5 m in height and 2.5 s in period, the value of f_0A^2 is almost the same with that of the SCLG, which is proportional to the maximum output power of the linear generators as shown by Eq. (2-17) . Furthermore, maximum linear speeds of these two generators are similar. The above descriptions indicate that these two linear generators are designed under similar

conditions. In addition, it is noted that the SCLG also adopts the AMSC's copper laminated Amperium wire, which has a current density of 82 A/mm^2 and cross-sectional dimension of 12 mm × 0.2 mm. By comparing the HTS-TLG※ to the SCLG, some conclusions are drawn as follows:

- Maximum output power of the HTS-TLG※ is more than 1.5 times than that of the SCLG.
- Length of these two linear generators is almost the same.
- The SCLG has a much lighter translator than the HTS-TLG※ due to its air-cored structure. And the total weight of SCLG is about 3/4 that of the HTS-TLG※.
- Power density (P_m / W_g) of the HTS-TLG※ is 18% higher than that of the SCLG.
- The HTS-TLG※ adopts 17.5 km × 5 mm × 0.2 mm AMSC's HTS wires, and the SCLG adopts about 27.4 km × 12 mm × 0.2 mm AMSC's HTS wires, which indicates that the HTS-TLG※ uses much less amount of expensive HTS wires (less than 1/2), implying a substantial reduction of costs.

As discussed above, the proposed HTS-TLG※ has some potential advantages than the SCLG, especially the higher power density and lower cost. Therefore, despite the advantages of the SCLG like stationary superconducting coils, a light translator, and elimination of attractive forces between stator and translator, the HTS-TLG※ is more promising for off-shore large-scale WEC application in viewpoints of both physical parameters and economics.

Table 5-5 Performance comparison of the HTS-TLG※ and the SCLG [87].

Item	HTS-TLG※	SCLG
Maximum output power P_m (kW)	2000	2×640
Terminal voltage (V)	660	1010
Line current (A)	1750	732
Wave frequency f_0 (Hz)	0.4	0.3
Maximum stroke A (m)	2.0	2.4
f_0A^2 ($P_m \propto f_0A^2$)	1.6	1.7
Maximum linear speed (m/s)	2.5	2.2
Generator length (m)	9.3	9.6
Length of SC wire (km)	17.5	27.4
Stator weight (ton)	20.4	18.5
Translator weight (ton)	6.8	3.0
Weight of generator with cryocooler W_g (ton)	28.2	21.5
P_m / W_g (kW/ton)	71	60

5.4.2 Comparison of main performance and cost of different HTS-TLGs

Table 5-6 shows the main machine parameters of the two HTS-TLGs designed with different wave data. The HTS-TLG is 1.2 m shorter than the HTS-TLG※ with a larger outer diameter, which indicates that the HTS-TLG is more robust. Besides, it is noted that the HTS-TLG uses more HTS wires, about 80% longer than that of the HTS-TLG※. Moreover, the HTS-TLG exhibits disadvantages in all the generator weight, translator weight, and generator efficiency compared to the HTS-TLG※. Both total generator weight and translator weight of the HTS-TLG are about 1.5 times higher than those of the HTS-TLG※, and the efficiency is about 7% lower. The above discussions verify that HTS-TLGs designed with different wave data exhibit very different generator performance. Therefore, it is important to design HTS-TLGs based on realistic wave data of some specific locations.

Table 5-6 Performance comparison of two HTS-TLGs.

Item	HTS-TLG	HTS-TLG※
Maximum output power (MW)	1	2
Operating temperature (K)	77	77
Field pole height (mm)	78	78
Generator length (m)	8.1	9.3
Outer diameter of TLGs (m)	1.1	0.8
Total length of HTS field windings (km)	30	17
HTS operating current (A)	66	105
Stator weight (ton)	34.7	20.4
Translator weight (ton)	9.5	6.8
Generator weight (ton)	44.2	27.2
Generator efficiency (%)	86.0	92.6

Table 5-7 compares the cost of the two HTS-TLGs. It is observed that cost of field part of the HTS-TLG※ is 1.5 times higher than that of the HTS-TLG, even cost of HTS wires of the HTS-TLG※ is less than that of the HTS-TLG. It is because that the HTS-TLG※ is longer, which adopts more HTS cryogenic vessels. And the price of cryogenic vessels is high. This result implies that it is better to adopt less number of field poles when designing such kind of HTS-TLGs, which would benefit for reducing costs. In addition, it is shown that the costs of both armature copper windings and armature part of the HTS-TLG※ are less than those of the HTS-TLG, because the HTS-TLG※ adopts less copper wires and has a lighter stator as shown in Table 5-6. However, the overall costs of these TLGs are same.

Table 5-7 Cost comparison of two HTS-TLGs.

Item	HTS-TLG	HTS-TLG※
Maximum output power (MW)	1	2
Cost of field HTS wires	1	0.9
Cost of field part	1	1.5
Cost of armature copper windings	1	0.8
Cost of armature part	1	0.7
Cost of accessories	1	1.0
Cost of miscellaneous works	1	1.0
Cost of TLGs	1	1.0

5.5 Conclusion

This chapter aims to compare different HTS linear generators designed for direct-drive WECs. Main conclusions are drawn as follows.

Comparison results among the three types of TLGs show that

(1) The Cu-TLG exhibits more robust structure, nevertheless, the heavy weight brings a big challenge in reduction of cost and mechanical tensions on the buoy.

(2) The PM-TLG presents relatively light weight, high efficiency but high cost.

(3) The HTS-TLG has distinguished advantages in weight, efficiency, and cost. Particularly, only 0.4 tons HTS wires are used to form the field exciting component, much less than the weight of field copper windings and PMs used in the Cu-TLG and PM-TLG, respectively.

Design results of a 2 MW HTS-TLG, which is designed under wave assumptions of 2.5 m in height and 2.5 s in period, are compared to those of a SCLG [87]. Comparison results imply that the proposed HTS linear generator with tubular structure is more promising for off-shore large-scale WEC application in viewpoints of both physical parameters and economics.

Comparisons between the two HTS-TLGs designed with different wave data indicate that the wave height and period affect the physical and electromagnetic characteristics of the HTS-TLGs.

Chapter VI Summary and future research

6.1 Summary

In this thesis, electrical design studies of large-scale TLGs proposed for a WEC system was conducted. The main purpose of this thesis is to breakthrough some key design technologies of HTS-TLGs used for direct-drive WECs, and make clear their advantages over the conventional TLGs in WEC application.

Firstly, the WEC systems and the direct-drive devices are introduced. Features of the present PM-LGs and HTS-LGs proposed for direct-drive WECs are described, including the fundamental properties of superconductors, and the state-of-the-art of HTS technologies.

Next, ocean wave characteristics were investigated to ensure that the studies in this thesis are carried out based on realistic wave data. Afterwards, the electrical system of a direct-drive WEC was presented. About this system, structural merits of the WEC device were highlighted. Buoy movement was analyzed to show the basic operation principle of the WEC. And the relation of buoy size and maximum output power was clarified. These works are indispensable for designing the overall WEC system.

Then, as the generally adopted electric machines in direct-drive WECs, electrical design of PM-TLGs was conducted. Compared to the conventional way of designing a PM machine, novelties of the electrical design method of PM-TLGs mainly lie in a more flexible and efficient approach of determining main machine parameters, a more accurate way of obtaining leakage coefficients by using 3-D simulation, and an easier and more accurate method of evaluating PM operating point. To verify the accuracy of design results of 1 MW PM-TLGs, magnetic flux density distribution of a PM-TLG was analyzed, which exhibits very good agreements of simulation results and design values. The successful design of the PM-TLGs established the foundation for designing HTS-TLGs.

Chapter IV presented the most important contents of this thesis, such as the electrical design method of HTS-TLGs (the design process, the method of calculating MMF, and the approaches of obtaining leakage coefficients and HTS heat loss by using 3-D simulation), the design results of a 1 MW HTS-TLG, the induced voltage characteristics of the HTS-TLG and the grid connection of output power, the cryogenic vessels and input power of cryocooler. The results obtained in the study of this chapter allow significant conclusions to be drawn as:

- HTS field leakage coefficient affects the geometric dimension of armature part, and the HTS operating current determined by HTS heat loss affects the field poles. With these two pivotal parameters obtained by 3-D simulation, adequate design results can

be obtained.

- Design results of the 1 MW HTS-TLG show some merits like high air gap flux density of 1.35 T, little amount of HTS wires used (only 0.4 tons), and a very light translator (about 9.5 tons). The light translator benefits for the reduction of mechanical tension to the heaving buoy of the WEC.
- Due to the changing velocity of the heaving buoy, electrical frequency of the HTS-TLG varies in amplitude, with peak values much higher than wave frequency. As a result, the induced phase voltage varies in both amplitude and frequency during one-cycle operation.
- Heat loads of cryogenic vessels mainly come from the GFRP pins and the SI, and the total heat loss is evaluated as 400 W, requiring 8 kW input power to a cryocooler.

Finally, in order to investigate the possible advantages of HTS-TLGs to large-scale WEC application, optimal design results of three types of TLGs are presented and compared. The comparison results on main machine parameters and generator costs suggests that the HTS-TLG has distinguished advantages in generator weight, translator weight, generator size, and total cost. Moreover, to study the influence of wave characteristics on design results of HTS-TLGs, two HTS-TLGs designed with different wave data are compared from the aspects of main machine performance and cost. And the comparison results indicate that HTS-TLGs designed with different wave data exhibit very different generator performance.

Main contributions of this thesis are to the clarified operating state of the heaving buoy, the developed electrical design method of HTS electric machines, the obtained design results of a 1 MW HTS-TLG, the proposed novel topology of connecting output power of WEC systems to grid, and the suggested configuration of cryogenic vessels. These contributions are highlighted as follows:

- By studying the relation of buoy size and the maximum output power, it shows a simple method of determining geometric parameters of the heaving buoy.
- The developed electrical design method of HTS-TLGs would be a good guidance to design HTS electric machines, which provides an efficient way of determining main machine parameters. The methods of obtaining leakage coefficients and evaluating HTS heat loss with 3-D simulation are presented, which lead to optimal design of the HTS-TLGs.
- Design results of the 1 MW HTS-TLG provide a candidate to WECs for practical application.
- Novelty of the topology of connecting WEC output power to grid lie in the reduction of expensive filters.
- The suggested structure of cryogenic vessels and the arrangement of HTS coils provide a reference to industrial manufacture.

6.2 Future research

The studies presented in this thesis demonstrated the feasibility of employing large-scale HTS-TLGs to WEC application, which establish the foundation for future experimental works. The future researches considered are outlined below.

(1) Grand design of a laboratory-scale WEC prototype with a HTS-TLG

A laboratory-scale WEC prototype will be designed, including a cylindrical heaving buoy, a HTS-TLG with capacity of several hundred watts, and a cooling system.

(2) Manufacture of the HTS-TLG

This process involves many key engineering technologies of manufacture and assembly of HTS-TLGs, such as the winding of HTS coils, the manufacture of HTS cryostat, and the installation of adiabatic tubes. Fulfillment of this process will provide a good guidance to manufacture HTS electric machines.

(3) Experimental studies on electromechanical characteristics of the HTS-TLG

After the HTS-TLG is fabricated, it is planned to erect the HTS-TLG and drive the translator with a slider-crank mechanism [108], which convert the rotating motion of a prime mover into reciprocating linear motion. In this way, the induced voltages of the HTS-TLG at different excitation currents will be tested and analyzed. In addition, mechanical properties of the bearings will be also tested.

(4) On-site test of the WEC system

All the buoy, the HTS-TLG, a DC power supply, a full-bridge rectifier, and a transmission cable will be assembled together. And the WEC system will be tested at sea to make its output voltage characteristics and mechanical properties clear.

References

1 https://www.iea.org/media/statistics/Keyelectricitytrends2015.pdf

2 I. López, J. Andreu, S. Ceballos, I. Alegría, I. Kortabarria, “Review of wave energy technologies and the necessary power-equipment,” Renewable and Sustainable Energy Reviews, vol. 27, pp. 413-434, Nov. 2013.

3 J. Cruz, Ed., “Introduction,” in Ocean wave energy: current status and future prepectives. Berlin: Springer, 2008.

4 Alain Cle´ment, Pat McCullen, Anto´nio Falca˜o, et. al., “Wave energy in Europe: current status and perspectives,” Renewable and Sustainable Energy Reviews, 6, pp. 405–431, 2002.

5 B. Drew, A. R. Plummer, and M. N. Sahinkaya, “A review of wave energy converter technology,” *Proc. IMechE Vol. 223 Part A: J. Power and Energy*, Jun. 2009.

6 Kester Gunn, Clym Stock-Williams. "Quantifying the global wave power resource". Renewable Energy, Volume 44, August 2012, Pages 296–304.

7 S. H. Salter, “Wave power,” Nature, 249, pp. 720-724, Jun. 1974.

8 T. W. Thorpe, “An overview of wave energy technologies, status, performance and costs,” *Wave Power: Moving to Commercial Viability*, London, U.K., 1999.

9 http://www.emec.org.uk/marine-energy/wave-devices/

10 António F. de O. Falcão, “Wave energy utilization: A review of the technologies,” Renewable and Sustainable Energy Reviews, vol. 14, Issue 3, pp. 899-918, Apr. 2010.

11 http://www.awsocean.com

12 Heath T, Whittaker TJT, Boake CB, “The design, construction and operation of the LIMPET wave energy converter (Islay Scotland),” 4th EWEC, Aalborg, Denmark, 2000.

13 http://www.oceanlinx.com

14 http://www.oceanpowertechnologies.com/

15 http://www.emec.org.uk/about-us/wave-clients/pelamis-wave-power/

16 "Update on EMEC activities, resource description, and characterisation of wave-induced velocities in a tidal flow" (PDF). Online available.

17 http://www.power-technology.com/projects/pelamis/

18 J. P. Kofoed, P. Frigaard, E. Friis-Madsen, H. C. Sorensen, “Prototype testing of the wave energy converter Wave Dragon,” Renewable Energy, vol. 31(2), pp.181-189, 2006.

19 http://www.wavedragon.net/

20 Vicinanza D, Margheritini L, Kofoed JP, Buccino M, “The SSG wave energy converter: performance status, and recent developments,” Energies, vol. 5 (2), pp. 193-226, 2012.

21 http://www.emec.org.uk/about-us/wave-clients/aquamarine-power/

22 Queen's University of Belfast, “Islay LIMPET wave power plant,” Technical report, the Queen's University of Belfast, 2002.

23 R. Curran, and L. M. C. Gato, “The energy conversion performance of several types of wells turbine designs,” *Proc. IMechE, Part A: J. Power and Energy*, vol. 211 (A2), pp. 133–145, 1997.

24 M. Torresi, S. M. Camporeale, P. D. Strippoli, and G. Pascazio, “Accurate numerical simulation of a high solidity wells turbine,” *Renew. Energy*, 33(4), pp. 735-747, 2008.

25 T. Finnigan, D. Auld, “Model testing of a variable-pitch aerodynamic turbine,” In: International offshore and polar engineering conference, pp. 357-360, 2003.

26 A. Gareev, “Analysis of variable pitch air turbines for oscillating water column (owc) wave energy converters,” Technical Report, University of Wollongong, School of Mechanical, Material and Mechatronic Engineering, 2011.

27 M. Takao, E. Sato, S. Nagata, K. Toyota, and T. Setoguchi, “A sea trial of wave power plant with impulse turbine,” in Proceedings of the 27th International Conference on Offshore Mechanics and Arctic Engineering (OMAE ’08), Paper no. OMAE2008-57535, pp. 681–688, Estoril, Portugal, June 2008.

28 M. Takao, and T. Setoguchi, “Air turbines for wave energy conversion,” International Journal of Rotating Machinery, vol. 2012, Article ID 717398, pp. (1023-621X):2382–2396, 2012.

29 M.S. Lagoun, A. Benalia, and M. E. H. Benbouzid, “Ocean wave converters: state of the art and current status,” *2010 IEEE International Energy Conference*, pp. 636-641, 2010.

30 M. Suzuki, M. Takao, E. Sato, S. Nagata, K. Toyota, and T. Setoguchi, “Performance prediction of OWC type small size wave power device with impulse turbine,” Journal of Fluid Science and Technology, vol. 3, no. 3, pp. 466–475, 2008.

31 O. Paish, “Small hydro power: technology and current status,” vol. 6, pp. 537–556, 2002.

32 H. Polinder, M. E. C. Damen, and F. Gardner, “Linear PM generator system for wave energy conversion in the AWS,” IEEE Trans. Energy Convers., vol. 19, no. 3, pp. 583-589, Sept. 2004.

33 H. Polinder, M. E. C. Damen, and F. Gardner, “Design, modelling and test results of the AWS PM linear generator,” Eur. Trans. Elect. Power, vol. 15, no. 3, pp. 245–256, May/Jun. 2005.

34 S. H. Salter, “Wave power,” Nature, vol. 249, pp. 720-724, 1974.

35 Alain Cle´ment, Pat McCullen, Anto´nio Falca˜o, et. al., “Wave energy in Europe: current status and perspectives,” *Renewable and Sustainable Energy Reviews*, 6, pp. 405–431, 2002.

36 P. C. J. Clifton, R. A. McMahon, and H. P. Kelly, “Design and commissioning of a 30 kW direct drive wave generator,” in Proc. IET 5th Int Conf. Power Electron., Mach. Drives, Brighton, U.K., 2010, pp. 1–6.

37 M. Leijon, O. Danielsson, M. Eriksson, et al., “An electrical approach to wave energy conversion,” Renew. Energy, vol. 31, no. 9, pp. 1309-1319, Jul. 2006.

38 J. Prudell, M. Stoddard, E. Amon, T. K. A. Brekken, and A. von Jouanne, “A permanent-magnet tubular linear generator for ocean wave energy conversion,” IEEE Trans. Ind. Appl., vol. 46, no.

6, pp. 2392–2400, Nov. 2010.

39 N. J. Baker, and M.A. Mueller, “Direct drive wave energy converters,” Rev. Energ. Ren.: Power Engineering, pp. 1-7, 2001.

40 H. Polinder，B. C. Mecrow，A. G. Jack，P. Dickinson，M. A. Mueller, “Linear generators for direct-drive wave energy conversion,” IEEE International Electric Machines & Drives Conference, 2003, 2(2):798-804 vol.2

41 N. Hodgins, O. Keysan, A. McDonald, and M. Mueller, “Linear generator for direct drive wave energy applications,” in Proc. Int. Conf. Elect. Mach., Rome, Italy, 2010, pp. 1–6.

42 Neil Hodgins, Ozan Keysan, Alasdair S. McDonald, and Markus A. Mueller, “Design and Testing of a Linear Generator for Wave-Energy Applications”, IEEE Trans. Ind. Electron., vol. 59, no. 5, May 2012.

43 H. Polinder, M.A. Mueller, M. Scuotto and M. Goden de Sousa Prado, “Linear generator systems for wave energy conversion,” *Proceedings of the 7th European Wave and Tidal Energy Conference*, Porto, Portugal, 2007.

44 I. Ivanova, O. Ågren, H. Bernhoff, and M. Leijon, “Simulation of a 100 kW permanent magnet octagonal linear generator for ocean wave conversion,” *Sci. Tech. Rev.*, Mar. 2004 [in Russian].

45 M. Leijon, O. Danielsson, M. Eriksson, et al., “An electrical approach to wave energy conversion,” *Renewable Energy*, 31, pp. 1309–1319, 2006.

46 H. Weh, H. Hoffmann, and J Landrath, “New permanent magnet excited synchronous machine with high efficiency at low speed,” *Proc. Int. Conf. Electrical Machines*, Pisa, Italy, pp. 35-40, Sept. 1988.

47 P. R. M. Brooking, and M. A. Mueller, “Power conditioning of the output from a linear vernier hybrid permanent magnet generator for use in direct drive wave energy converters,” *IEE Proc.-Gener. Transm. Distrib.*, vol. 152, no. 5, Sept. 2005.

48 M. A. Mueller, and N. J. Baker: “Modelling the performance of the vernier hybrid machine,” *IEE Proc. Electr. Power Appl.*, 150 (6), pp. 647-653, 2003.

49 Y. Du, K. T. Chau, M. Cheng, et al., “Design and Analysis of Linear Stator Permanent Magnet Vernier Machines,” *IEEE Trans. Magn.*, vol. 47, issue. 3, pp. 4219-4222, Oct. 2011.

50 J. H. Prudell. “Novel design and implementation of a permanent magnet linear tubular generator for wave energy conversion,” Master thesis. Corvallis, OR: Oregon State University, 2007.

51 I. Stamenkovic, N. Milivojevic, N. Schofield, and M. Krishnamurthy, “Design, analysis, and optimization of ironless stator permanent magnet machines,” *IEEE Trans. Power Electron.*, vol. 28, no. 5, pp. 2527-2538, May 2013.

52 L. Huang, H. Yu, M. Hu, J. Zhao, and Z. Cheng, “A novel flux-switching permanent-magnet linear generator for wave energy extraction application,” IEEE Trans. Magn., vol. 47, no. 5, pp. 1034-1037, May 2011.

53 J. F. Pan, Y. Zou, N. Cheung, and G. Z. Cao, “On the voltage ripple reduction control of the linear switched reluctance generator for wave energy utilization,” IEEE Trans. Power Electron., vol. 29, no. 10, pp. 5298-5307, Oct. 2014.

54 P. R. M. Brooking and M. A. Mueller, “Power conditioning of the output from a linear vernier hybrid permanent magnet generator for use in direct drive wave energy converters,” in Proc. Inst. Elect. Eng.—Gener., Transm. Distrib., vol. 152, no. 5, pp. 673-681, Sept. 2005.

55 J. Bardeen, L. N. Cooper, and J. R. Schrieffer, “Theory of superconductivity,” Physical Review, vol. 108, no. 5, pp. 1175-1204, Dec. 1957.

56 C. P. Bean, "Magnetization of high-field superconductors," *Rev. Mod. Phys.*, vol.36, pp. 31-38, 1964.

57 M. Tinkham, “Introduction to superconductivity,” 2nd ed. Dover Publications, 1996.

58 M. P. Oomen, “AC loss in superconducting tapes and cables,” Ph.D. dissertation, University of Twente, Enschede, The Netherlands, 2000.

59 M. Ainslie, “Transport AC loss in high temperature superconducting coils,” University of Cambridge, Ph.D. dissertation, 2012.

60 M. P. Oomen, “AC loss in superconducting tapes and cables,” Energy for Sustainable Development, 2000.

61 Iwasa, “Case studies in superconducting magnets design and operational issues,” Second edition,

62 D. Larbalestier, A. Gurevich, D. M. Feldmann, and A. Polyanskii, “High-T_c superconducting materials for electric power applications,” *Nature*, vol. 414, no.15, Nov. 2001.

63 http://global-sei.com/

64 http://www.amsc.com/

65 http://www.superpower-inc.com/

66 S. Greg, G. Bruce, and K. Swarn, “The performance of a 5 MW high temperature superconductor ship propulsion motor,” *Trans. Appl. Supercond.*, vol. 15, no. 2, pp. 2206-2209, 2005.

67 G. Bruce, S. Greg and M. Tim, “Full power test of a 36.5 MW HTS propulsion motor,” *IEEE Trans. Appl. Supercond.*, vol. 21, no. 3, pp. 1083-1088, Jun. 2011.

68 G. Nerowski, J. Frauenhofer, G. Ries, W. Nick, and H. W. Neumüller, “Advances and prospects of HTS rotating machine development at siemens”. Power Engineering Society General Meeting, vol. 2, pp. 2052-2055, 2004.

69 “SeaTitan™ 10 MW Wind Turbine,” [Available online]: http://www.amsc.com/documents/seatitan-10-mw-wind-turbine-data-sheet/

70 Y. Xu, N. Maki, and M. Izumi, “Electrical design study of 10-MW salient-pole wind turbine HTS synchronous generators,” *IEEE Trans. Appl. Supercond.*, vol. 24, no. 6, Dec. 2014.

71 A. B. Abrahamsen, B. B. Jensen, E. Seiler, et al., “Feasibility study of 5 MW superconducting wind turbine generator,” *Physica C,* 471, pp. 1464-1469, 2011.

72 W. H. Fietz, M. J. Wolf, A. Preuss, R. Heller, K. P. Weiss, “High-current HTS cables: Status and actual development,” *IEEE Trans. Appl. Supercond.*, vol. 26 (4), 2016.

73 B. Zhang, R. Shi, Z. Chi, et al., “Review and outlook of HTS cable research,” Applied Mechanics & Materials, vol. 734 pp. 720-725, 2014.

74 J. Bock, M. Bludau, R. Dommerque, et al., “HTS fault current limiters—first commercial devices for distribution level grids in Europe,” IEEE Trans. Appl. Supercond., vol. 21 (3), 2011.

75 A. Morandi, “State of the art of superconducting fault current limiters and their application to the electric power system,” *Physica C*, vol. 484, pp. 242-247, Jan. 2013.

76 M. Staines, M. Pannu, N. Glasson, and N. Allpress, “Superconducting transformers – Part I,” *TRANSFORMERS MAGAZINE*, vol. 3, Issue 2, pp. 68-73, 2016.

77 S. Dai, T. Ma, Q. Qiu, Z. Zhu, Y. Teng, L. Hu, “Development of a 1250-kVA superconducting transformer and its demonstration at the superconducting substation,” *IEEE Trans. Appl. Supercond.*, vol. 26 (1), 2015.

78 S. Mukoyama, T. Matsuoka1, M. Furukawa, et al., “Development of REBCO HTS magnet of magnetic bearing for large capacity flywheel energy storage system,” *Physics Procedia*, 65, pp. 253- 256, 2015.

79 Y. Miyazaki, K. Mizuno, T. Yamashita, et al., “Development of superconducting magnetic bearing for flywheel energy storage system,” Cryogenics, 80, pp. 234-237, 2016.

80 J. Zhu, M. Qiu, B. Wei, H. Zhang, X. Lai, and W. Yuan, “Design, dynamic simulation and construction of a hybrid HTS SMES (high-temperature superconducting magnetic energy storage systems) for Chinese power grid,” *Energy*, 51, pp. 184-192, 2013.

81 L. Bertola, T. Cox, P. Wheeler, S. Garvey, and H. Morvan, “Superconducting electromagnetic launch system for civil aircraft,” *IEEE Trans. Appl. Supercond.*, vol. 26 (8), Dec. 2016.

82 Gorazd Stumberger, Mehmet Timur Aydemir, Damir Žarko, and Thomas A. Lipo, “Design of a linear bulk superconductor magnet synchronous motor for electromagnetic aircraft launch systems,” *IEEE Trans. Appl. Supercond.*, vol. 14, no. 1, March 2004.

83 F. Yen et al., “A single-sided linear synchronous motor with a high temperature superconducting coil as the excitation system,” *Superconductor Science and Technology*, vol. 23, no. 10, p. 105015, Oct. 2010.

84 S. J. Zheng, F. Yen, J. Li, et al., “Performance of a small-scale high temperature superconducting linear synchronous motor prototype,” *IEEE Trans. Appl. Supercond.*, vol. 22, no. 2, pp. 5200104, Apr. 2012.

85 J. X. Jin, L. H. Zheng, Y. G. Guo, and J. G. Zhu, “Performance characteristics of an HTS linear synchronous motor with HTS bulk magnet secondary,” *IEEE Trans. Ind. Appl.*, vol. 47, no. 6, pp. 2469-2477, Nov. 2011.

86 Y. Du, K. T. Chau, M. Cheng, Y. Wang, and J. Li, “A linear doubly-salient HTS machine for wave energy conversion,” *IEEE Trans. Appl. Supercond.*, vol. 21, no. 3, Jun. 2011.

87 O. Keysan and M. Mueller, “A linear superconducting generator for wave energy converters,” *in IET International Conf. on PEMD*, pp. 134, 2012.

88 O. Farrok, Md. R. Islam, Md. R. I. Sheikh, Y.G. Guo, J. G. Zhu, and W. Xu, “A novel superconducting magnet excited linear generator for wave energy conversion system,” *IEEE Trans. Appl. Supercond.*, vol. 26, no. 7, Oct. 2016.

89 L. Huang, M. Hu, J. Liu, H. Yu, C. Zeng, and Z. Chen, “Electromagnetic design of a 10-kW-class flux-switching linear superconducting hybrid excitation generator for wave energy conversion,” *IEEE Trans. Appl. Supercond.*, vol. 27, no. 4, June 2017.

90 L. Huang, J. Liu, H. Yu, R. Qu, H. Chen, and H. Fang, “Winding configuration and performance investigations of a tubular superconducting flux-switching linear generator,” *IEEE Trans. Appl. Supercond.*, vol. 25, no. 3, Jun. 2015.

91 J. Falnes and M. Perlin, “Ocean waves and oscillating systems, linear interaction including wave-energy extraction,” *Applied Mechanics Reviews*, 56(1):286, 2003.

92 J. Falnes, “Ocean waves and oscillating systems : linear interactions including wave-energy extraction,” Cambridge University Press , 2002

93 S. Barstow, “WorldWaves: Integrated model, satellite and in-situ measurements providing quality wave and wind data anywhere, anytime,” Fugro OCEANOR, Norway, Apr. 2010.

94 “Ocean energy in Ireland,” An ocean strategy for Ireland submitted to the Department of Communications, Marine and Natural Resources, Oct. 2005. Online available: http://www.seai.ie/Renewables/Renewable_Energy_Policy/Policy_Initiatives/19_Ocean_Energy_Strategy_Report.pdf

95 http://www.oceanor.no/Services/Worldwaves/WW_database

96 I. A. Ivanova, H. Bernhoff, O. Ågren, and M. Leijon, “Simulated generator for wave energy extraction in deep water,” Ocean Engineering, 32, pp. 1664–1678, 2005.

97 http://cdip.ucsd.edu/themes/m/latest?r=2

98 F. Wu, X. P. Zhang, P. Ju, and M. J. H. Sterling, “Optimal control for AWS-based wave energy conversion system,” *IEEE Trans. Power Syst.*, vol. 24, no. 4, pp. 1747–1755, 2009.

99 H. Polinder, B. C. Mecrow, A. G. Jack, P. G. Dickinson, and M. A. Mueller, “Conventional and TFPM linear generators for direct-drive wave energy conversion,” *IEEE Trans. Energy Convers.*, vol. 20, no. 2, pp. 260–267, 2005.

100 M. Cheng, K. T. Chau, and C. C. Chan, “Design and analysis of a new doubly salient permanent magnet motor,” *IEEE Trans. Magn.*, vol. 37, no. 4, pp. 3012–3020, 2001.

101 S. S. Kalsi, K. Weeber, H. Takesue, C. Lewis, H.-W. Neumueller, and R. D. Blaugher, “Development status of rotating machines employing superconducting field windings,” *Proc. IEEE*, vol. 92, no. 10, pp. 1688–1704, 2004.

102 R. Pei, A. Velichko, M. Majoros, Y. Jiang, R. Viznichenko, Z. Hong, R. Marchant, A. M. Campbell, and T. A. Coombs, “Ic and AC loss of 2G YBCO tape measurement for designing

and fabrication of an HTS motor," *IEEE Trans. Appl. Supercond.*, vol. 18, no. 2, pp. 1236–1239, 2008.

103 Y. Koshiba *et al*., "Critical current and electric loss under magnetic field at 30 K on Bi-2223 superconducting coil for ship propulsion motor," *IEEE Trans. Appl. Supercond.*, vol. 21, no. 3, pp. 1127-1130, Jun. 2011.

104 S. Fujita, M. Daibo, T. Takeuchi, *et al*., "Evaluation of rare-earth-based coated conductors-mechanical, delamination and in-field critical current properties," *TEION KOGAKU (J. Cryo. Super. Soc. Jpn.)*, vol. 48, no. 4, 2013.

105 K. Thorburn, H. Bernhoff, and M. Leijon, "Wave energy transmission system concepts for linear generator arrays," *Ocean Engineering*, 31, pp. 1339-1349, 2004.

106 H. Hirai, M. Hirokawa, S. Yoshida, T. Sano, and S. Ozaki, "Development of a turbine-compressor for 10 kW class neon turbo-Brayton refrigerator," American Institute of Physics, 2014:1236-1241.

107 http://www.cryomech.com/

108 http://eng-aos.com/upload/upfile/ar/113.pdf

Acknowledgement

Firstly, I would like to express my deepest appreciation to my supervisor Prof. Mitsuru Izumi for the continuous encouragement and support of my Ph.D. study, for his instructive advice and valuable suggestions on this thesis. He deserves more respect and my appreciation for his dedication to academic research and his kindness. His immense knowledge and enthusiasm at work have always been great motivation and tremendous encouragement to me.

Besides my supervisor, I would like to express my heartfelt gratitude to Prof. Naoki Maki. I greatly appreciate his continuous contributions of time and ideas to my research. He has broad knowledge and vast experience in designing electric machines. His guidance helped me in most of the time of Ph.D. pursuit and writing of this thesis.

My sincere thanks also go to everybody in my laboratory. Thank Prof. T. Ida and Dr. M. Miki for the support and time to time discussions on my research. Dr. Y. Xu, Dr. Z. Li, Dr. K. Yamaguchi, Dr. S. Erasmus, Mr. C. Bouquel, Mr. H. Tsubouchi, Mr. R. Matsumi, Mr. K. Nishimura and others, you all helped me a lot in adapting to Japanese life, learning Japanese language, and doing the Ph.D. research. Thank you all for your kind support, which made my life in Japan easier.

I would also like to thank my Chinese friends, who sent video calls or messages to comfort me in some depressed moments.

Last but not least, special thanks to my family, who have been helping me out of difficulties and supporting without a word of complaint.

List of publications

[1] **Hailian Jing**, Naoki Maki, Tetsuya Ida, Mitsuru Izumi. “Design study of large-scale HTS linear generators for wave energy conversion”, *IEEE Trans. Appl. Supercond.*, vol. 27, no. 4, Jun. 2017, Art no. 5202105. (SCI: EU3EB, WOS:000400910300001)

[2] **Hailian Jing,** Naoki Maki, Tetsuya Ida, Mitsuru Izumi. “Performance comparison of MW class tubular linear generators for wave energy conversion”, *IEEE Trans. Appl. Supercond.*, vol. 27, no. 6, pp. 1-6, Sept. 2017, Art no. 5203906. (SCI: FA9PF, WOS: 000405777300001)

[3] **Hailian Jing,** Naoki Maki, Tetsuya Ida, Mitsuru Izumi. “Study on key design technologies of a wave energy converter with a HTS linear generator”, *IEEE Trans. Appl. Supercond*., vol. 27, no. 7, Oct. 2017, Art no. 5204108. (DOI: 10.1109/TASC.2017.2732224)

[4] **Hailian Jing**, Naoki Maki, Tetsuya Ida, Mitsuru Izumi. “Electrical design of large-scale tubular PM linear generators for wave energy conversion”, *IEEJ Transactions on Electrical and Electronic Engineering*, vol.12, no. S2, Dec. 2017, in press. (DOI: 10.1002/tee.22555)